DESIGN OF SUBSTRATE INTEGRATED WAVEGUIDE BASED BANDPASS FILTERS AND POWER DIVIDERS

A THESIS
SUBMITTED TO THE DEPARTMENT OF ELECTRICAL AND ELECTRONICS ENGINEERING
AND THE GRADUATE SCHOOL OF ENGINEERING AND SCIENCE
OF BILKENT UNIVERSITY
IN PARTIAL FULFILLMENT OF THE REQUIREMENTS
FOR THE DEGREE OF
MASTER OF SCIENCE

By
Sinan Kurudere
July, 2013

I certify that I have read this thesis and that in my opinion it is fully adequate, in scope and in quality, as a thesis for the degree of Master of Science.

Assoc. Prof. Vakur B. Ertürk (Advisor)

I certify that I have read this thesis and that in my opinion it is fully adequate, in scope and in quality, as a thesis for the degree of Master of Science.

Prof. Ayhan Altıntaş

I certify that I have read this thesis and that in my opinion it is fully adequate, in scope and in quality, as a thesis for the degree of Master of Science.

Prof. Özlem Aydın Çivi

Approved for the Graduate School of Engineering and Science:

Prof. Dr. Levent Onural
Director of the Graduate School

ABSTRACT

DESIGN OF SUBSTRATE INTEGRATED WAVEGUIDE BASED BANDPASS FILTERS AND POWER DIVIDERS

Sinan Kurudere
M.S. in Electrical and Electronics Engineering
Supervisor: Assoc. Prof. Vakur B. Ertürk
July, 2013

A microwave system is, in general, designed by using fundamental components such as filters, couplers, dividers, etc. Due to the fact that wavelength becomes comparable with lumped element dimensions, at microwave frequencies distributed elements are used for building these components. Microstrip based devices can be used up to certain frequencies. However, when radiation loss increases, waveguide based devices are used which are bulky and costly.

Recently, substrate integrated waveguide (SIW) based devices have attracted the attention of many researchers due to low cost, lightweight and efficient high frequency characteristics. SIW is the printed circuit realization of a waveguide. SIW is fabricated on a dielectric material with top and bottom sides are conductors, and two linear arrays of metallic vias form the side walls. In this thesis, by using SIW structure, iris type bandpass filters are designed, analyzed and fabricated for verification. After that, complementary split ring resonator (CSRR) and dumbbell type defected ground structure (DGS) etched filters that are available in the literature are investigated and verified with simulations. Having investigated different filter topologies in the literature, a novel SIW based bandpass filter is proposed, where its second harmonic is suppressed using a dumbbell type DGS underneath the microstrip feed line. The filter is demonstrated with a fabricated prototype, where the simulated and measured results agree well. Furthermore, SIW based power dividers available in the literature and the corrugated SIW (CSIW) architecture which uses open-circuit ended quarter-wavelength stubs instead of vias as the sidewalls, are investigated. CSIW architecture is implemented to a power divider structure available in the literature and a novel CSIW based high isolation power divider is designed and demonstrated with a fabricated prototype. Good agreement between simulated and fabricated results are observed.

Keywords: Substrate Integrated Waveguide (SIW), Bandpass Filter, Power Divider.

ÖZET

MALZEMEYE GÖMÜLÜ DALGA KILAVUZU TABANLI BANT GEÇİREN SÜZGEÇ VE GÜÇ BÖLÜCÜ TASARIMI

Sinan Kurudere
Elektrik ve Elektronik Mühendisliği, Yüksek Lisans
Tez Yöneticisi: Assoc. Prof. Vakur B. Ertürk
Temmuz, 2013

Mikrodalga sistem, genellikle, süzgeç, bağlaştırıcı, güç bölücü gibi temel elemanlarla tasarlanır. Mikrodalga frekanslarda dalgaboyu toplu eleman büyüklüğüyle kıyaslanabilir olduğu için dağınık elemanlar kullanılır. Belirli frekanslara kadar mikroşerit yapılar kullanılabilir, fakat yayılma kaybı arttıkça hantal ve pahalı olan dalga kılavuzları kullanılır.

Son yıllarda, malzemeye gömülü dalga kılavuzu (MGDK) tabanlı yapılar, az maliyetli, hafif ve verimli yüksek frekans karakteristikleriyle birçok araştırmacının dikkatini çekmiştir. MGDK, dalga kılavuzunun baskı devre gerçeklemesidir. MGDK, malzemenin alt ve üst yüzeyindeki iletkenler ve iki dizi halinde metalik deliklerle tasarlanır. Bu tezde MGDK yapılarını kullanarak, iris tipinde bant geçiren süzgeçler tasarlanmıştır, analiz edilmiş ve doğrulamak için üretilmiştir. Daha sonra, literatürdeki tümler yarıklı halka rezonatör (TYHR) ve dambıl tipinde deforme toprak yapısı (DTY) gömülü süzgeçler incelenip benzetimle doğrulanmıştır. Literatürdeki farklı süzgeç yapıları incelendikten sonra, yeni MGDK tabanlı, ikinci harmoniğin mikroşerit hat altındaki dambıl tipi DTY ile bastırıldığı bant geçiren süzgeç önerilmiştir. Süzgeç üretilmiş ve üretim sonuçları benzetim sonuçlarıyla örtüşmüştür.

Son olarak, literatürdeki MGDK tabanlı güç bölücüler ve metalik deliklerin açık-devre uçlu çeyrek-dalgaboyu çubuklarla yapıldığı oluklu MGDK (OMGDK) yapıları incelenmiştir. OMGDK yapısı literatürdeki güç bölücülere uygulanarak yüksek izolasyonlu yeni bir güç bölücü tasarlanmış ve üretilmiştir. Üretim sonuçları benzetim sonuçlarıyla örtüşmüştür.

Anahtar sözcükler: Malzemeye Gömülü Dalga Kılavuzu (MGDK), Bant Geçiren

Süzgeç, Güç Bölücü.

Acknowledgement

I would like to mention my endless thanks to my supervisor Assoc. Prof. Vakur B. Ertürk for his guidance and encouragement during the development of this thesis.

I would like to thank to members of my jury, Prof. Ayhan Altıntaş and Prof. Özlem Aydın Çivi for reading and commenting on my thesis.

I would like to express my thanks to my company Meteksan Defence Ind. Inc. for encouraging me to pursue this degree and to use their facilities for both fabrication and measurement. Especially, many thanks to my manager İrfan Yıldız for sharing his knowledge with me, Ali Rıza Acer for his excellent PCB manufacturing skills and my friends Volkan Aban, S. Meliksah Yayan and S. Can Aksoy for their help during the measurements.

I would like to thank to Turkish Scientific and Technological Research Council (TÜBİTAK) for their financial support during my graduate study.

Finally, I would like to thank to my family for their patience and endless love.

Contents

1 Introduction **2**

2 Substrate Integrated Waveguide **9**

2.1 SIW Design Equations 9

2.2 Transitions to Other Guiding Structures 14

2.2.1 Microstrip to SIW Transition 15

2.2.2 Grounded Coplanar Waveguide to SIW Transition 17

2.2.3 Waveguide to SIW Transition 18

2.3 SIW and Microstrip Comparison 20

3 SIW Bandpass Filters **23**

3.1 Iris Type SIW Bandpass Filters 24

3.1.1 Theory and Design Equations 24

3.1.2 SIW Iris Filter Design at X and K-Bands 28

3.2 SIW Bandpass Filter with CSRR and DGS 30

3.2.1 SIW Bandpass Filter with CSRR Structures 31

3.2.2 SIW Bandpass Filter with CSRR and Dumbbell Structures 34

3.3 Novel SIW Based Interdigital Filter with Harmonic Suppression . 36

4 SIW Power Dividers 52

4.1 T-junction SIW Power Divider 53

4.2 Y-junction SIW Power Divider 55

4.3 Corrugated SIW 57

4.4 Novel CSIW Based Power Divider 59

5 Conclusion 66

A Frequency Bands 77

B Datasheets 79

List of Figures

1.1 Microstrip line 3

1.2 Rectangular waveguide 4

1.3 Substrate integrated waveguide (SIW) 4

2.1 Substrate integrated waveguide (SIW) 10

2.2 Dimensions of the air filled waveguide 10

2.3 Dimensions for SIW 11

2.4 Geometry of SIW for testing 12

2.5 S_{11} results for d=20 mil and p=20, 30, 40 and 50 mil for the geometry illustrated in Fig. 2.4 13

2.6 S_{21} results for d=20 mil and p=20, 30, 40 and 50 mil for the geometry illustrated in Fig. 2.4 13

2.7 Simulated S_{21} results for TE_{10} and TE_{20} modes 15

2.8 Microstrip to SIW tapered transition 16

2.9 Simulation results of the microstrip to SIW tapered transition . . 16

2.10 Grounded coplanar waveguide (GCPW) 17

2.11 GCPW to SIW transition 18

2.12 Simulation results of the GCPW to SIW tapered transition 18

2.13 Waveguide to SIW transition 19

2.14 Simulation results of the waveguide to SIW transition 20

2.15 SIW (top) and microstrip line (below) structures 21

2.16 Southwest Microwave 2.92 mm end-launch connectors 21

2.17 S_{21} (insertion loss) measurement results 22

2.18 S_{11} (return loss) measurement results 22

3.1 Air filled waveguide 7^{th} order iris filter model 26

3.2 Iris type waveguide bandpass filter. The upper one is with the electrical and the below one is with the physical parameters. . . . 27

3.3 SIW iris filter at X-band 29

3.4 SIW iris filter at K-band 29

3.5 CST MWS model for the SIW iris filter at X-band 31

3.6 CST MWS model for the SIW iris filter at K-band 31

3.7 Measured and simulated S_{11} and S_{21} for the X-band filter 32

3.8 Measured and simulated S_{11} and S_{21} for the K-band filter 32

3.9 Bandpass SIW filter that uses CSRRs. Top figure is the upper side and the bottom figure is the ground side of the filter 33

3.10 CSRR structure 34

3.11 Simulated S_{11} and S_{21} results of the 3^{rd} order SIW filter that uses CSRRs . . . 35

3.12 Bottom view of the SIW filter with CSRR and dumbbell. 36

3.13 Simulated S_{11} and S_{21} results of the SIW filter with CSRR and dumbbell . . . 37

3.14 Single resonator in the SIW . . . 38

3.15 Simulated S_{11} and S_{21} results of a single resonator in the SIW . . 39

3.16 Simulated S_{21} versus frequency for varying cap radius . . . 40

3.17 Top (up) and bottom (below) surfaces of the three resonators in the filter . . . 41

3.18 Simulated S_{11} and S_{21} results of the 3^{rd} order filter depicted in Fig. 3.17 with the parameters tabulated in Table 3.6 . . . 42

3.19 Top (up) and bottom (below) surfaces of the modified filter 43

3.20 Simulated S_{11} and S_{21} results of the modified 3^{rd} order filter depicted in Fig. 3.19 with the parameters tabulated in Table 3.7 . . 44

3.21 Top (up) and bottom (below) views of the final SIW interdigital filter . . . 45

3.22 Measured and simulated S_{11} and S_{21} results of the 3^{rd} order SIW interdigital filter depicted in Fig. 3.21 for the final parameters tabulated in Table 3.8 . . . 46

3.23 A 3^{rd} order SIW iris filter at 9 GHz . . . 46

3.24 Simulated S_{11} and S_{21} results of both the SIW interdigital filter and the SIW iris filter with the parameters tabulated in Table 3.8 and 3.9, respectively. . . . 47

3.25 Measured and simulated S_{11} and S_{21} results of the proposed SIW interdigital filter depicted in Fig. 3.21 for the final parameters tabulated in Table 3.8 47

3.26 1^{st} order dumbbell DGS 48

3.27 Simulated S_{11} and S_{21} results of the 1^{st} order dumbbell DGS . . . 48

3.28 3^{rd} order dumbbell DGS 49

3.29 Simulated S_{11} and S_{21} results of the 3^{rd} order dumbbell DGS . . . 49

3.30 Bottom surface of the 3^{rd} order SIW interdigital filter with the dumbbell type DGS 50

3.31 Manufactured filter images. The longer filter is with the dumbbell type DGS whereas the shorter filter does not have the dumbbell type DGS. 50

3.32 Simulated and measured S_{11} and S_{21} results of the filter with the dumbbell DGS 51

4.1 T-junction SIW power divider 53

4.2 Simulation results of the T-junction SIW power divider illustrated in Fig. 4.1 with the parameters tabulated in Table 4.1 54

4.3 Y-junction SIW power divider 56

4.4 Simulation results of the Y-junction SIW power divider illustrated in Fig. 4.3 whose parameters are tabulated in Table 4.2 56

4.5 CST view of CSIW with microstrip transition 58

4.6 S-parameter simulation results of microstrip to CSIW transition at X-band for the design shown in Fig. 4.5 with the parameters tabulated in Table 4.3 58

4.7 CST model of the CSIW power divider 60

4.8 Fabricated CSIW power divider 61

4.9 S_{11} versus frequency results of the divider shown in Fig. 4.8 with the parameters tabulated in Table 4.4 62

4.10 S_{21} and S_{31} versus frequency results of the divider shown in Fig. 4.8 with the parameters tabulated in Table 4.4 62

4.11 Isolation of the divider (resistors are present) shown in Fig. 4.8 with the parameters tabulated in Table 4.4 63

4.12 Isolation of the divider with and without the resistors (divider is shown in Fig. 4.8 with the parameters tabulated in Table 4.4) . . 63

4.13 Effects of the resistors on S_{11} and S_{21} for the divider shown in Fig. 4.8 with the parameters tabulated in Table 4.4 64

4.14 Effects of the resistor on the output return losses for the divider shown in Fig. 4.8 with the parameters tabulated in Table 4.4 . . . 64

4.15 Phases of S_{21} and S_{31} for the divider shown in Fig. 4.8 with the parameters tabulated in Table 4.4 65

List of Tables

3.1 Dimensions of the X-band SIW iris filter 30

3.2 Dimensions of the K-band SIW iris filter 30

3.3 Dimensions of the SIW bandpass filter with CSRR 34

3.4 Dimensions of the SIW bandpass filter with CSRR and dumbbell 36

3.5 Effect of cap radius to the upper cut-off frequency 38

3.6 Dimensions of the 3^{rd} order SIW interdigital filter in Fig. 3.17 . . 39

3.7 Dimensions of the 3^{rd} order modified filter seen in Fig. 3.19 41

3.8 Dimensions of the final SIW interdigital filter 42

3.9 Dimensions of the 3^{rd} order SIW iris filter 43

3.10 Dimensions of the dumbbell type resonators 45

4.1 Dimensions of the T-junction SIW power divider 54

4.2 Dimensions of the Y-junction SIW power divider 55

4.3 Dimensions of the CSIW at X-band 57

4.4 Dimensions of the CSIW divider at X-band 61

A.1 Frequency bands with corresponding waveguide standards 78

To My Family ...

Chapter 1

Introduction

The lumped circuit element approximations of standard circuit theory are not valid at microwave frequencies (ranging from 300 MHz to 300 GHz) due to the fact that device dimensions become comparable (or even larger) with the wavelength. Therefore, microwave components are usually treated as distributed elements, where the phase of a voltage or current changes significantly over the physical length of the device. Consequently, voltages and currents are treated as waves which propagate over the device, and propagation effects can no longer be ignored [1].

A microwave circuit (or a system) is, in general, an interconnection of many fundamental microwave devices such as filters, couplers, power divider/combiners, etc. However, an essential requirement in all these devices is the ability to transfer signal power from one point to another as efficient as possible (i.e., with minimum amount of loss). This requires the transport of electromagnetic energy in the form of a propagating wave. Therefore, all the aforementioned fundamental microwave devices are designed and manufactured in the form of a guiding structure so that electromagnetic waves can be guided from one point to another without much loss [2].

Microstrip lines are among the most widely used guiding structures at relatively lower microwave frequencies because of their simple construction, low cost

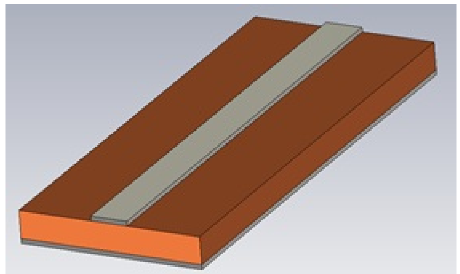

Figure 1.1: Microstrip line

and high integrability with surface mount components. A typical microstrip line is formed using a conductor on one side of a dielectric layer substrate with a single ground plane forming the other side and air above, as shown in Fig. 1.1. The top conductor is basically a conducting material (generally preferred copper) shaped in the form of a narrow line. The width of this line, the thickness, the relative dielectric constant and the dielectric loss tangent of the substrate are important parameters. Moreover, the thickness (i.e., the metallization thickness) and the conductivity of the conductors can also be critical at higher frequencies. By carefully considering these parameters and using microstrip lines as building blocks, many printed microwave devices and components such as filters, couplers, power divider/combiners, mixers, etc. can be designed. However, as the frequency increases (when moved to relatively higher microwave frequencies), transmission loss increases and radiation emerges [1]. Therefore, hollow-pipe waveguides such as a rectangular waveguide, shown in Fig. 1.2, are preferred because of less loss at higher frequencies (no radiation). Inside of a waveguide is usually air. However, if desired, it can be filled with a dielectric material resulting a smaller cross-section compared to the air-filled waveguide. Unfortunately, hollow-pipe waveguides are usually bulky, can be heavy especially at lower frequencies, their productions can be difficult and costly, and they are not integrable with printed structures.

Recently, a hybrid guiding architecture between microstrip structures and waveguides called substrate integrated waveguide (SIW) has been proposed [3]. SIWs are integrated waveguide like structures fabricated on a dielectric material with top and bottom sides are conductors, and two linear arrays of metallic vias form the side walls as shown in Fig. 1.3. When compared to microstrip and

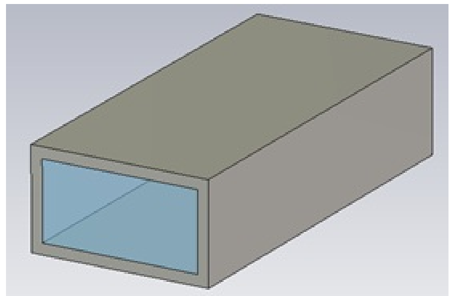

Figure 1.2: Rectangular waveguide

waveguide structures, a SIW has the characteristics of both, namely, cost effective, relatively easy fabrication process, integrable with planar devices. Besides, it is claimed to perform better than microstrip structures at high frequencies and has the waveguide dispersion characteristics [3]. Consequently, a significant number of SIW based microwave components such as filters, couplers, power divider/combiners has been reported so that they can replace their microstrip and/or waveguide counterparts at appropriate frequencies [3]-[65]. A comprehensive review of SIW circuits including the theoretical background with the design equations is provided in [3] and [4].

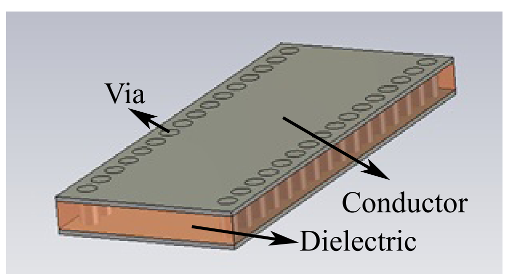

Figure 1.3: Substrate integrated waveguide (SIW)

As mentioned before, a microwave circuit (or a system) is usually an interconnection of many basic microwave components such as filters, couplers, power divider/combiners, amplifiers, attenuators, etc. Among them, filters play a vital role in the design of radio frequency (RF) and microwave systems. A microwave filter is a two-port network. It is used to control the frequency response at a certain point in a microwave system by allowing transmission at frequencies within the passband of the filter, and rejecting (by significantly attenuating) the signal flow within the stopband of the filter [1]. Based on their frequency responses, filters can be grouped as follows.

Low-pass Filters: Allow transmission of signals with no or little attenuation at frequencies lower than a predetermined critical frequency, called cut-off frequency, and reject the signals at frequencies higher than the cut-off frequency.

High-pass Filters: Allow transmission of signals with no or little attenuation at frequencies higher than the cut-off frequency and reject the signals at frequencies lower than the cut-off frequency.

Band-pass Filters: Allow transmission of signals with frequencies within a band bounded by a lower and an upper cut-off frequencies and reject signals out of this band.

Band-reject (Band-stop) Filters: Reject signals within a frequency band bounded by a lower and an upper cut-off frequencies and allow transmission at frequencies out of this band.

One of the main focus in this thesis is to design SIW filters. In the literature, majority of the SIW filter designs are about bandpass SIW filters. Therefore, several bandpass SIW filter topologies available in the literature have been investigated. Iris waveguide bandpass filters are realized using SIW technology in [21]-[29]. The initial states of the design of these filters are performed in a similar fashion to that of air-filled waveguide iris filters. However, after determining the necessary parameters for the air-filled waveguide iris filters, a scale factor is found by using the air-filled waveguide and SIW dimensions, and this scale factor is used to determine all the critical parameters when the filter is realized with the SIW technology. In Chapter 3 of this thesis, more details about this process are given. Another group of SIW bandpass filters are based on SIW cavities and the couplings between these cavities [30]-[36]. In the design of these filters, the first step is to design the necessary SIW cavities and to decide the coupling scheme. Then, the corresponding generalized coupling matrix is determined by using a computer-aided-design (CAD) tool such as HFSS or CST Microwave Studio (MWS). As a result, the initial design is obtained. Finally, via optimization and tuning, the final design is realized. Recently, a significant number of SIW bandpass filters is realized by loading the SIW architecture by complementary split ring resonators (CSRRs) [66], where usually square CSRRs are etched on the waveguide surface [37]-[47]. As a result, these structures allow the implementation of a forward-wave passband propagating below the characteristic cut-off frequency of the waveguide. It has been observed that when properly designed these filters exhibit high selectivity and compact size due to the employment of subwavelength resonators and an evanescent wave transmission [38]. In a similar fashion, SIW bandpass filters are also realized by implementing a defected ground structure (DGS) into the development of a SIW filter [48]-[51]. These filters are realized by etching different shapes such as dumbbell, ring or even periodic geometries to the ground conductor of the waveguide surface. It should be noted that using combination of these topologies multiband bandpass filters are also realized in [19] and [31].

On the other hand, one main focus of this thesis is to design novel SIW bandpass filters. Thus, several bandpass SIW filter topologies available in the literature have been investigated. Among them, first iris type SIW bandpass filters at X and K-bands (center frequencies 10 GHz and 21 GHz, respectively) have been designed, analyzed and fabricated. Measurement and simulation results agree well with each other. Then, several CSRR loaded SIW bandpass filters have been investigated in the form of simulations around 9 GHz. During the simulations, several small modifications to those exist in the literature have been performed to improve the filter response as well as to ease the fabrication process. Finally, a novel SIW bandpass filter with interdigital type resonators has been proposed. A 3^{rd} order prototype has been designed to operate at 9 GHz with an approximately 500 MHz bandwidth. Dumbbell type DGS has been used at the ground part of the structure right below the microstrip based feeding to suppress the next harmonic expected around 13.5 GHz. Good agreement between the simulation and measurement results has been observed. Moreover, the proposed filter exhibits good filtering properties with an excellent harmonic suppression at 13.5 GHz.

Another important microwave component that has been widely used in microwave systems is a power divider/combiner used to divide or combine power equally or unequally (with respect to a predetermined ration). Three port T-junction and Y-junction power dividers are the most widely used power dividers (or combiners). Therefore, SIW based power divider/combiners have gained prominence in recent years due to their compact size, light weight and high isolation compared to waveguide power dividers. As a result, different types of SIW power divider/combiners have been presented before [54]-[65]. Recently, the corrugated substrate integrated waveguide (CSIW) architecture has been presented in [52] and [53], where open-circuit quarter-wavelength microstrip stubs are used in place of vias to form the side walls of the SIW. In [52], it is stated that CSIW is compatible with SIW but permits ease of integration of active devices. Moreover, open-circuit quarter-wavelength microstrip stubs are easier to fabricate than vias. Considering these advantages of CSIW, in this thesis, we have proposed a novel CSIW based power divider (which is a CSIW realization of a SIW based power divider) at X-band. Measurement and simulation results agree well with each other and the manufactured CSIW based power divider exhibits a high isolation.

The outline of this thesis is as follows:

In Chapter 2, the basic SIW concept is presented together with the SIW design equations. Then, its transition to other guiding structures are given. Finally, a comparison between SIW and microstrip structures is presented in terms of loss and matching.

Chapter 3 is related with the bandpass SIW filters. Investigation of different SIW bandpass filters such as iris type SIW bandpass filters at X and K-bands and CSRR loaded SIW filters at X-band, are discussed and compared with dumbbell type DGS loaded filters. Finally, a novel SIW bandpass filter with interdigital type resonators are presented.

Chapter 4 focuses on SIW power dividers and the CSIW architecture. The CSIW idea is combined with the power divider concept, and a novel CSIW based power divider is presented in this chapter.

Finally, Appendix A which contains the most widely used microwave frequency bands with corresponding standard waveguide dimensions and Appendix B which contains all the related datasheets are added to the end of this thesis.

Chapter 2

Substrate Integrated Waveguide

Substrate integrated waveguides (SIWs) are integrated waveguide like structures fabricated by using two rows of metal vias embedded in a dielectric that connect two parallel metal plates. The rows of metal vias form the side walls. This relatively new architecture has the properties of both microstrip line and waveguide. Its manufacturing process is also similar to other printed planar architectures. A typical SIW geometry is illustrated in Fig. 2.1, where its width (i.e., the separation between the vias in the transverse direction (a_s)), the diameter of the vias (d) and the pitch length (p) are the most important geometrical parameters (as shown in Fig. 2.1) that are used for designing SIW structures as will be explained in the next section. It should be noted that the dominant mode is TE_{10} just like a rectangular waveguide.

2.1 SIW Design Equations

The relationship between the cut-off frequency, f_c, and the dimensions a and b of an air-filled waveguide (AFWG) and a dielectric filled waveguide (DFWG) are the starting points of a SIW design. For an AFWG (refer to Fig. 2.2), the cut-off

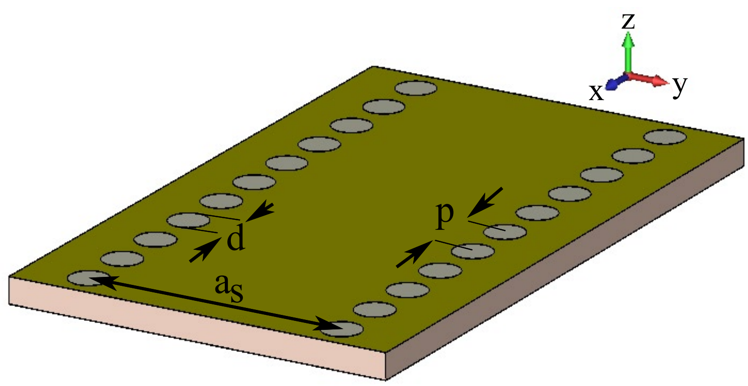

Figure 2.1: Substrate integrated waveguide (SIW)

frequency of a mode is given by

$$f_c = \frac{c}{2\pi}\sqrt{(\frac{m\pi}{a})^2 + (\frac{n\pi}{b})^2} \tag{2.1}$$

where c is the speed of light in free space, m and n are mode numbers, a is the longer and b is the shorter dimensions of the waveguide. Because it is desired to work at the dominant TE_{10} mode, (2.1) is simplified to

$$f_c = \frac{c}{2a} \tag{2.2}$$

for an AFWG.

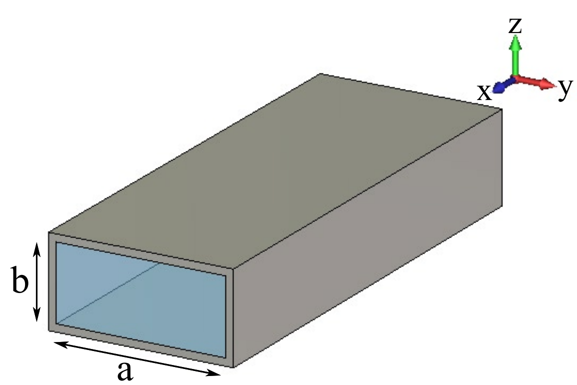

Figure 2.2: Dimensions of the air filled waveguide

The same f_c (i.e., for the dominant TE_{10} mode) for a DFWG can be obtained when a is replaced by $a_d = a/\sqrt{\epsilon_r}$, where ϵ_r is the relative dielectric constant of the dielectric that fills the waveguide. Making use of these information and aiming to work at the same f_c (i.e., the dominant TE_{10} mode of SIW) the first empirical design equation of a SIW is related to its width, a_s, and is given by [5]

$$a_s = a_d + \frac{d^2}{0.95p} \tag{2.3}$$

where a_d is the width of the DFWG corresponding to the same f_c, d is the diameter of the vias, and p is the center to center separation between the vias along the longitudinal direction as shown in Fig. 2.3. A general rule of thumb for the choice of d and p is given in (2.4) and (2.5), respectively [5].

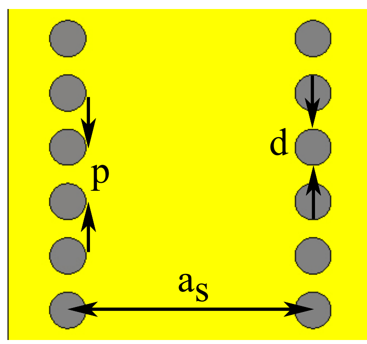

Figure 2.3: Dimensions for SIW

$$d < \lambda_g/5 \tag{2.4}$$

$$p < 2d \tag{2.5}$$

where λ_g is the guided wavelength [17] and is given by

$$\lambda_g = \frac{2\pi}{\sqrt{(\frac{\epsilon_r(2\pi f)^2}{c^2}) - (\frac{\pi}{a})^2}}. \tag{2.6}$$

Note that the thickness of the substrate does not affect these design equations, but it affects the loss of the structure in such a way that the low loss advantage of a high thickness substrate should be considered.

One way to interpret equations (2.4) and (2.5) is that for a fixed via diameter, d, the pitch length, p, affects the performance of a SIW. Therefore, to investigate the reflection and transmission properties of a SIW structure for varying p values, the S-parameters (i.e., S_{11} and S_{21}) of the geometry shown in Fig. 2.4 are simulated using CST Microwave Studio. The input and output ports of the SIW geometry are modeled with rectangular vias with CST MWS to excite it as a DFW. Hence, possible meshing related errors of the simulator due to circular vias at the ports are minimized. Rogers 3003 with a thickness of 10 mil, $\epsilon_r = 3$ and loss tangent 0.0013 is selected as the substrate as it is widely used in industry. Its conductors are copper with a thickness of 0.7 mil.

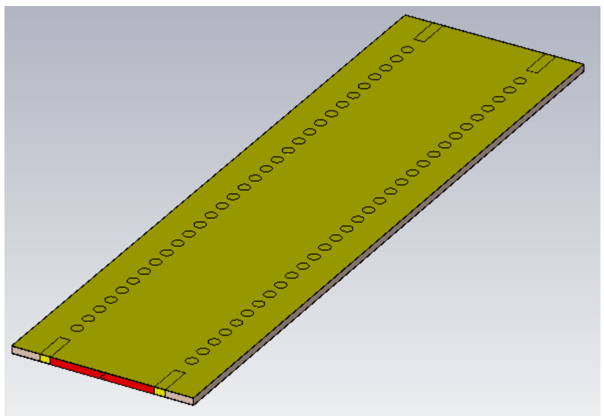

Figure 2.4: Geometry of SIW for testing

Ka band (26.5-40 GHz) is considered as the frequency band, and the SIW structure is designed for 40 GHz. At this frequency $\lambda_g = 179$ mil and hence, the maximum d becomes 35.8 mil as given by (2.4). Thus, d is fixed to 20 mil since it is one of the standard via diameter. Then, the pitch length p, is varied. However, for each p, the width of the SIW, a_s, is recalculated from (2.3) to ensure that SIW is properly designed. Finally, the length of the SIW is selected to be 1000 mil for all cases. Simulations are performed with CST MWS (as mentioned before). Fig. 2.5 illustrates S_{11} versus frequency of the designed SIW along the Ka-band for varying p values (p = 20, 30, 40 and 50 mil). Minimum p is determined by the fabrication tolerances. Similarly, Fig. 2.6 illustrates the S_{21} versus frequency for the same design and same variations. Note that according to (2.5) the maximum value of p must be 40 mil. However, larger values (p = 50 mil) are selected to see its effect on the performance of the design. It can be observed from the S-parameter results that as the length of p increases, return loss (S_{11}) increases (from -30 dB to -17 dB being the maximum value of the return loss in the whole

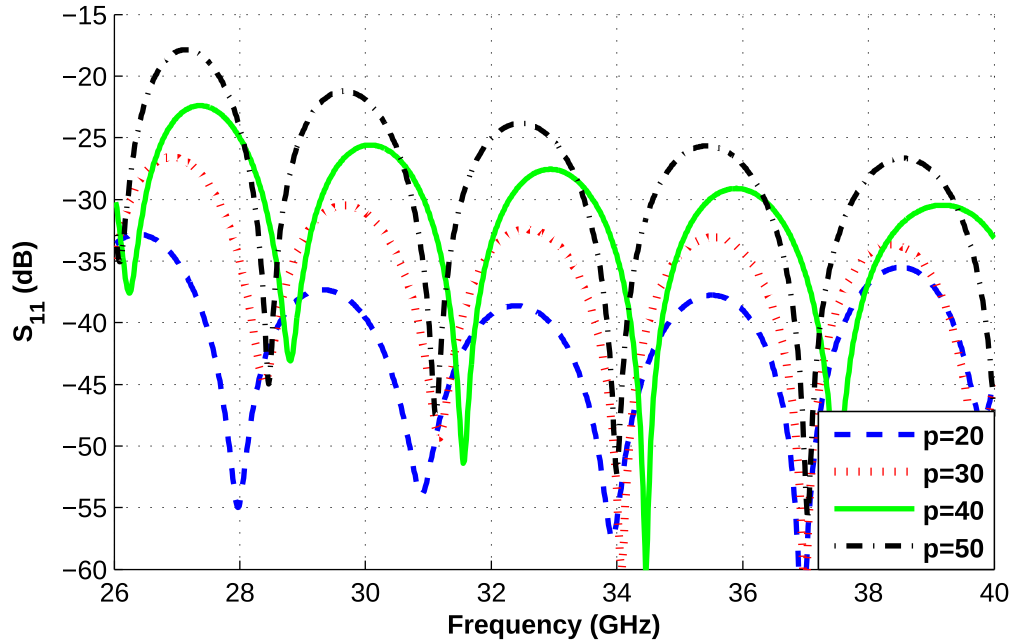

Figure 2.5: S_{11} results for d=20 mil and p=20, 30, 40 and 50 mil for the geometry illustrated in Fig. 2.4

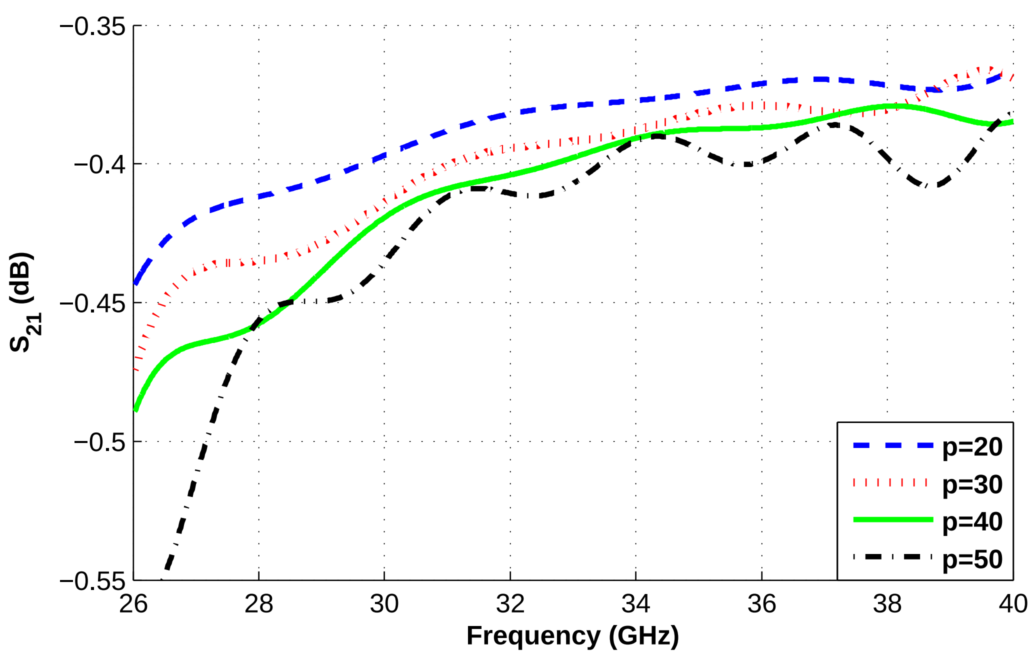

Figure 2.6: S_{21} results for d=20 mil and p=20, 30, 40 and 50 mil for the geometry illustrated in Fig. 2.4

frequency band) as well as the insertion loss increases and ripples emerge (see Fig. 2.6) due to an increase in RF leakage between the vias.

When the results presented in Fig. 2.5 and Fig. 2.6 are investigated, it is clear that the design equations given by (2.3)-(2.5) work well. However, a better strategy to design a SIW is to use them as initial design equations and after the initial design; they can be optimized. Flexibility of determining the cut-off frequency is an advantage of SIW compared to standard waveguides.

Finally, the operating frequency of SIW is investigated at X-band. Similar architecture shown in Fig. 2.4 is used. The substrate used in this design is Rogers TMM10i with 25 mil thickness, $\epsilon_r = 9.8$ and loss tangent 0.002. The critical SIW dimensions/parameters for the design are as follows: $a_s = 297$ mil, $d = 16$ mil and $p = 28$ mil. When all modes are included in the simulations, the next higher mode after the dominant TE_{10} mode is TE_{20} which is similar to that of an AFWG. As illustrated in Fig. 2.7, the cut-off frequency of X-band of the SIW is about 6.7 GHz for the TE_{10} mode, and the next cut-off frequency occurs at approximately two times of this cut-off at 13.4 GHz. Therefore, as in AFWG case, TE_{20} mode is the next higher mode of SIW. As a result, operating frequency ranges of standard AFWG (which are given in Appendix A), can also be used for SIW structures.

2.2 Transitions to Other Guiding Structures

SIW can be integrated both with printed and waveguide structures, and for all transitions broad and narrow band matching can be achieved. Microstrip, grounded coplanar waveguide and rectangular waveguide to SIW transitions are the most widely used transitions and hence, they are described in this section.

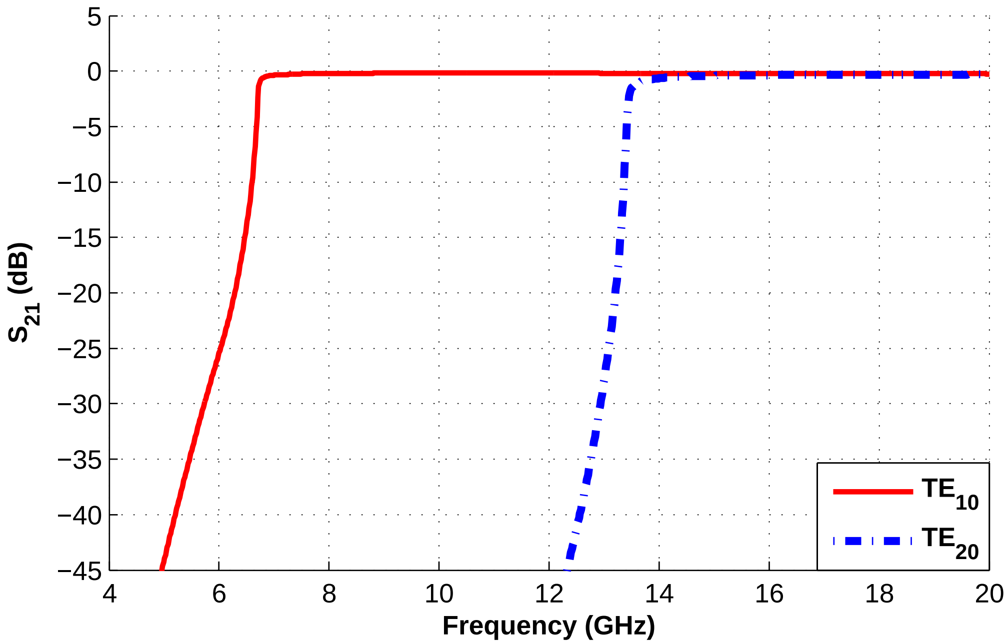

Figure 2.7: Simulated S_{21} results for TE_{10} and TE_{20} modes

2.2.1 Microstrip to SIW Transition

When microstrip structures are desired to be connected to SIW, tapered microstrip transition, seen in Fig. 2.8, is one of the largely preferred transitions and it usually provides broadband matching compared to other printed transitions [11]. However, taper length can be relatively long due to the long wavelength at low frequencies. Therefore, other transition topologies can be considered for low frequency applications.

We designed a microstrip to SIW transition on Rogers 5880, with thickness 10 mil, $\epsilon_r = 2.2$ and loss tangent $= 0.0009$ at Ka band since both the substrate and the frequency band are widely used in microwave applications. The designed SIW has a center-to-center width (a_s) of 198 mil. The via diameter (d) is selected to be 16 mil and the pitch length (p) is 28 mil. These dimensions are consistent with the SIW design equations given by (2.3)-(2.5). The taper width (w_t) and the taper length (l_t), depicted in Fig. 2.8, are 65 mil and 200 mil, respectively, and are found via optimization so that matching at the Ka band can be achieved.

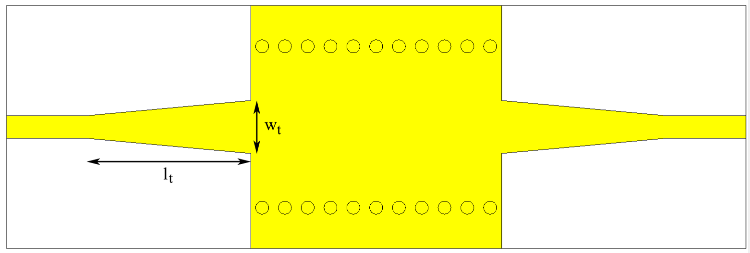

Figure 2.8: Microstrip to SIW tapered transition

Simulation results for this transition are illustrated in Fig. 2.9. As seen from the results, a broadband matching, (i.e., S_{11} is below -15 dB in the whole frequency band) is provided, and since reflection is very low, insertion loss is mostly caused by dielectric and conductor losses. The choice of the substrate and the conductor materials mainly determine the loss of the transition.

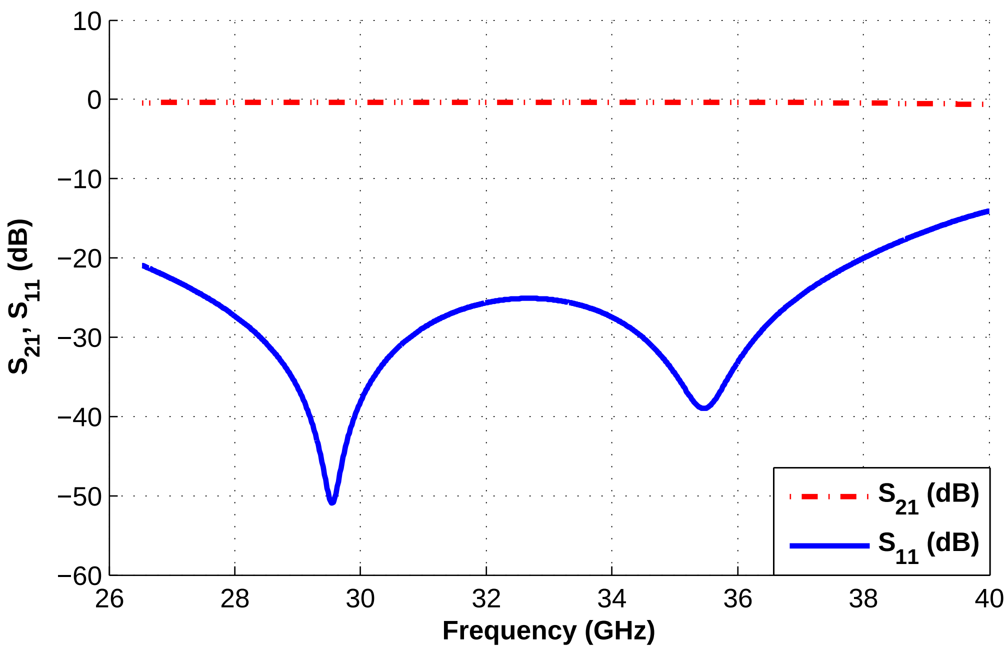

Figure 2.9: Simulation results of the microstrip to SIW tapered transition

Finally, it should be noted that because the thickness of the substrate determines the width of the microstrip line for a predefined characteristic impedance, taper parameters should be modified when the thickness of the substrate is changed.

2.2.2 Grounded Coplanar Waveguide to SIW Transition

Grounded coplanar waveguide (GCPW) shown in Fig. 2.10 is another widely preferred transmission line structure in high frequency systems. As in the microstrip case, bottom side of the substrate is ground. However, side conductors near the main line are also used as ground. By adjusting the width of the main line and the gap between the main line and the side ground, desired characteristic impedance can be obtained. Due to the flexibility of the main line width, GCPW is preferred in microwave applications.

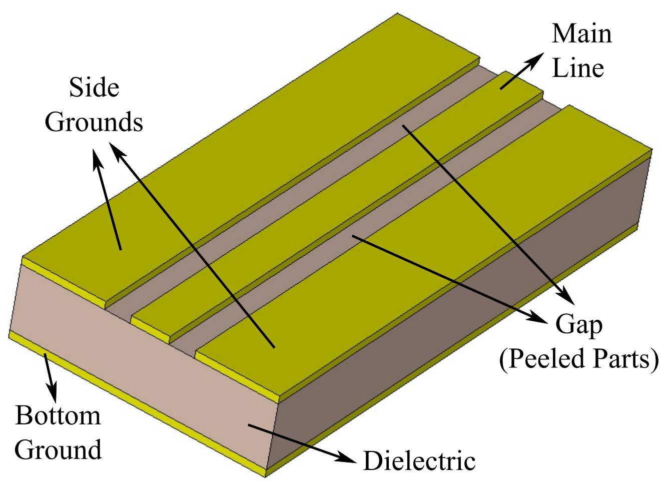

Figure 2.10: Grounded coplanar waveguide (GCPW)

A GCPW to SIW transition, illustrated in Fig. 2.11, is designed and simulated for the Ka-band in this sub-section. Rogers TMM10i substrate with a thickness of 25 mil, $\epsilon_r = 9.8$ and loss tangent $= 0.002$ is used as the substrate. Using the design equations given in (2.3)-(2.5), the SIW parameters are as follows: $d = 16$ mil, $p = 28$ mil and $a_s = 99$ mil. The transition, as in the microstrip case, is made with a taper whose length (l_t) and width (w_t) are optimized for the best matching at the desired frequency band [13]. In this design, $w_t = 65$ mil and $l_t = 50$ mil. The taper is inserted into the SIW section, and the gap (10 mil) between the main line and side ground is kept the same in the transition part as well. The width of the main line is 15 mil. As seen from the results shown in Fig. 2.12 a broadband matching (i.e., S_{11} is below -15 dB in the whole frequency band) is provided. Besides, the insertion loss is very small.

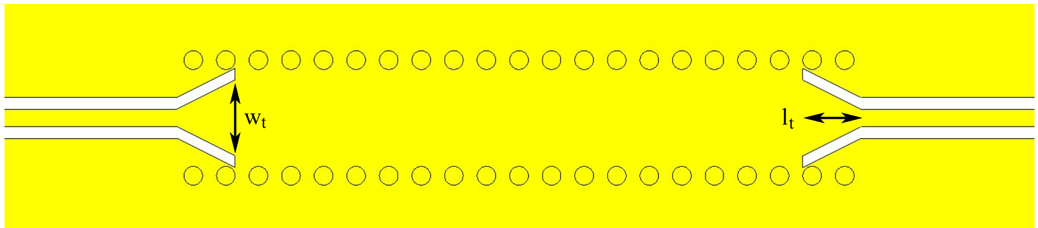

Figure 2.11: GCPW to SIW transition

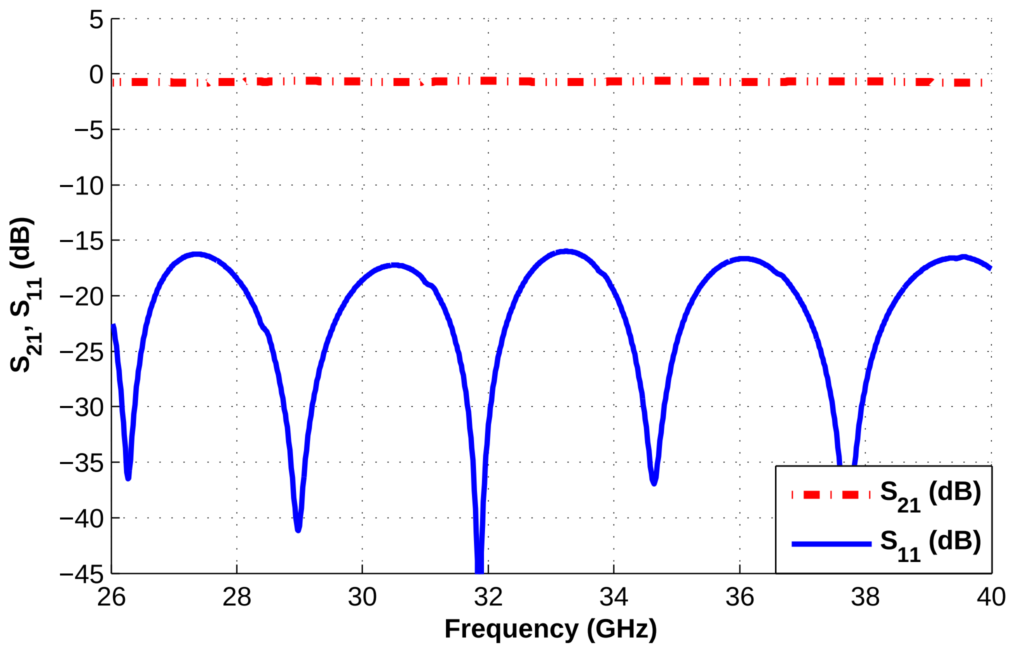

Figure 2.12: Simulation results of the GCPW to SIW tapered transition

2.2.3 Waveguide to SIW Transition

Another widely used transition in microwave systems is the rectangular waveguide (RWG) to SIW transition. To achieve this transition, one method is to introduce a slot on the top of the SIW as described in [14]. A rectangular slot whose dimensions to be optimized is introduced at the top of the SIW, and a rectangular SIW cavity section around it is optimized with vias for the best matching, which is illustrated in Fig. 2.13. Slot is placed at the center of the rectangular SIW cavity. Slot is the blue colored part on the SIW, and its dimensions are smaller than the standard waveguide dimensions. Finally, the red colored parts are the

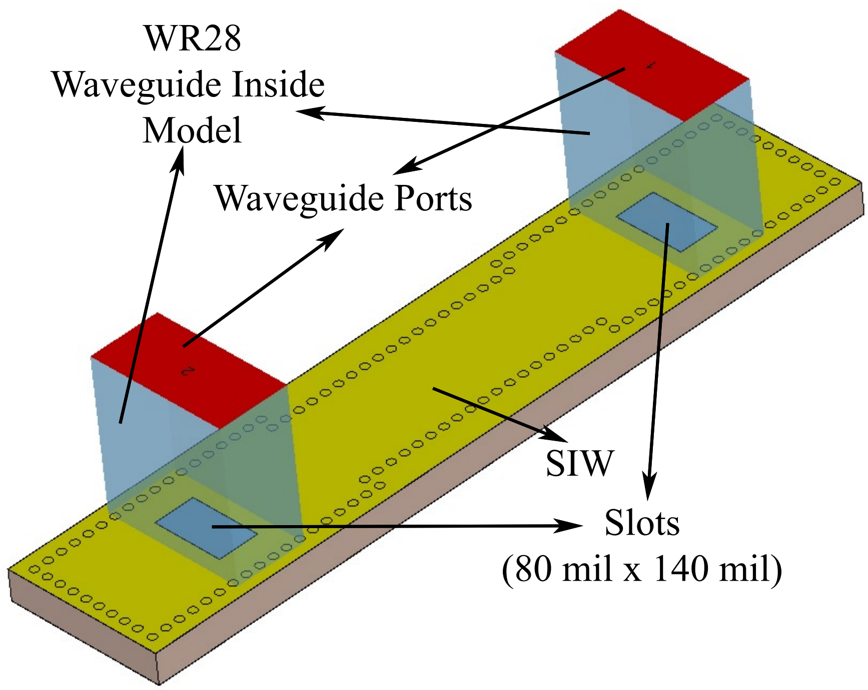

Figure 2.13: Waveguide to SIW transition

waveguide ports. RWG is shown on the top of the slot with light blue color.

A simple RWG to SIW transition is designed on Rogers 5880 that has a thickness of 62 mil, $\epsilon_r = 2.2$ and loss tangent = 0.0009. WR-28 waveguide (280 mil x 140 mil) is used since the desired frequency band is the Ka band. The design parameters for the SIW part is as follows: $d = 16$ mil, $p = 28$ mil and $a_s =$ 200 mil. Rectangular slot, introduced at the top of the SIW, has 80 mil x 140 mil dimensions, and the SIW cavity around it has a dimension of 280 mil x 481 mil. The results for the transmission and reflection, seen in Fig. 2.14, are optimized for 32 GHz. Compared to the GCPW and microstrip transitions described in the previous sub-sections, a relatively narrower bandwidth is obtained from this transition. However, the insertion loss is still small (i.e. less than 0.5 dB around the center frequency).

Different waveguide to SIW transitions exist and they can be found in [15] and [16].

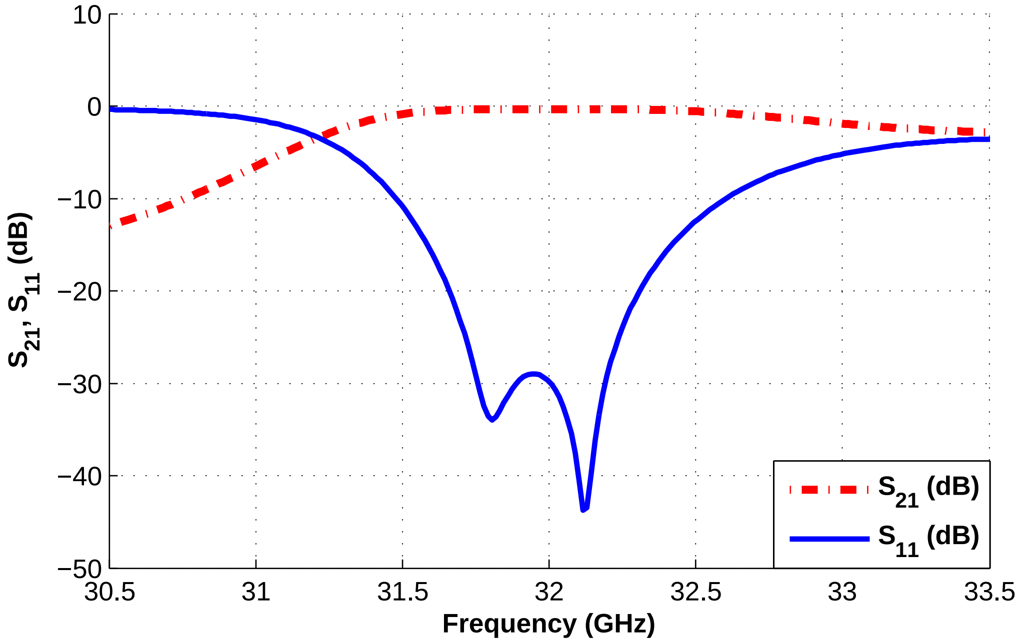

Figure 2.14: Simulation results of the waveguide to SIW transition

2.3 SIW and Microstrip Comparison

As the last part of this chapter, the performances of a microstrip line and a SIW structure are compared in terms of loss and matching. Rogers RO4003 is used as the substrate for the measurement. Its relative dielectric constant is listed as 3.38, it has a loss tangent of 0.0027 and its thickness is 20 mil. This substrate can be processed easily, via hole plating process on it is easy and cost effective. A 50 Ω microstrip line is designed whose width is 44 mil and has a total length of 3448 mil (considering the diameter of the vias and the pitch length). Similarly, a SIW with a microstrip transition is designed with a_s = 150 mil and the total length 3448 mil, same with that of the microstrip line. Both structures are designed relatively long (i.e., 3448 mil) so that possible losses in the microstrip transition part remain negligible compared to the losses in the main structures. The measurements are performed at the Ka-band. Manufactured SIW and microstrip line structures are shown in Fig. 2.15. Southwest Microwave's 2.92 mm end-launch connectors, seen in Fig. 2.16 are used. These connectors have low loss, better than -12 dB return loss at the Ka-band, and they squeeze the substrate thereby eliminating the need for extra soldering. Overall their performance is well at Ka-band.

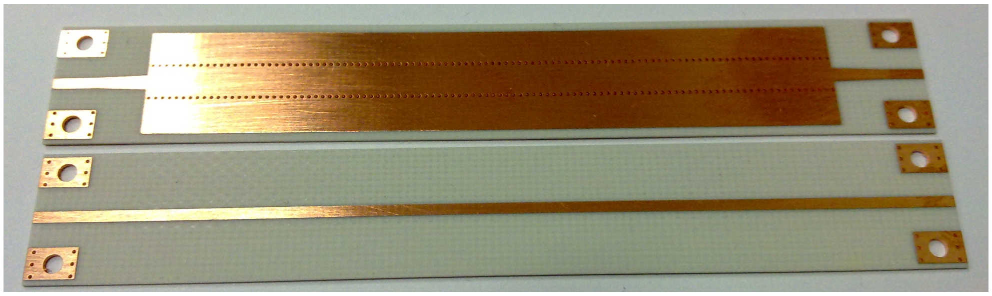

Figure 2.15: SIW (top) and microstrip line (below) structures

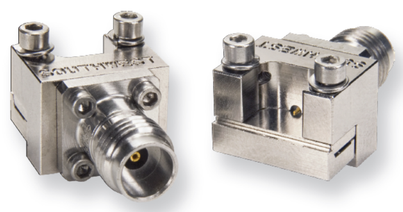

Figure 2.16: Southwest Microwave 2.92 mm end-launch connectors

Fig. 2.17 shows the measured insertion loss (i.e., S_{21} (dB)) comparison of SIW and microstrip line structures versus frequency for the 30 - 40 GHz band (since a good SIW to microstrip line matching could not be achieved with the fabricated prototype in the whole Ka-band). Possible connector losses, fabrication tolerances and measurement errors cause ripples in the insertion loss. However, the most important point for this measurement is that SIW appears to be lossier than the microstrip line through the whole Ka-band. This is a bit surprising because the radiation loss of microstrip line was expected to dominate the loss mechanism. Probably, the losses in the microstrip line transition to SIW as well as the leakage of waves from the side walls (between the vias) are the dominant contributions to loss for the SIW structure.

Similarly, Fig. 2.18 shows the measured S_{11} (in dB) comparison for both structures versus frequency for the same 30 - 40 GHz band. Return loss performance of both structures are compatible and S_{11} is better than -12 dB for both cases which is sufficient for many practical applications.

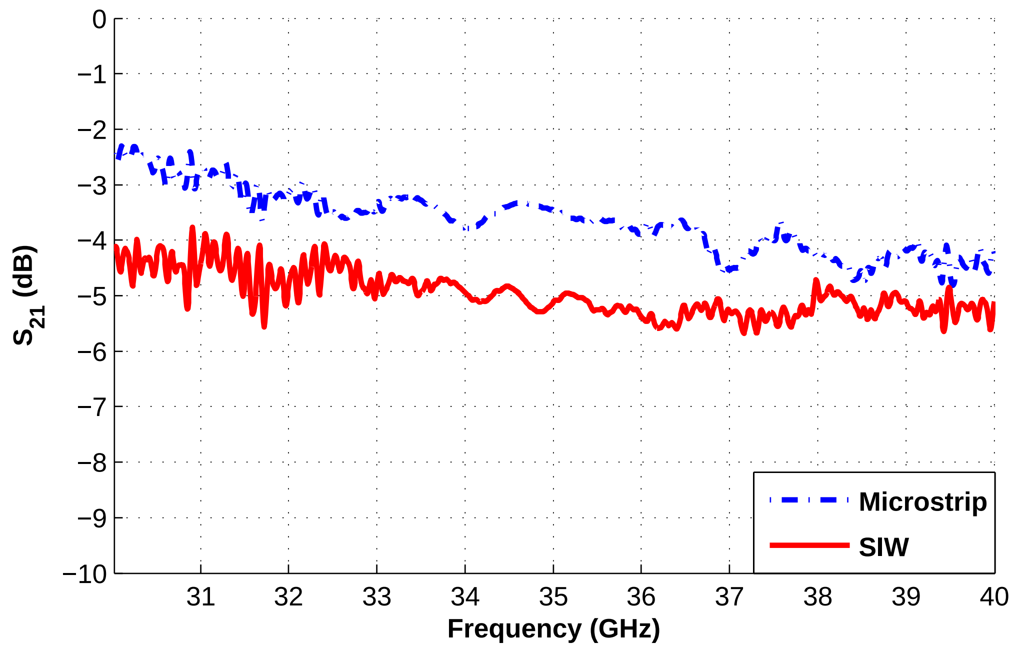

Figure 2.17: S_{21} (insertion loss) measurement results

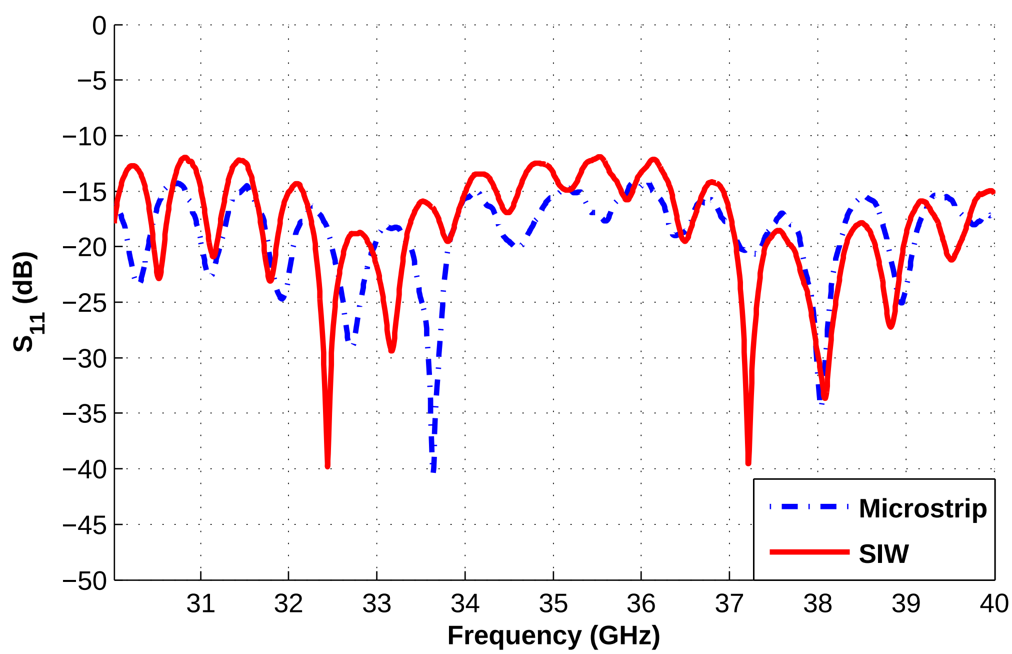

Figure 2.18: S_{11} (return loss) measurement results

Chapter 3

SIW Bandpass Filters

Microwave filters are among the most widely investigated and realized groups of devices with the SIW technology. Consequently, several filter topologies that are compatible with the SIW technology have been proposed and various types of bandpass filters have been designed, analyzed and fabricated [21]-[51]. Therefore, in this chapter, we focus on SIW bandpass filters. As the first part of this chapter, iris type SIW bandpass filters at X and K-bands are investigated. Two prototypes with center frequencies 10 GHz and 21 GHz are designed, analyzed and fabricated. Good agreement between the measured and simulated results are obtained. Then, several CSRR loaded SIW bandpass filters are investigated via simulations around 9 GHz. Small modifications to those exist in the literature are performed to improve the filter response and to ease the fabrication process. Finally, a novel SIW bandpass filter with interdigital type resonators is proposed. A 3^rd order prototype is designed, analyzed and fabricated to operate at 9 GHz with an approximately 500 MHz bandwidth. Dumbbel type DGS is used at the ground part of this filter right below the microstrip based feeding line to suppress the next higher harmonic at 13.5 GHz. Good agreement between the simulation and measurement results are obtained. Furthermore, the proposed filter exhibits good filtering properties with an excellent harmonic suppression at 13.5 GHz.

3.1 Iris Type SIW Bandpass Filters

3.1.1 Theory and Design Equations

In waveguide structures, bandpass filters can be designed by placing inductive irises inside a waveguide (usually air filled waveguide). This topology is easy to manufacture and yields very good filtering properties. A 7^{th} order air filled waveguide iris filter is illustrated in Fig. 3.1, where only the air part inside the waveguide is modelled. In other words, metallic walls of the waveguide is not illustrated in Fig. 3.1.

In this topology, iris walls (see Fig. 3.2) are considered to have a finite thickness, and the two key parameters to be calculated and optimized are so called the window width and the distance between the irises along the waveguide's longitudinal direction. Window width is the separation between two iris walls along the transverse direction of the waveguide and shown with d_i (i= 1, 2,..., n+1) in Fig. 3.2. Similarly, the distance between two irises along the longitudinal direction of the waveguide is shown with l_i (i= 1, 2,..., n) in Fig. 3.2. It is important to note that implementation of this topology to SIW technology is easy as will be explained later.

The first step to design these filters is to determine the element values (also called the g-values) [67] depending on whether a Butterworth or a Chebyshev type filter is to be designed.

In an n^{th} order Butterworth filter, the passband ripple is zero and g-values are found as follows:

$$g_0 = 1 \tag{3.1}$$

$$g_k = 2sin(\frac{(2k-1)\pi}{2n}), \quad k = 2, 3, ..., n \tag{3.2}$$

$$g_{n+1} = 1 \tag{3.3}$$

where g_0 is the source, g_{n+1} is the load and g_k's are the interelement impedances which are normalized with respect to the source impedance.

On the other hand, for an n^{th} order Chebyshev type filter, the passband has some ripples and the g-values are found as follows:

$$g_0 = 1 \tag{3.4}$$

$$g_1 = \frac{2a_1}{\gamma} \tag{3.5}$$

$$g_k = \frac{4a_{k-1}a_k}{b_{k-1}g_{k-1}}, \quad k = 2, 3, ..., n \tag{3.6}$$

$$g_{n+1} = 1 \text{ , } for\ n\ odd \tag{3.7}$$

$$g_{n+1} = coth^2(\frac{\beta}{4}) \text{ , } for\ n\ even \tag{3.8}$$

where

$$a_k = sin(\frac{(2k-1)\pi}{2n}), \quad k = 1, 2, ...n \tag{3.9}$$

$$b_k = \gamma^2 + sin^2(\frac{k\pi}{n}), \quad k = 1, 2, ...n \tag{3.10}$$

and

$$\gamma = sinh(\frac{\beta}{2n}) \tag{3.11}$$

$$\beta = ln(coth(\frac{L_{ar}}{17.37})) \tag{3.12}$$

where L_{ar} being the passband ripple in dB. Remaining variables are used as dummy variables while calculating the g-values.

Once the g-values are found, the air filled waveguide iris filter synthesis method described in [20] can be used. Iris thickness is assumed to be 0 in this method. Therefore, the design obtained using this method should be simulated in a 3-D EM simulation software before manufacturing in order to see the effect of the iris thickness (when iris thickness increases bandwidth decreases, vice versa).

Considering the fact that the order of the filters (Chebyshev or Butterworth) is usually an odd number, the design equations for an air filled waveguide iris bandpass filter are given in (3.13) to (3.21) as follows:

$$f_0 = \sqrt{f_1 f_2} \approx \frac{f_1 + f_2}{2} \tag{3.13}$$

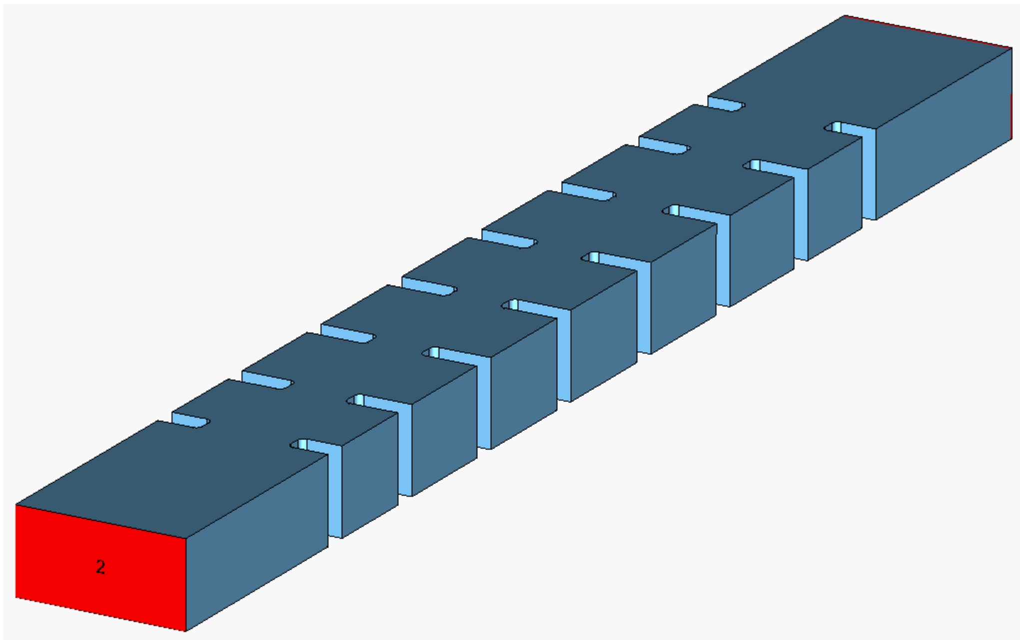

Figure 3.1: Air filled waveguide 7^{th} order iris filter model

where f_1 and f_2 are the band edge frequencies. The corresponding guided wavelengths are given by

$$\lambda_{gi} = \frac{2a}{\sqrt{(\frac{2af_i}{c})^2 - 1}} \ , \quad i = 0, 1, 2 \tag{3.14}$$

where a isthe width of the waveguide and c is the speed of light in free-space.

Then the reactance of the irises ($x_{i,i+1}$) and the electrical length (ϕ_i in radians) between the irises are found as follows:

$$x_{i,i+1} = (\frac{L}{\sqrt{g_i g_{i+1}}})/(1 - \frac{L^2}{g_i g_{i+1}}), \quad i = 0, 1, ...n \tag{3.15}$$

$$\phi_i = \pi - \frac{1}{2}[\tan^{-1}(2x_{i-1,i}) + \tan^{-1}(2x_{i,i+1})], \quad i = 1, 2, ...n \tag{3.16}$$

where L is given by

$$L = \pi \frac{\lambda_{g1} - \lambda_{g2}}{\lambda_{g1} + \lambda_{g2}} \tag{3.17}$$

Having determined the reactances and the electrical lengths between the cavities, these values are used to calculate the iris window width (d_i) and the physical length (l_i) between the irises such that the iris window width (d_i) can be extracted

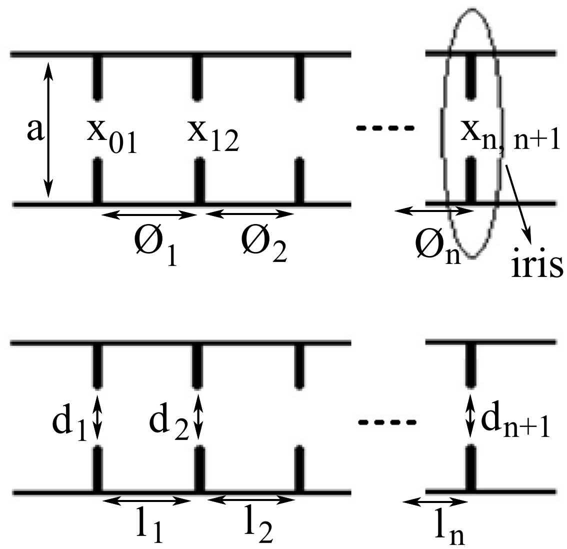

Figure 3.2: Iris type waveguide bandpass filter. The upper one is with the electrical and the below one is with the physical parameters.

from the following equation

$$x_{i-1,i} = \frac{a}{\lambda_{g0}}\{\frac{1}{s_i^2} - 1 - \frac{(1-s_i^2)^2}{1-\delta_3 s_i^6}[3\delta_3 + 5\delta_5 \frac{[2s_i^2 - 1 + \delta_3 s_i^6(s_i^2-2)]^2}{(1-\delta_3 s_i^6)(1-\delta_5 s_i^{10}) - 15 s_i^6 \delta_5 (1-s_i^2)^2}]\} \tag{3.18}$$

where

$$s_i = \sin(\frac{\pi d_i}{2a}), \quad i = 1, 2, ..., n \tag{3.19}$$

and

$$\delta_m = 1 - \sqrt{1 - (\frac{2a}{m\lambda_0})^2}, \quad m = 3, 5 \tag{3.20}$$

Finally, the physical length (l_i) between irises is obtained as follows:

$$l_i = \frac{\lambda_{g0}}{2\pi}\phi_i. \quad i = 1, 2, ..., n. \tag{3.21}$$

It should be noted that if the order of the filter is even (not common) then g_0 and g_{n+1} parameters will not be 1 anymore. They will take the value of

$$g_0 = g_{n+1} = L/R \tag{3.22}$$

where R is given by

$$R = 2k^2 + 1 - 2k\sqrt{1+k^2} \; n \; is \; even \tag{3.23}$$

with k being

$$k = \sqrt{10^{L_{ar}/10} - 1} \tag{3.24}$$

Then, again critical parameters will be found via (3.13) - (3.21).

3.1.2 SIW Iris Filter Design at X and K-Bands

In this section, using the aforementioned design equations, two different 5^{th} order SIW iris bandpass filters (one in X-band and the other in K-band) are designed and fabricated on Rogers TMM10i substrate that has $\epsilon_r = 9.8$, loss tangent 0.002 and thickness 25 mil. High dielectric permittivity materials used in order to obtain a small sized filter. Fig. 3.3 illustrates the filter for X-band whereas Fig. 3.4 shows the designed filter for K-band. Once the waveguide iris filter parameters are determined for an air-filled waveguide (using the aforementioned design equations), the waveguide dimension a is scaled to the SIW dimension a_s, and this scale factor is used to modify the width of the iris windows and the length between the irises so that SIW implementation of the iris filter can be performed. Then, the final values of the critical parameters, such as the iris window width (shown with w_i in Figs. 3.5 and 3.6), and the length between the irises along the longitudinal direction of the SIW (shown with l_i in Figs. 3.5 and 3.6) are optimized for the best performance using CST MWS. Fig 3.5 and Fig. 3.5 show the CST MWS models for the X- and K-band filters, respectively, together with the critical filter parameters a_s, l_i, w_i as well as the matching parameters w_t and l_t.

The final parameters for the fabricated filters are tabulated in Table 3.1 and Table 3.2 for the X- and K-band filters, respectively. In addition to these parameters, the width of the 50 Ω line is 22 mil, each metallic via has a 16 mil diameter and the pitch between the vias is 28 mil. It should be noted that these parameters are measured from the via centers. Both filters have 5 cavity sections (between the 6 iris sections) and hence, they are 5^{th} order filters. Finally Southwest Microwave's 2.92 mm end-launch connectors (previously mentioned in Chapter 2) are used for the measurements.

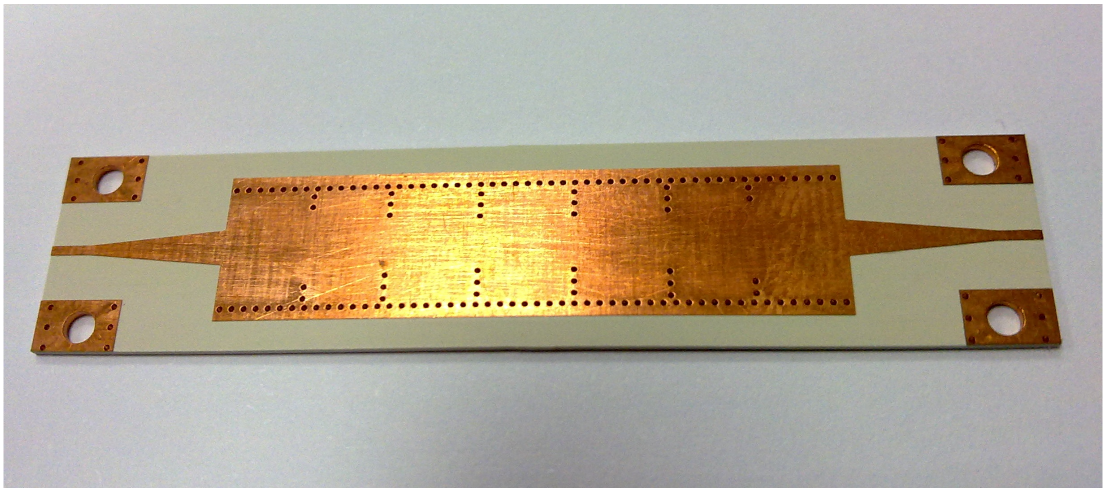

Figure 3.3: SIW iris filter at X-band

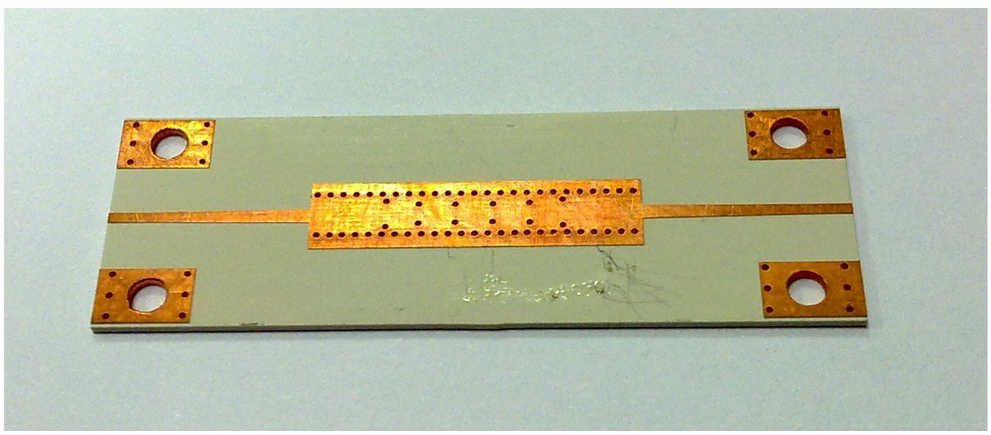

Figure 3.4: SIW iris filter at K-band

Fig. 3.7 shows the measured and simulated S_{11} and S_{21} results of the X-band filter whereas Fig. 3.8 shows the same results for the K-band filter. For both cases, the frequency band is shifted towards lower frequency side in the measured results. This is probably due to the tolerance change in ϵ_r and possible fabrication errors. On the other hand, measured S_{11} is better than -15 dB in the X-band filter and better than -18 dB in the K-band filter and these return loss values are quite sufficient for matching. The bandwidth and the suppression levels agree well with the simulations. In X-band filter, unloaded resonator Q-factor (including dielectric and conductor losses) is found to be 300 at 10 GHz by using CST MWS's Q-calculation tool and this results 1.2 dB loss at 10 GHz

Table 3.1: Dimensions of the X-band SIW iris filter

Parameter	Length (mil)	Parameter	Length (mil)
w_t	85	l_t	325
w_1	183	l_1	169
w_2	134	l_2	199
w_3	120	l_3	205
a_s	297		

Table 3.2: Dimensions of the K-band SIW iris filter

Parameter	Length (mil)	Parameter	Length (mil)
w_t	42	l_t	235
w_1	86	l_1	78
w_2	64	l_2	94
w_3	58	l_3	97
a_s	144		

in the simulations. When measured results are investigated, 1.4 dB insertion loss at the center frequency is obtained and this is an expected result. The 0.2 dB difference between simulated and measured results are most probably caused from the connector losses. For the K-band filter, the unloaded resonator Q-factor is found about 380 which results 1.3 dB loss at 21 GHz in the simulations. In the measured results, the 2.4 dB loss at the center frequency is slightly higher than simulation results. This is most probably caused from the unexpected material losses and radiation loss in addition to connector losses.

3.2 SIW Bandpass Filter with CSRR and DGS

Recently, split ring resonators (SRRs), complementary split ring resonators (CSRRs) and defected ground structures (DGSs) are becoming popular due to their resonant responses, and several novel filter topologies that use these structures have been proposed. Among these structures CSRRs and DGSs can be used in SIW architecture to design novel bandpass filters. Therefore, inspired from the study in [41], X-band SIW bandpass filters are designed and analzed that use CSRRs and dumbbell type DGSs.

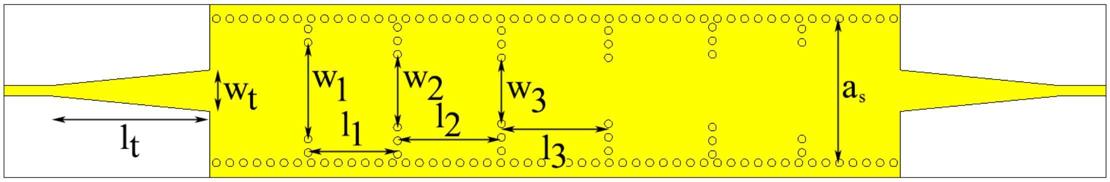

Figure 3.5: CST MWS model for the SIW iris filter at X-band

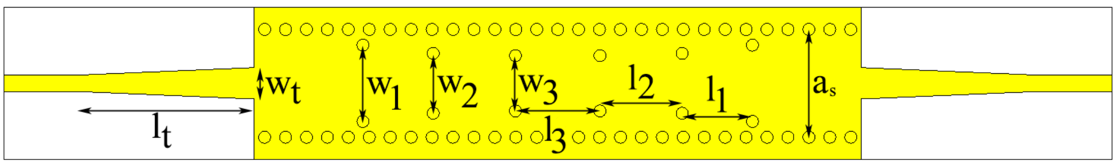

Figure 3.6: CST MWS model for the SIW iris filter at K-band

3.2.1 SIW Bandpass Filter with CSRR Structures

The first design is a SIW bandpass filter that uses CSRRs on the top and bottom part of the SIW section as presented in [41]. The main difference is that we use microstrip lines for the transition to SIW. In [41] double sided parallel stripline (DSPSL) structures are used.

Similar to [41], Rogers 5880 substrate that has a thickness of 20 mil, $\epsilon_r = 2.2$ and a loss tangent of 0.0009 (at 10 GHz) is used. This substrate is widely used in high frequency applications due to its low loss. Besides, it is also used in [41] and we want to compare our results with that of presented in [41]. The 3^{rd} order bandpass filter structure with its important design parameters are illustrated in Fig. 3.9 whereas the detailed view of the CSRR is shown in Fig. 3.10. All critical design parameters are given in Table 3.3. In addition to the parameters listed in Table 3.3, the 50 Ω microstrip line has a width of 58 mil, and as in [41], via diameters are 24 mil and via pitch is 43 mil.

As seen in Fig. 3.9, the orientation of the CSRRs on the upper and bottom sides are adjusted in such a way that the filter provides good suppression as well as good matching. The gap (g) and the split parameters (v) (shown in Fig. 3.10) of the CSRR are kept as small as possible to minimize the radiation loss and are selected to be 10 mil, which is the limiting tolerance of our fabrication

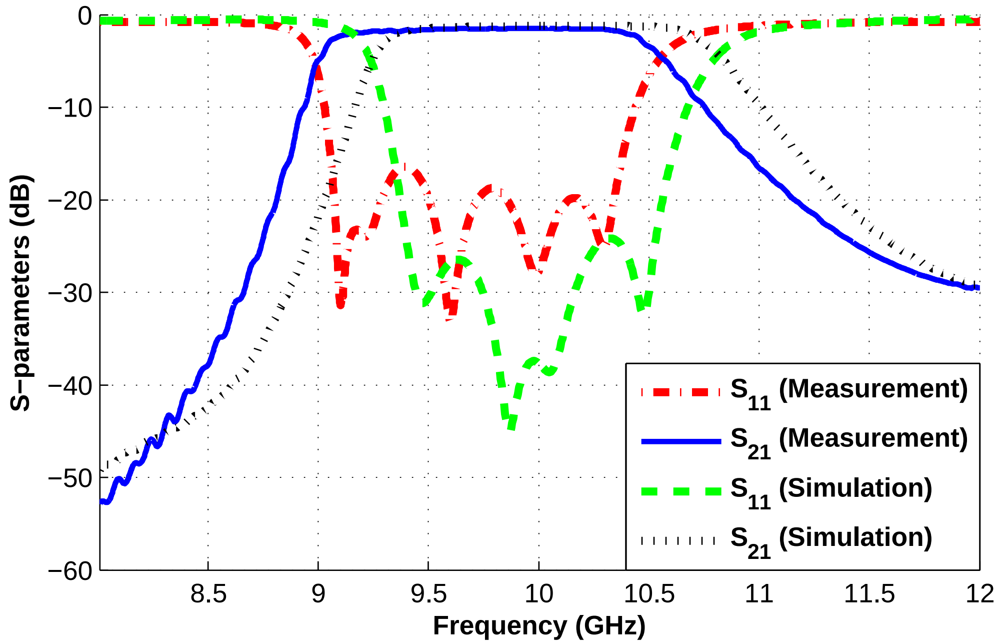

Figure 3.7: Measured and simulated S_{11} and S_{21} for the X-band filter

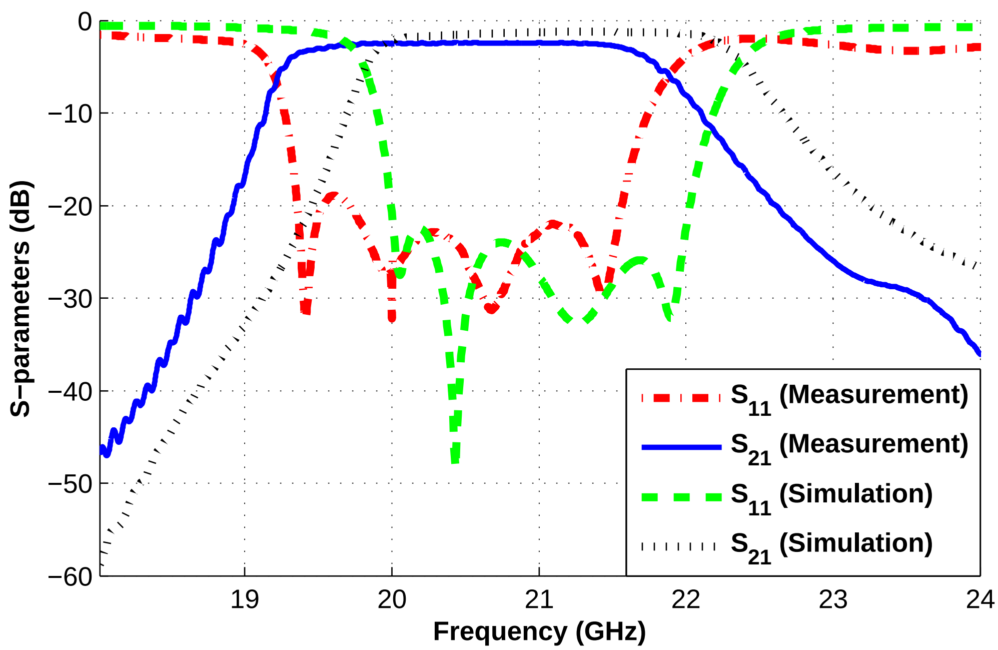

Figure 3.8: Measured and simulated S_{11} and S_{21} for the K-band filter

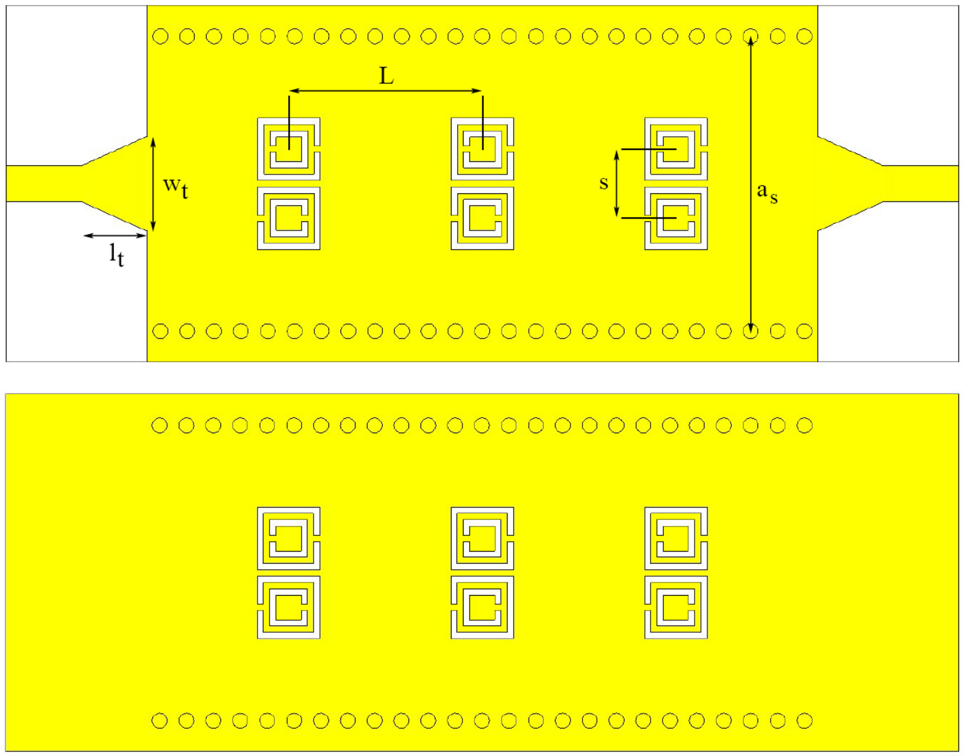

Figure 3.9: Bandpass SIW filter that uses CSRRs. Top figure is the upper side and the bottom figure is the ground side of the filter

facility. The length of the CSRR (L_{csrr}) determines the resonance frequency (center frequency) of the structure, and the separation between the right and left CSRRs affect the matching. On the other hand, the length between the CSRR couples (L) determines the bandwidth of the filter. Increasing L results smaller bandwidth.

The center frequency of this 3^rd order bandpass filter is adjusted to 8.75 GHz and the 1 dB bandwidth is adjusted approximately to 1 GHz. Based on the simulation results shown in Fig. 3.11, the insertion loss at the center frequency is about 0.9 dB and S_{11} is better than -15 dB. Results show that this 3^{rd} order filter has sharp band edges. However, the harmonic band occurring at about 1.5 times of the center frequency is close to the passband which is not desired. When these results are compared with [41], insertion and return loss results, and the harmonic band occurring at 1.5 times of the center frequency are similar. In order to carry the harmonic band to a higher frequency, in [41] dumbbell type DGS is

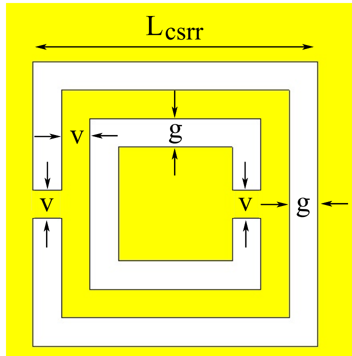

Figure 3.10: CSRR structure

Table 3.3: Dimensions of the SIW bandpass filter with CSRR

Parameter	Length (mil)	Parameter	Length (mil)
w_t	152	l_t	105
L	310	s	110
g	10	v	10
a_s	472	L_{csrr}	100

used at the ground of the filter instead of CSRR which is also studied in the next sub-section.

3.2.2 SIW Bandpass Filter with CSRR and Dumbbell Structures

In order to improve the harmonic behaviour of the filter, dumbbell type DGS is used at the ground side of the filter. The substrate as well as the SIW parameters (i.e., a_s, via diameters, pitch size, etc.) are kept the same. The order of the filter is also kept same. However, certain parameters are changed and hence, the center frequency of the filter is 9.6 GHz. The upper (signal) side of the filter is the same as the previous case. However, dumbbell type DGS is introduced to the ground side of the SIW as illustrated in Fig. 3.12, which also shows the critical parameters of the dumbbells. Each dumbbell is placed exactly under the corresponding CSRR pair. Final filter dimensions are given in Table 3.4.

Simulated S-parameter results of the final filter is illustrated in Fig. 3.13. As

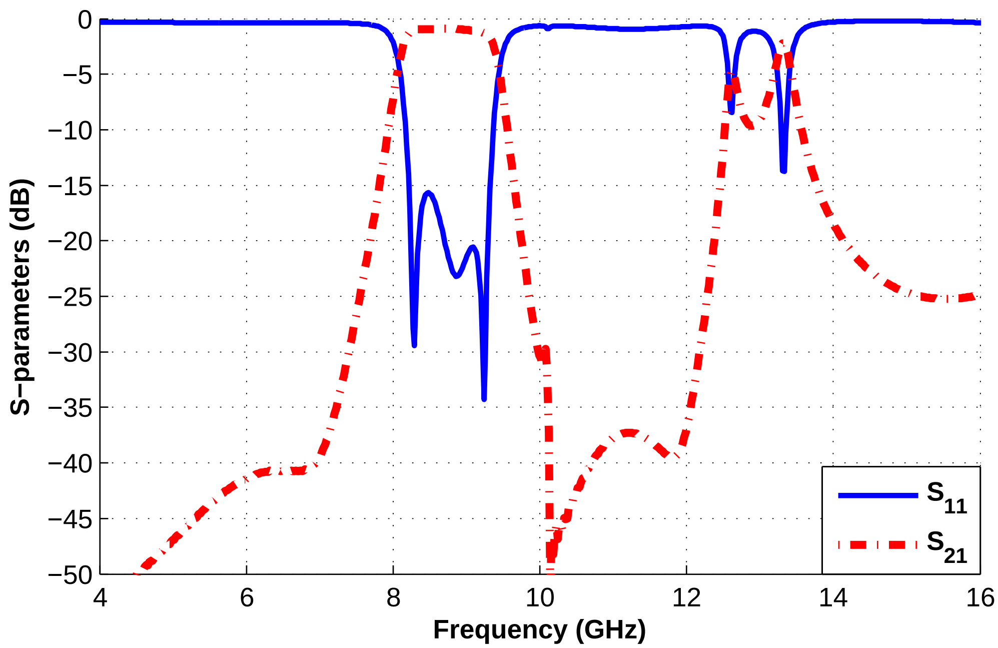

Figure 3.11: Simulated S_{11} and S_{21} results of the 3^{rd} order SIW filter that uses CSRRs

seen in the results, the center frequency is 9.6 GHz and the 1 dB bandwidth of the filter is about 1.9 GHz. Although the filter is designed with the similar CSRR parameters as in the previous case, effect of the dumbbells results a higher bandwidth. Hence, the increase in the bandwidth results a decrease in the insertion loss to 0.6 dB. The sharpness of the filter edges are almost same, but when the harmonics are investigated a significant improvement is observed. In the previous structure (where CSRRs are used in both sides), the next higher order harmonic is at $1.5f_0$ (f_0 : center frequency) which is quite close to the passband. However, replacing the CSRRs at the ground side of the SIW with dumbbell type resonators results the next higher order harmonic to occur at $2f_0$.

When these final results are compared with that of [41], filter insertion and return losses are similar. Furthermore, the next higher harmonic band occurs beyond $2f_0$ which is similar to our results.

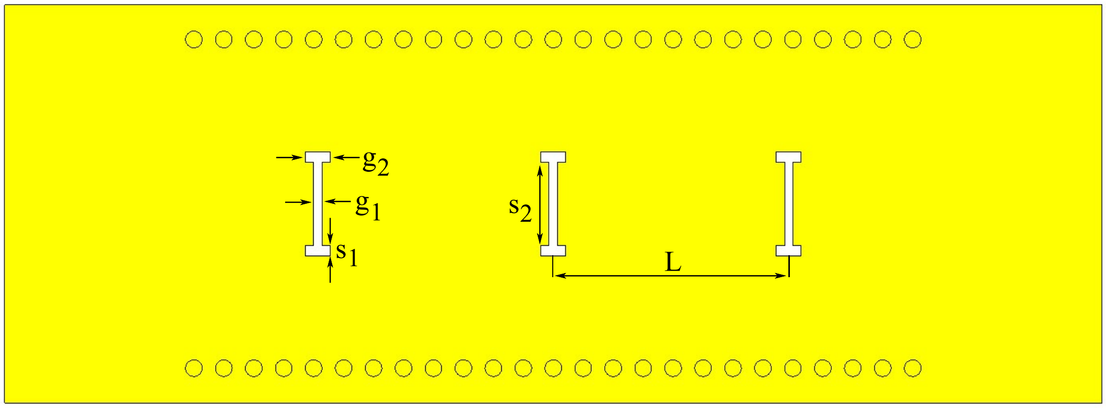

Figure 3.12: Bottom view of the SIW filter with CSRR and dumbbell.

Table 3.4: Dimensions of the SIW bandpass filter with CSRR and dumbbell

Parameter	Length (mil)	Parameter	Length (mil)
w_t	95	l_t	130
L	338	s	108
g	10	v	10
g_1	12	g_2	36
s_1	15	s_2	120
a_s	472	L_{csrr}	98

3.3 Novel SIW Based Interdigital Filter with Harmonic Suppression

As mentioned in the previous sections, resonant structures are used in order to obtain filter responses in microwave applications. Many different filter topologies have been built with different kinds of resonators like CSRRs, dumbbells, SRRs, etc. Recently, a coplanar waveguide-fed combline SIW filter has been proposed in [18], where each combline SIW resonator is formed from a metallic via short-circuited at the bottom metallization and open ended at the top. Hence, a capacitance is established between a metallic disk, connected to the via, and the top metallization of the SIW cavity through the fringing fields across an annular gap etched on the metal. These resonators are then placed with some distance to each other in order to obtain the desired filter response.

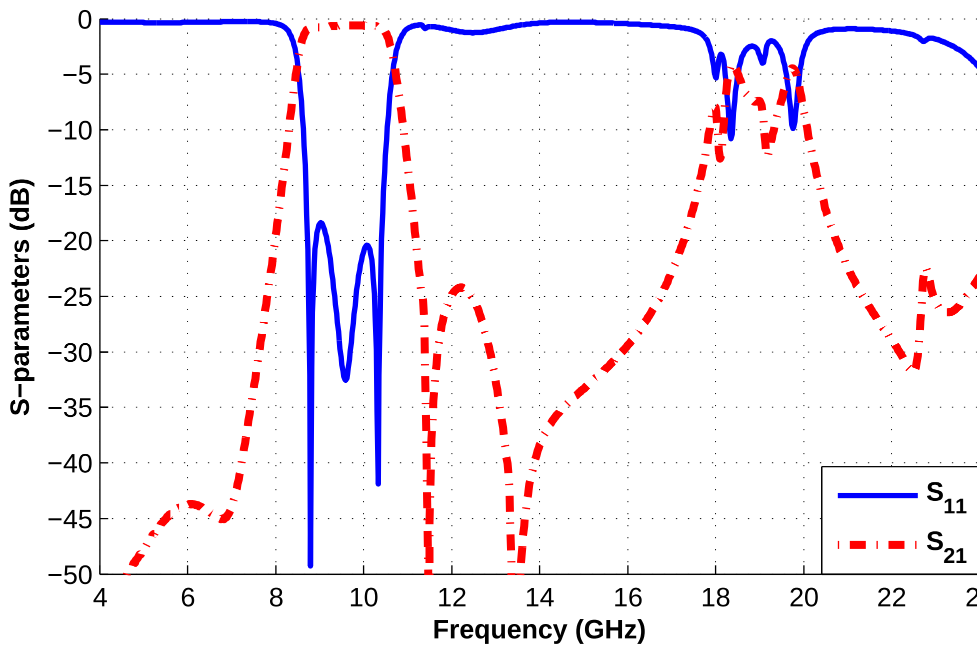

Figure 3.13: Simulated S_{11} and S_{21} results of the SIW filter with CSRR and dumbbell

In this study, inspired from [18], a novel filter topology for SIW bandpass filter with interdigital configurated resonators is suggested and harmonics are suppressed by using a dumbbell type DGS. The first step of the design is to determine the width of the SIW section (recall that the width, a_s, determines the cut-off frequency of the SIW section) together with a microstrip tapered transition. Microstrip tapered transition is preferred because achieving wideband matching is simpler with this kind of transition as shown in Chapter 2 and as suggested in [11]. After determining the initial SIW dimensions together with the microstrip tapered transition, a resonator is formed at the center of the filter as illustrated in Fig. 3.14. Similar to [18], this resonator is formed from a metallic via short-circuited at the bottom metallization and open-ended with the cap at the top. The diameter of the via is 16 mil (standard via (drill) dimension) and the radius of the cap (metallic portion at the open-ended part) is an optimization parameter as its size mainly determines the upper cut-off frequency of the passband. An annular gap, whose gap width is 10 mil, is etched on the metal and it separates the cap from the rest of the metallization on the top metal surface of

Table 3.5: Effect of cap radius to the upper cut-off frequency

Radius (mil)	Frequency (GHz)
50	10.1
52.5	9.66
55	9.16
57.5	8.63
60	8.37

the SIW. Besides, the diameter of all other metallic vias is 16 mil and the pitch size is 28 mil (similar to all previous designs in this thesis). Note that these sizes are from the centers of the vias.

Because the radius of the cap affects (mainly determines) the upper cut-off frequency, initially it is set to 55 mil as it leads the upper cut-off frequency to occur around 9.16 GHz as shown in Fig. 3.15. Then using the Rogers TMM10i substrate ($\epsilon_r = 9.8$, loss tangent = 0.002, thickness = 25 mil, 50 Ω microstrip width = 22 mil), effects of the cap radius on the upper cut-off frequency is investigated by varying the cap radius from 50 mil to 60 mil with increments of 2.5 mil. The simulated S_{21} versus frequency results for varying cap radius are shown in Fig. 3.16. As seen from the figure, an increase in the radius results a shift in the 3 dB cut-off frequency through the lower frequency side. Cap radius of the resonators versus the corresponding upper cut-off frequency results are tabulated in Table 3.5.

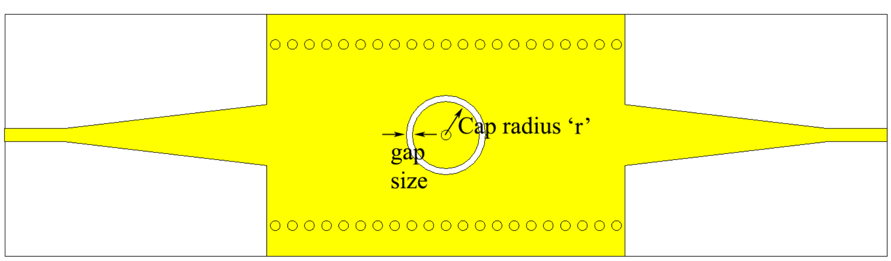

Figure 3.14: Single resonator in the SIW

Once the single resonator filter is designed, the order of the filter is increased by adding more resonators (number of resonators determines the order of the filter). Each resonator has the same geometry as depicted in Fig. 3.14. However, because an interdigital type configuration is aimed, resonators are reversed with

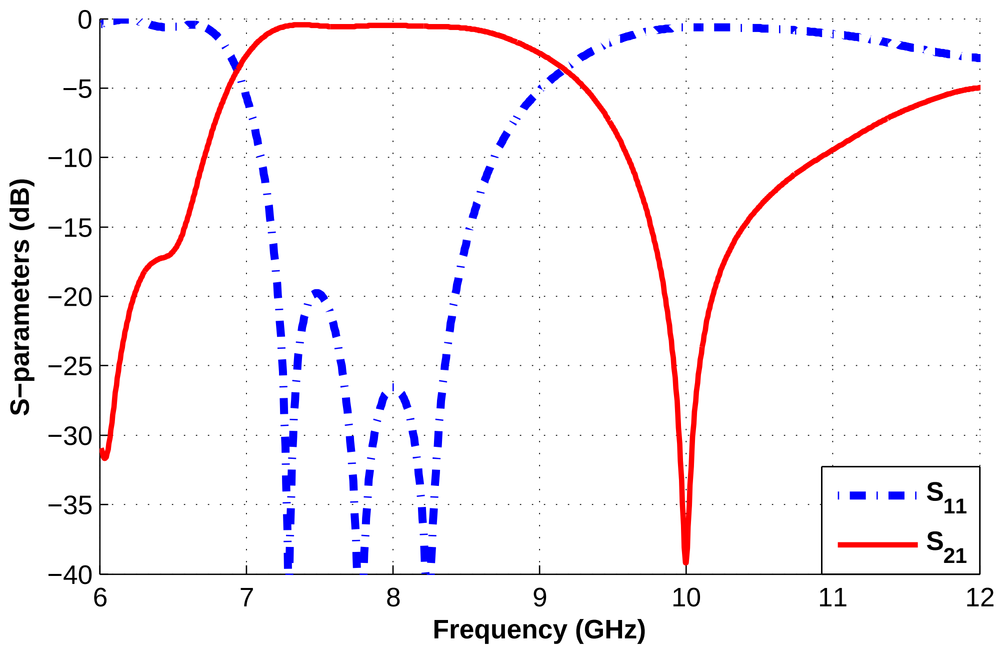

Figure 3.15: Simulated S_{11} and S_{21} results of a single resonator in the SIW

Table 3.6: Dimensions of the 3^{rd} order SIW interdigital filter in Fig. 3.17

Parameter	Length (mil)	Parameter	Length (mil)
w_t	100	l_t	330
d_1	110	d_2	110
a_s	297		

respect to each other in such a way that for a third order filter, the middle resonator's cap together with the annular gap is on the top (i.e., signal) metallic surface of the SIW whereas the first and third resonators' caps (together with the corresponding annular gaps) are on the bottom (i.e., ground) metallic surface of the SIW. Fig. 3.17 shows the top and bottom views of these three resonators in the filter. Note that interdigital and combline filters are usually symmetric. Therefore, the dimensions of the left and right (i.e., the first and the third) resonators as well as their center to center distance from the middle (i.e., second) resonator is the same. Also note that the distance between the resonators mainly affects the bandwidth and matching. Fig. 3.18 shows the simulated S_{11} and S_{21} results of the 3^{rd} order filter depicted in Fig. 3.17 with the parameters tabulated in Table 3.6.

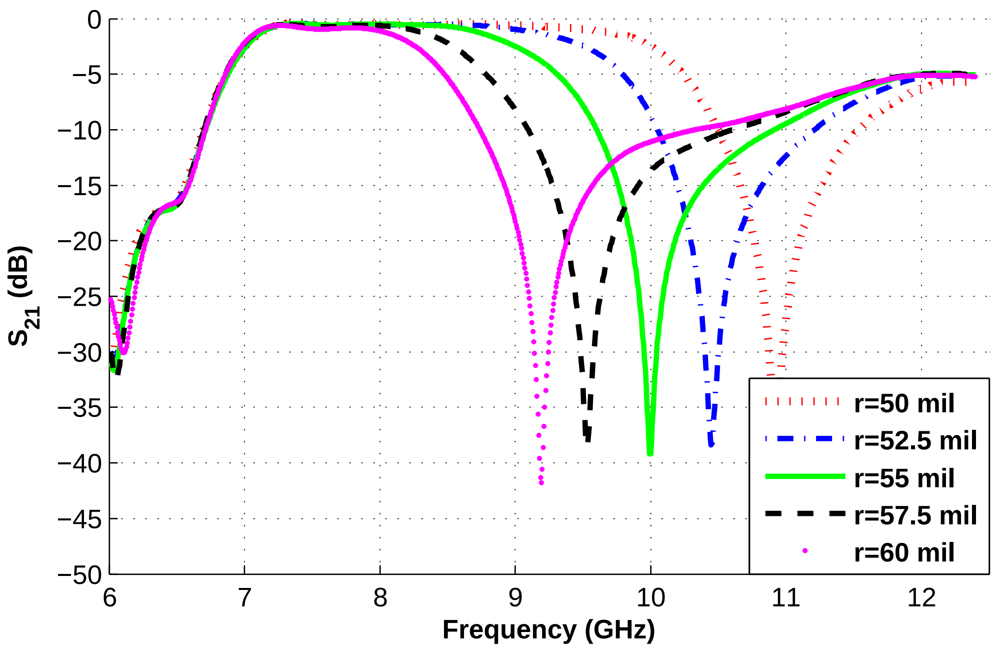

Figure 3.16: Simulated S_{21} versus frequency for varying cap radius

As seen in Fig. 3.18, a wideband response is obtained with the center frequency being around 8 GHz. Although the wideband is desirable for certain applications, the return loss level is not attractive (S_{11} is aimed less than -20 dB in the simulations), and an extra control mechanism on the center frequency of the filter is desired since the aimed center frequency is around 9 GHz.

Therefore, to control the amount of frequency shift (towards the lower frequency side because the upper 3dB cut-off frequency may shift towards the lower frequency side) and to improve the matching, the width of the filter is narrowed at the center part of the structure as seen in Fig. 3.19 and a_s is also decreased. Even if a_s is kept the same, narrowing at the center of SIW will shift the frequency towards the upper frequency side but a little decrease in a_s provides better matching. As a result of this modification, the lower cut-off frequency of the filter is shifted to a higher frequency, and the matching is improved in the expanse of a narrower bandwidth as seen in Fig. 3.20 for the parameters tabulated in Table 3.7.

However as seen in Fig. 3.20, the high frequency suppression of the filter is

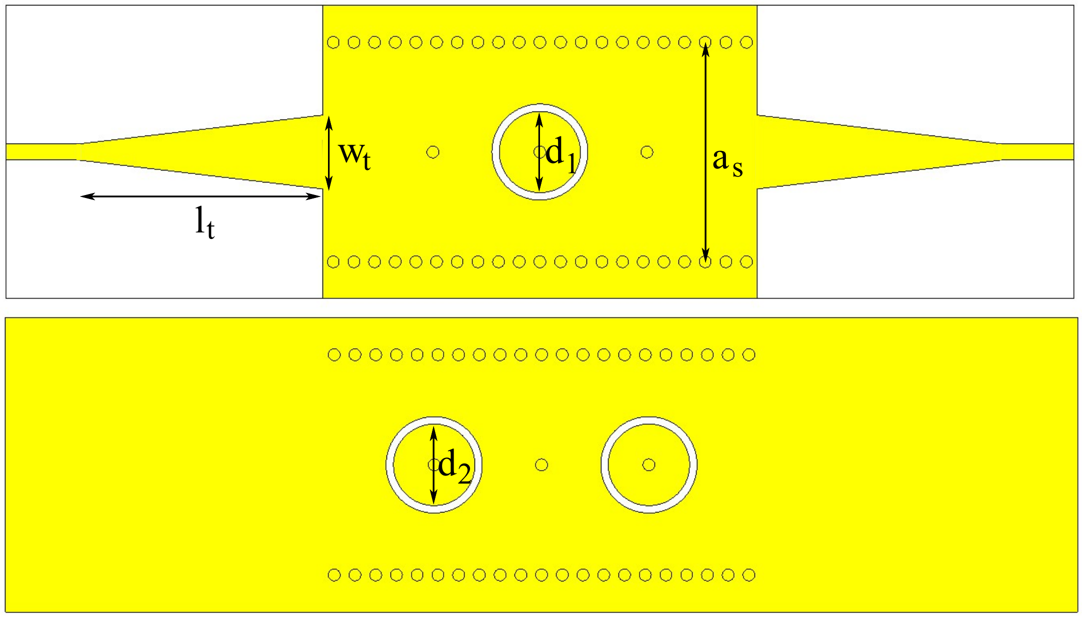

Figure 3.17: Top (up) and bottom (below) surfaces of the three resonators in the filter

Table 3.7: Dimensions of the 3^{rd} order modified filter seen in Fig. 3.19

Parameter	Length (mil)	Parameter	Length (mil)
w_t	100	l_t	330
d_1	110	d_2	109
a_s	290	a_2	202

better than that of the low frequency side. Therefore, to obtain a more symmetrical filter response, additional vias are added to the input and output of the SIW section as depicted in Fig. 3.21. The final design parameters for the filter depicted in Fig. 3.21 are given in Table 3.8. As in the previous designs, the substrate, and hence the width of the 50 Ω line as well as the via diameter and the pitch length are kept the same.

Fig. 3.22 shows the measured and simulated S_{11} and S_{21} results of the filter depicted in Fig. 3.21, whose parameters are tabulated in Table 3.8. The measured results agree well with the simulations in terms of the center frequency, bandwidth and return loss. However, the measured insertion loss is about 2 dB at the center frequency which is 1 dB more than the simulation results. In the simulations, unloaded resonator Q-factor is found 290 (by using CST MWS's Q-Calculation

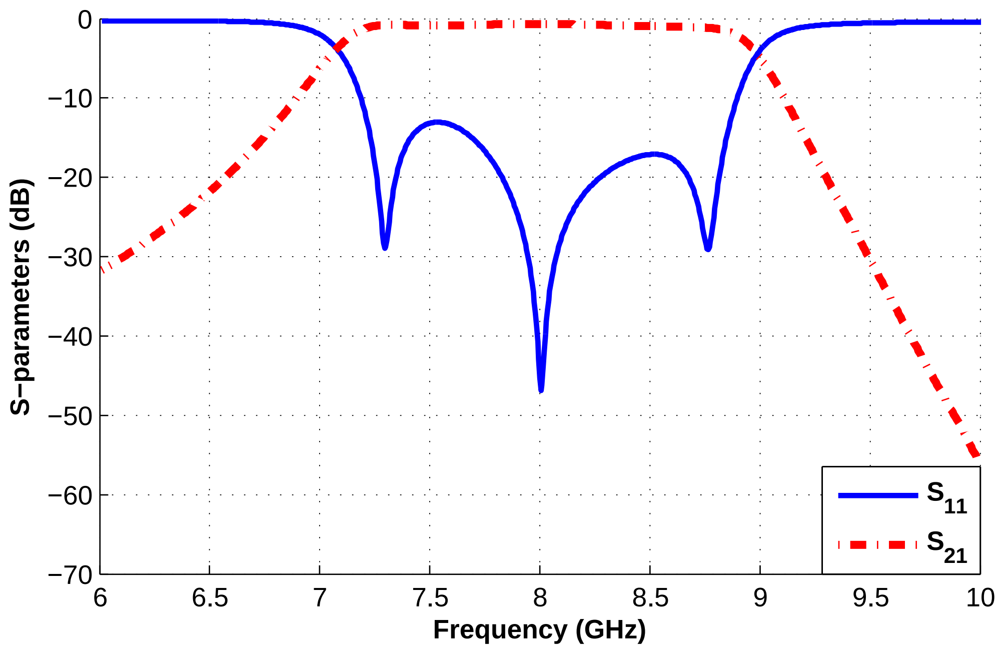

Figure 3.18: Simulated S_{11} and S_{21} results of the 3^{rd} order filter depicted in Fig. 3.17 with the parameters tabulated in Table 3.6

Table 3.8: Dimensions of the final SIW interdigital filter

Parameter	Length (mil)	Parameter	Length (mil)
w_t	100	l_t	330
d_1	110.5	d_2	108
a_1	224	a_2	196
a_s	284	l_1	100

tool) which results a 1 dB insertion loss at 9 GHz. Most probably, the main reason of this difference is the connector losses and unexpected material losses that are not included in the simulations.

In order to compare the performance of this novel filter with other types of filters available in the literature, SIW iris filter topology is chosen as a reference filter and a 3^{rd} order SIW iris filter is designed at the same center frequency, by using the same substrate. The designed 3^{rd} order SIW iris filter is illustrated in Fig. 3.23 and its dimensions (measured from via centers) are given in Table 3.9. Similar to the proposed interdigital filter, this SIW iris filter is also designed by using vias that have 16 mil diameter and the pitch length is 28 mil. For a fair

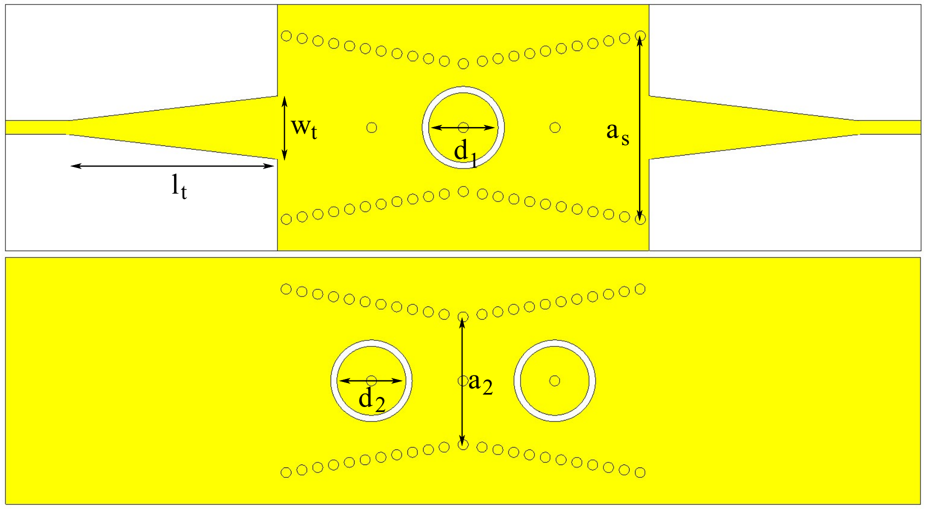

Figure 3.19: Top (up) and bottom (below) surfaces of the modified filter

Table 3.9: Dimensions of the 3^{rd} order SIW iris filter

Parameter	Length (mil)	Parameter	Length (mil)
w_t	85	l_t	325
w_1	183	w_2	136
l_1	249	l_2	276
a_s	297		

comparison, only the filter sections are measured (transition parts are ommitted). The length of the filter section for the SIW iris filter (shown with L in Fig. 3.23) is 774 mil whereas it is 560 mil for the SIW interdigital filter proposed in this thesis. Hence, approximately 28 % reduction is achieved. Moreover, when the simulated S_{11} and S_{21} responses of these two filters are compared (shown in Fig. 3.24), it has been observed that the proposed interdigital filter has a better suppression at the high frequency side. The return and insertion losses are similar. The suppression at the low frequency side is also comparable. As a result, the proposed filter has a better selectivity and it is more compact compared to the SIW iris filter.

Fig. 3.25 shows the measured and simulated S_{11} and S_{21} results of the proposed SIW interdigital filter depicted in Fig. 3.21 with the final design parameters tabulated in Table 3.8. There is a good agreement between the measurements and simulations. However, the next higher order harmonic of the proposed filter is around 13.5 GHz (i.e., $1.5f_0$) as shown in Fig. 3.25. Because the higher

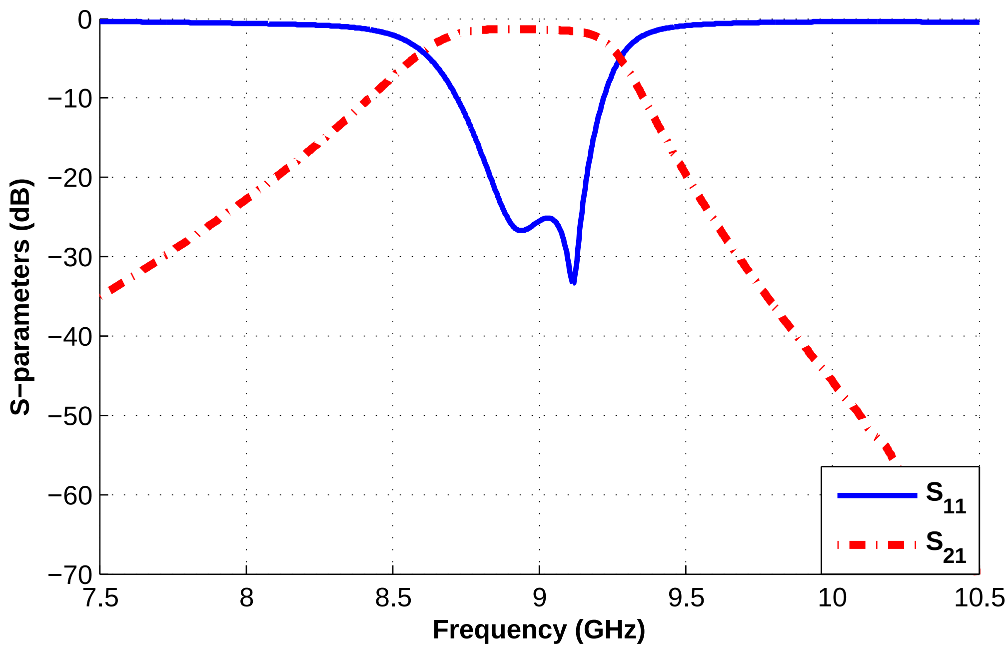

Figure 3.20: Simulated S_{11} and S_{21} results of the modified 3^{rd} order filter depicted in Fig. 3.19 with the parameters tabulated in Table 3.7

order harmonics are undesired frequency components, they must be suppressed as much as possible by giving priority to the ones closer to the center frequency. Hence, in this study, we have decided to use dumbbell type DGS to suppress the harmonic appearing around 13.5 GHz. First, the response of a single dumbbell (named as 1^{st} order dumbbell DGS) etched on the ground plane of a 50 Ω microstrip line, shown in Fig. 3.26, is investigated. Dumbbell heads located at two ends of the architecture are in square shape and each side (labelled with h) has a length of 20 mil. The size of the dumbbell heads mainly affects the matching. On the other hand, the long slot connecting the heads has a length (L) of 140 mil and a width (w) of 10 mil, and this part mainly determines the frequency to be suppressed. Fig. 3.27 shows the simulated S_{11} and S_{21} results of the 1^{st} order dumbbell DGS depicted in Fig. 3.26. The substrate used in these simulations is Rogers TMM10i, as in the filter (with ϵ_r = 9.8, loss tangent = 0.002 and thickness = 25 mil). The width (w_m) of the 50 Ω line is 22 mil. As seen in Fig. 3.27, the presence of the dumbbell DGS stops the signal around 14 GHz. However, its matching (i.e., S_{11}) is not sufficient for practical requirements. Therefore, as the

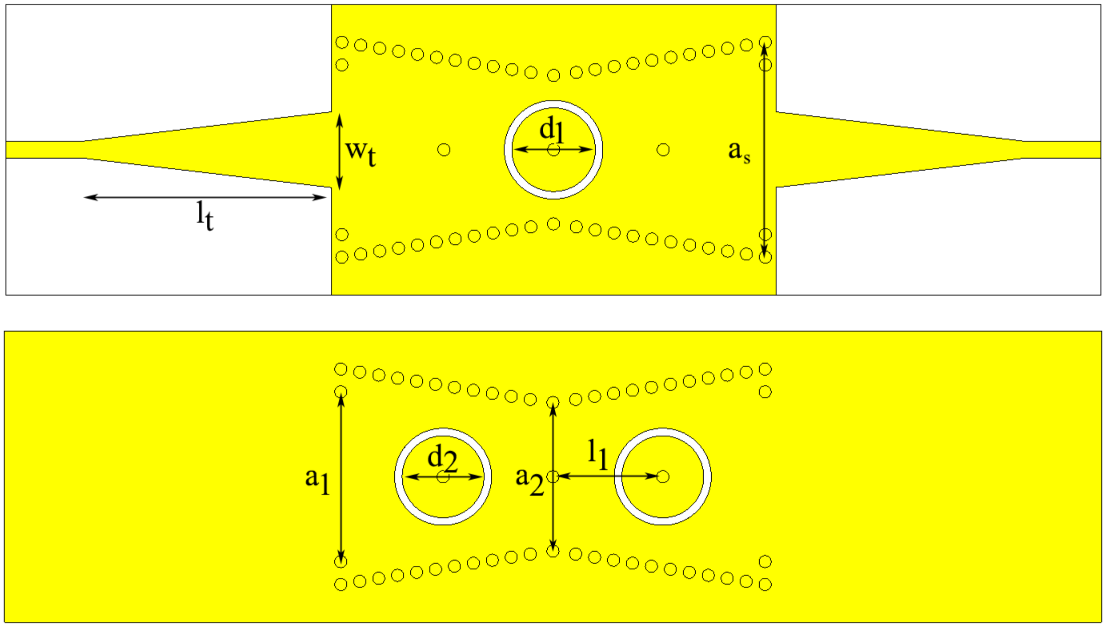

Figure 3.21: Top (up) and bottom (below) views of the final SIW interdigital filter

Table 3.10: Dimensions of the dumbbell type resonators

Parameter	Length (mil)	Parameter	Length (mil)
L	140	g	52
h	20	w	10

next step, the number of dumbbells is increased and a 3^{rd} order dumbbell type DGS, illustrated in Fig. 3.28, that has the same dumbbell dimensions as that of the 1^{st} order case is designed using the same substrate. The separation between each dumbbell is optimized for the best performance and finally it is set to 52 mil. The simulated S_{11} and S_{21} results of the 3^{rd} order dumbbell DGS are given in Fig. 3.29. Clearly a much better rejection around the desired frequency over a wider band is achieved while the S_{11} around this band is also improved.

Fig. 3.30 shows the bottom surface of the realized 3^{rd} order SIW interdigital filter together with the dumbbell type DGS, where the dumbbells are under the 50 Ω microstrip lines at the input and output ports. The final dimensions of the dumbbell resonators are given in Table 3.10.

The manufactured filters (with and without the dumbbell type DGS), seen

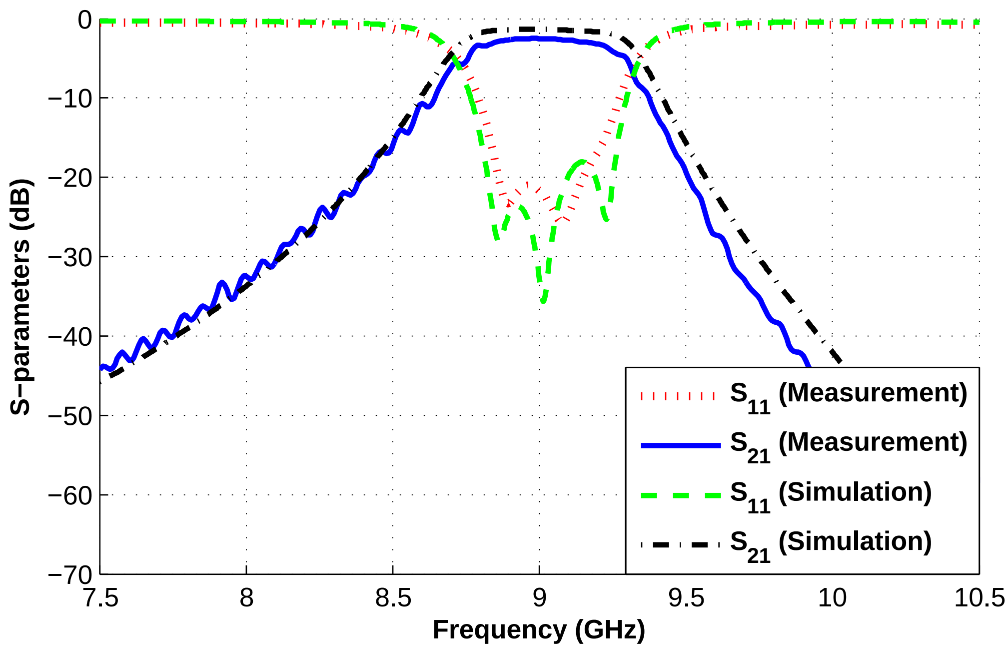

Figure 3.22: Measured and simulated S_{11} and S_{21} results of the 3^{rd} order SIW interdigital filter depicted in Fig. 3.21 for the final parameters tabulated in Table 3.8

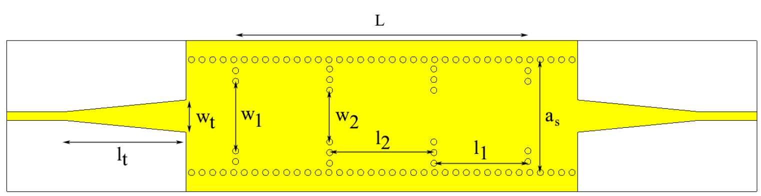

Figure 3.23: A 3^{rd} order SIW iris filter at 9 GHz

in Fig. 3.31, are measured with end launch connectors of Southwest Microwave. The longer filter has the dumbbell type DGS and the shorter one does not have DGS. Using DGS results the microstrip feeding sections to be longer, but if harmonic suppression is important, then this trade-off should be taken into account. Simulation and measurement results for the filter with the dumbbell type DGS are given in Fig. 3.32. Matching, insertion loss, bandwidth and suppression beyond cut-off frequencies are as expected in the simulations, and also the harmonic band around 13.5 GHz is suppressed about 30 dB.

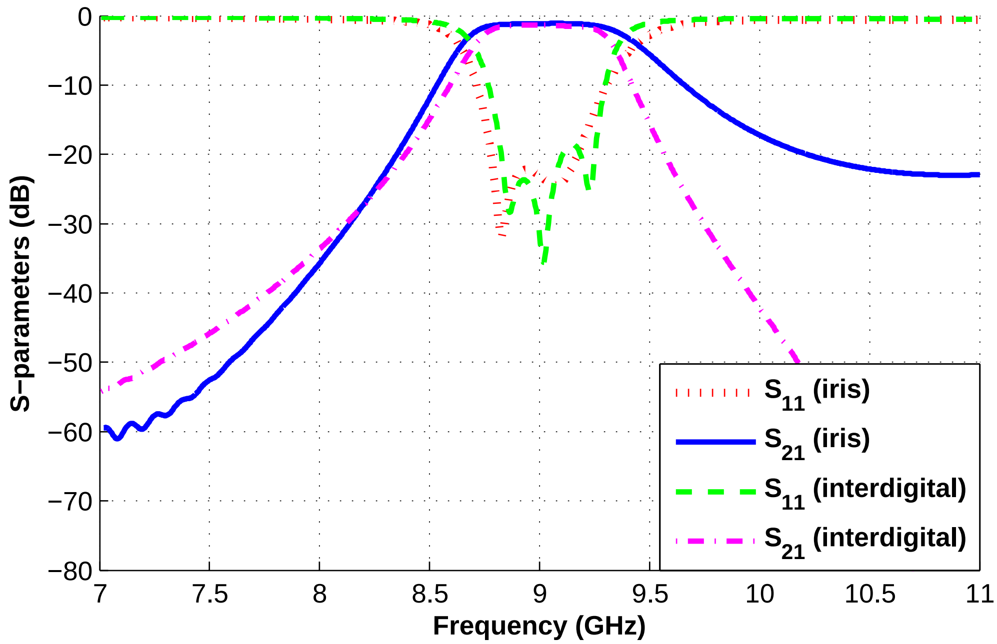

Figure 3.24: Simulated S_{11} and S_{21} results of both the SIW interdigital filter and the SIW iris filter with the parameters tabulated in Table 3.8 and 3.9, respectively.

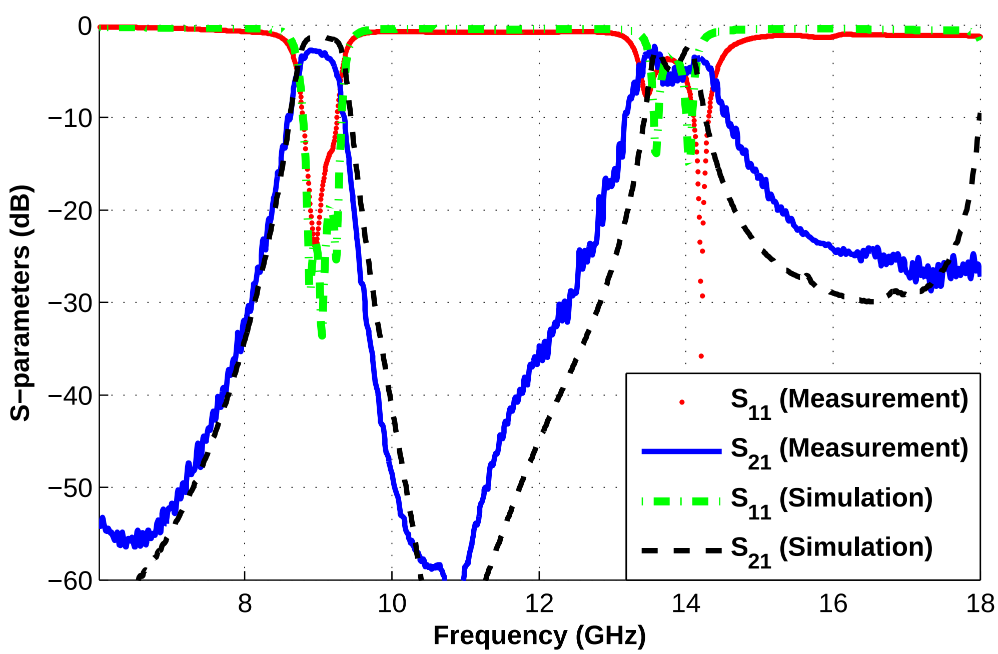

Figure 3.25: Measured and simulated S_{11} and S_{21} results of the proposed SIW interdigital filter depicted in Fig. 3.21 for the final parameters tabulated in Table 3.8

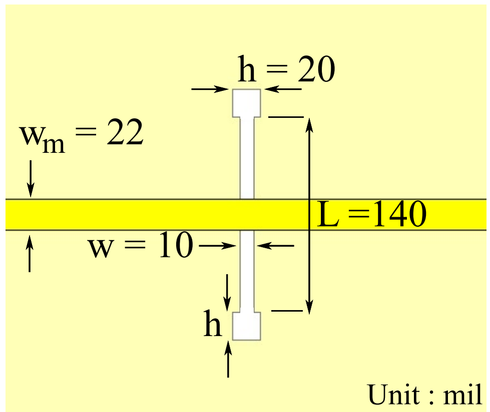

Figure 3.26: 1^{st} order dumbbell DGS

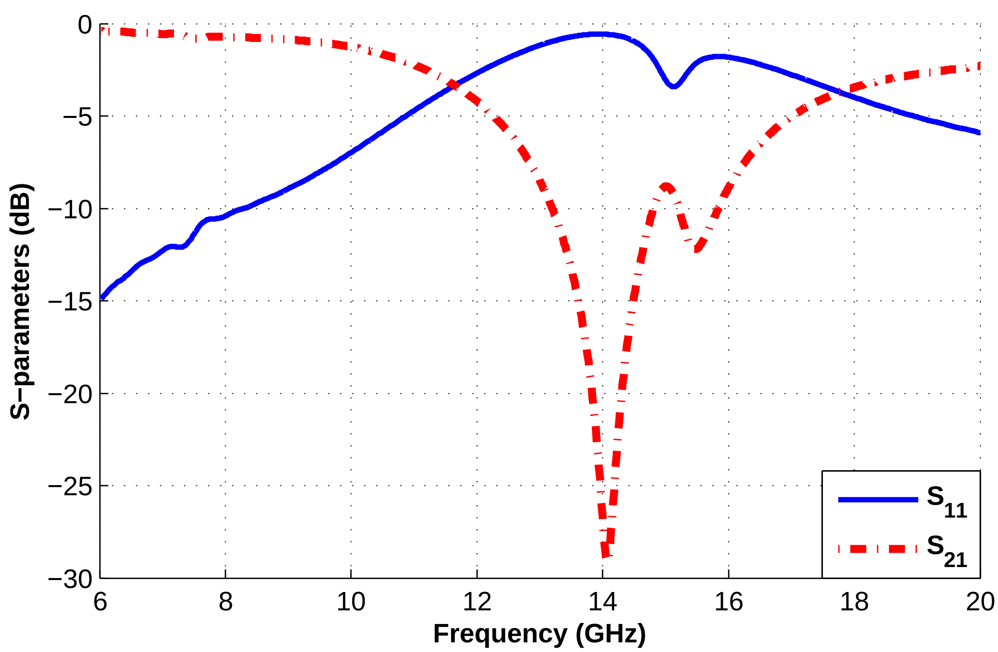

Figure 3.27: Simulated S_{11} and S_{21} results of the 1^{st} order dumbbell DGS

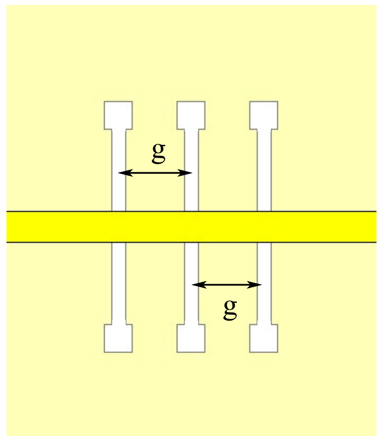

Figure 3.28: 3^{rd} order dumbbell DGS

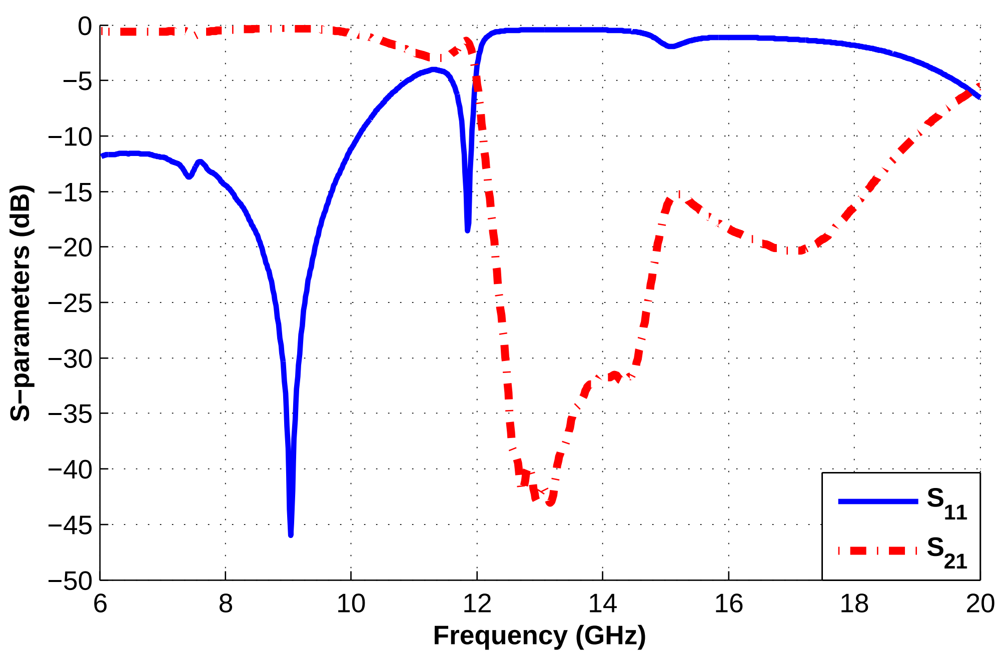

Figure 3.29: Simulated S_{11} and S_{21} results of the 3^{rd} order dumbbell DGS

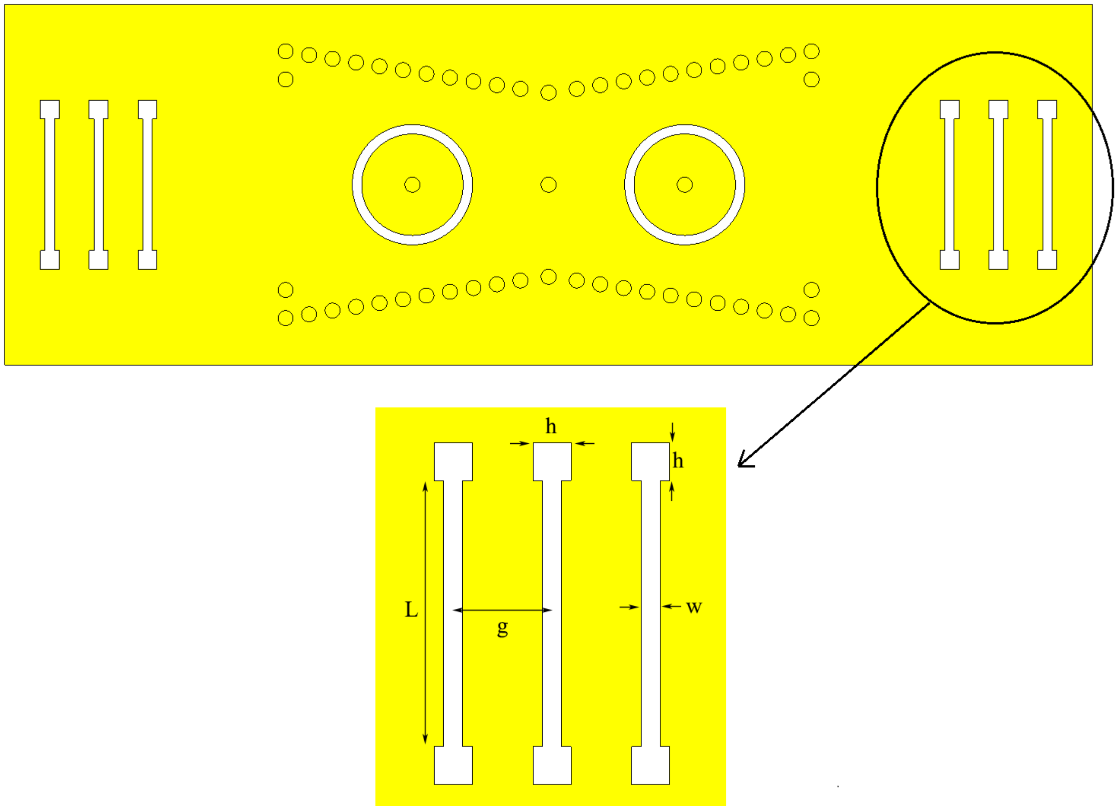

Figure 3.30: Bottom surface of the 3^{rd} order SIW interdigital filter with the dumbbell type DGS

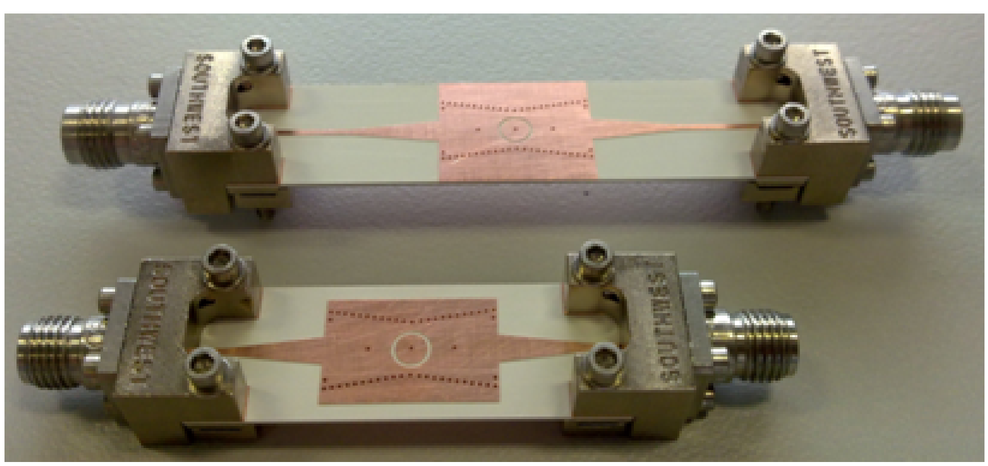

Figure 3.31: Manufactured filter images. The longer filter is with the dumbbell type DGS whereas the shorter filter does not have the dumbbell type DGS.

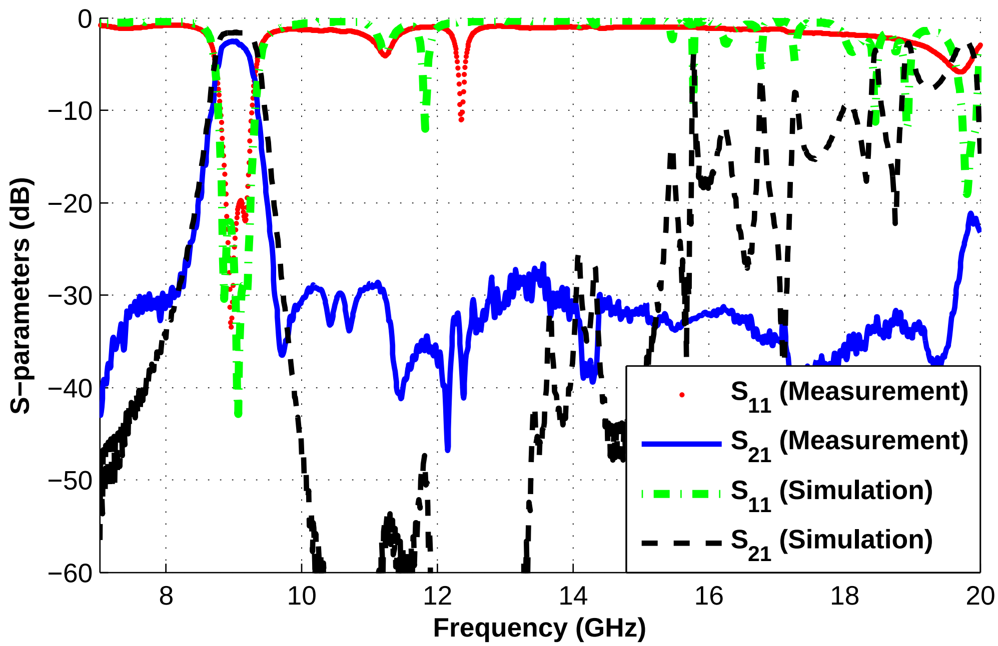

Figure 3.32: Simulated and measured S_{11} and S_{21} results of the filter with the dumbbell DGS

Chapter 4

SIW Power Dividers

SIW based power dividers have been very popular in recent years due to their compact size, light weight and high isolation compared to waveguide power dividers. They are widely used in antenna feeding networks, amplifier applications, etc. in order to obtain multiple copies of the same signal. As a result, several types of SIW power divider/combiners have been presented in the literature [54]-[65].

In this chapter, we first focus on two of the widely used SIW based power dividers, namely T-junction and Y-junction [1] SIW power dividers. In T-junction, the output arms are configured in such a way that they are in reverse direction (as the top of letter 'T') with respect to each other. In Y-junction, the output arms are configured to be in the same direction (as the top of letter 'Y'). Then, we propose a novel power divider structure with high isolation using corrugated SIW (CSIW) architecture (presented in [52], [53]), where open-circuit quarter-wavelength microstrip stubs are used in place of vias to form the side walls of the SIW.

4.1 T-junction SIW Power Divider

In this section, the design of a T-junction SIW power divider at X-band whose output arms are in reverse directions with respect to each other, as illustrated in Fig. 4.1, is presented. In Fig. 4.1, the input port is labelled with number 1, and the output ports are labelled with 2 and 3. The structure is designed on Rogers TMM10i substrate that has a thickness of 25 mil, 9.8 ϵ_r and loss tangent of 0.002. The width of 50 Ω lines is 22 mil, all metallic vias have 16 mil diameter and the separation between the adjacent vias is 28 mil. The final design parameters for the design seen in Fig. 4.1 are given in Table 4.1.

In this divider, the tapered microstrip transition is designed for test purposes. The taper parameters are width w_t and length l_t. Having met the microstrip to SIW matching requirements, the structure is divided into two arms (2 and 3) with the same SIW width a_s and then the outputs are matched to corresponding microstrip lines. In order to satisfy the matching requirements, via positions (g and w) at the junction of the input and output arms are optimized.

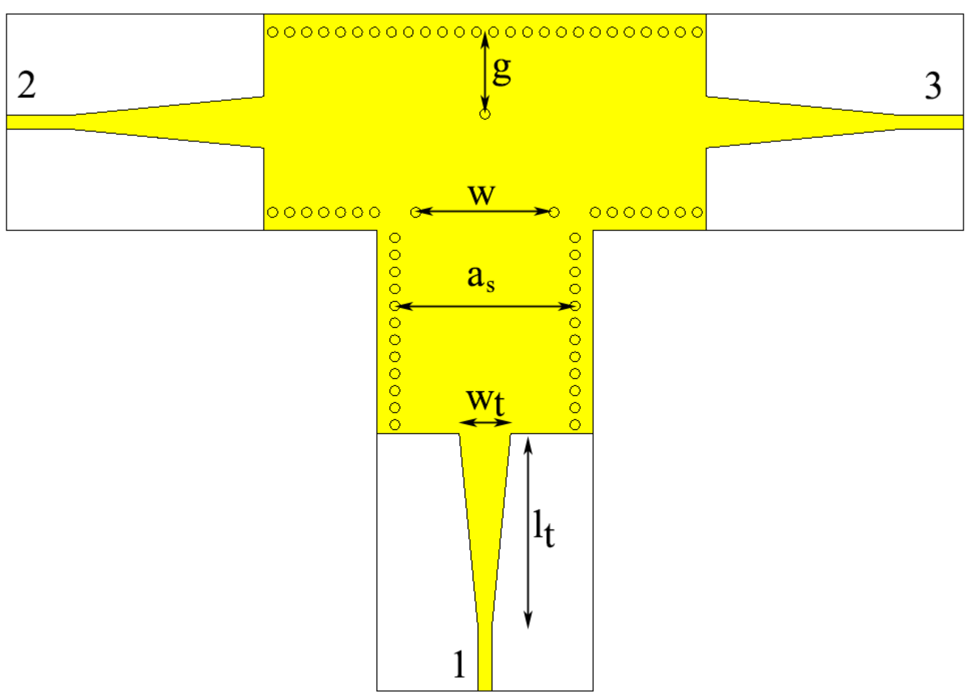

Figure 4.1: T-junction SIW power divider

Table 4.1: Dimensions of the T-junction SIW power divider

Parameter	Length (mil)	Parameter	Length (mil)
w_t	85	l_t	325
w	288	g	135
a_s	297		

S-parameter results for the simulated divider are given in Fig. 4.2. When we investigate the simulation results, S_{11} is better -12 dB in whole X-band, and S_{21} (and S_{31}) is about -3.5 dB. These results are promising, however isolation between the output arms (S_{23}) is worse than -10 dB in the whole frequency band. Therefore, isolation of this divider is not satisfactory for high isolation requiring applications.

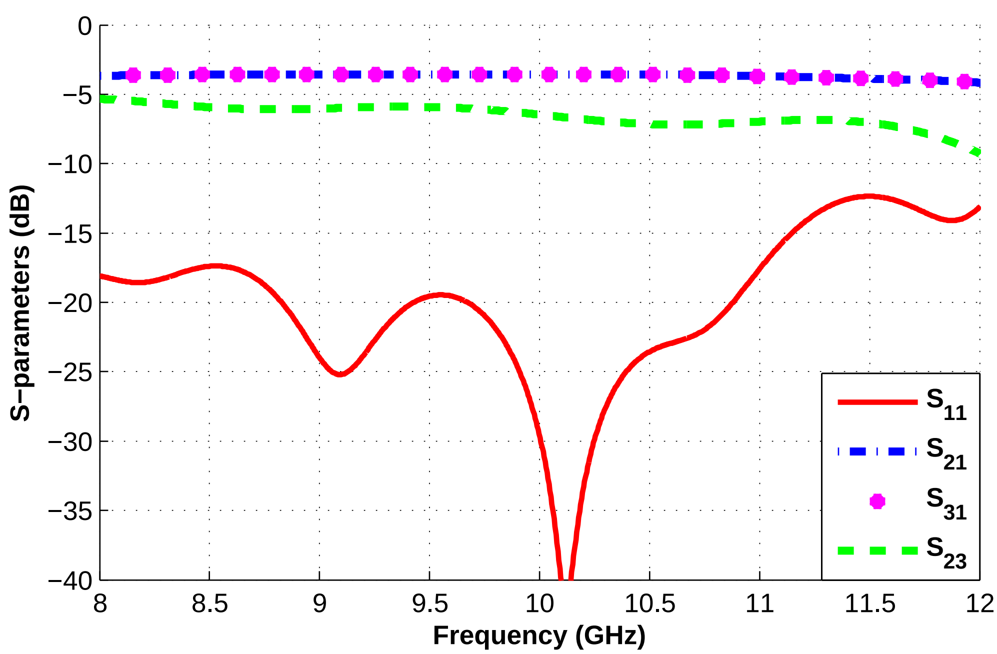

Figure 4.2: Simulation results of the T-junction SIW power divider illustrated in Fig. 4.1 with the parameters tabulated in Table 4.1

Table 4.2: Dimensions of the Y-junction SIW power divider

Parameter	Length (mil)	Parameter	Length (mil)
w_t	85	l_t	325
g	196	a_s	135

4.2 Y-junction SIW Power Divider

In Y-junction power dividers, the output arms are in the same direction and hence, the structure looks like the letter 'Y'. The input port can be thought as the lower line and the output ports are as the upper lines of the letter 'Y'. For test purposes, a Y-junction SIW power divider on Rogers TMM10i with the same aforementioned properties is designed as illustrated in Fig. 4.3, and the dimensions are given in Table 4.2. The 50Ω microstrip line width is 22 mil, via diameters are 16 mil and the separation between the adjacent vias is 28 mil. Since the design is at X-band, the proper SIW width, a_s, is found and kept the same in output arms as well. One of the critical design parameter is the location of the junction of 3 arms labelled with g as seen in Fig. 4.3. This parameter should be chosen carefully in order to meet the frequency and matching requirements. 3-D electromagnetic simulation of the design is performed with CST MWS and the simulation results are given in Fig. 4.4. S_{21} (and S_{31}) is about -3.5 dB in the whole band and S_{11} is below -10 dB between 8 - 12 GHz and better than -20 dB between 9.5 - 11 GHz. As in the T-junction design, the isolation is not better than 7 dB which is quite unsatisfactory. It should be noted that one way to solve the isolation problem in SIW based power dividers is as follows [60]: a rectangular slot whose width determined by the resistor dimensions and length determined by the number of chip resistors is introduced at the junction of the arms and necessary number of chip resistors with appropriate values are soldered on the slot. However, an iteration regarding the length of the slot may be necessary as longer slot lengths can worsen the S-parameters. Thus, an optimization of the slot length based on the response of the S-parameters may be necessary. Using this method, better than 15 dB isolation can be achieved. Consequently, this method is implemented to our novel CSIW based power divider which is explained in the next section.

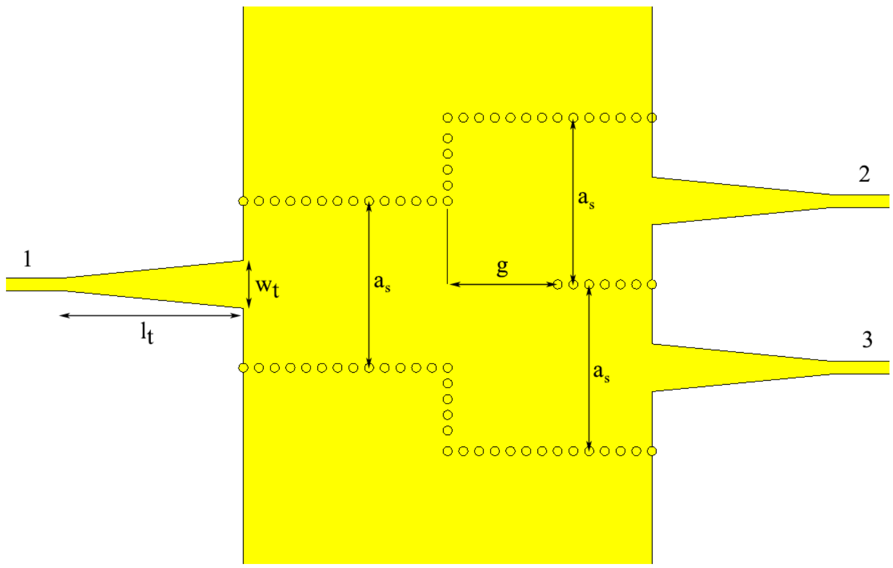

Figure 4.3: Y-junction SIW power divider

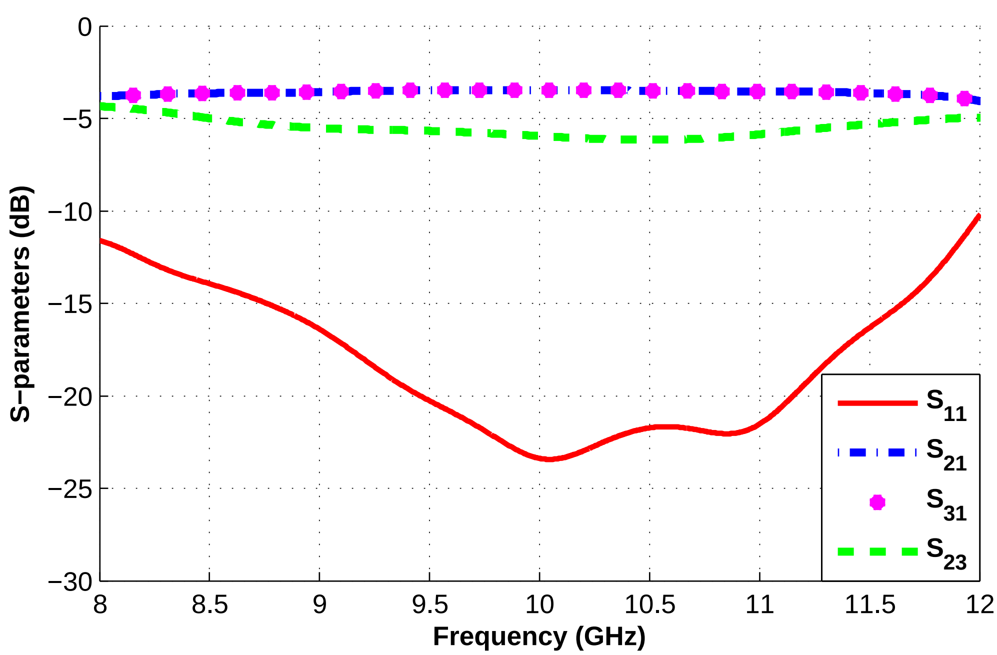

Figure 4.4: Simulation results of the Y-junction SIW power divider illustrated in Fig. 4.3 whose parameters are tabulated in Table 4.2

Table 4.3: Dimensions of the CSIW at X-band

Parameter	Length (mil)	Parameter	Length (mil)
w_t	140	l_t	190
u	16	v	12
a_s	350	l_c	210

4.3 Corrugated SIW

Corrugated Substrate Integrated Waveguide (CSIW) is a relatively new form of SIW architecture which uses open ended quarter wavelength microstrip stubs instead of metallic vias at the side walls. It shows a similar wave behaviour with that of a standard SIW structure. To investigate its characteristics, even and odd mode analysis of this structure is performed in [52], and following the proposed design steps given in [52], CSIW based devices can be built. The main advantage of CSIW is that it avoids the process of metallic via plating. Via plating can be considered to be a costly process as the process shows variation based on the substrate. Therefore, CSIW can provide simpler and cost effective fabrication.

Before the design of the CSIW based power divider, a CSIW structure having a tapered transition is designed on Rogers 4003 substrate that has a relative dielectric constant, $\epsilon_r = 3.55$, loss tangent 0.0027 and a thickness of 20 mil. The design, which is shown in Fig. 4.5, is optimized to work over the entire X-band. As shown in Fig. 4.5, the critical design parameters are the CSIW width (a_s), taper width (w_t), taper length (l_t) as well as the dimensions of the open-circuit stubs, namely the width, the length and the spacing between the open-circuit stubs labelled with u, l_c and v, respectively. Finally, the 50 Ω line width (for input and output ports) is 44 mil and the length of these lines is selected to be 200 mil (only affects the insertion loss). The CSIW structure shown in Fig. 4.5 has 20 open-circuit stubs on each side.

The CST MWS simulation results of the structure are given in Fig. 4.6 and the corresponding design parameters are given in Table 4.3. The structure yields an S_{11} value better than -20 dB whereas the S_{21} is better than -1 dB between 9.2 and 11.7 GHz.

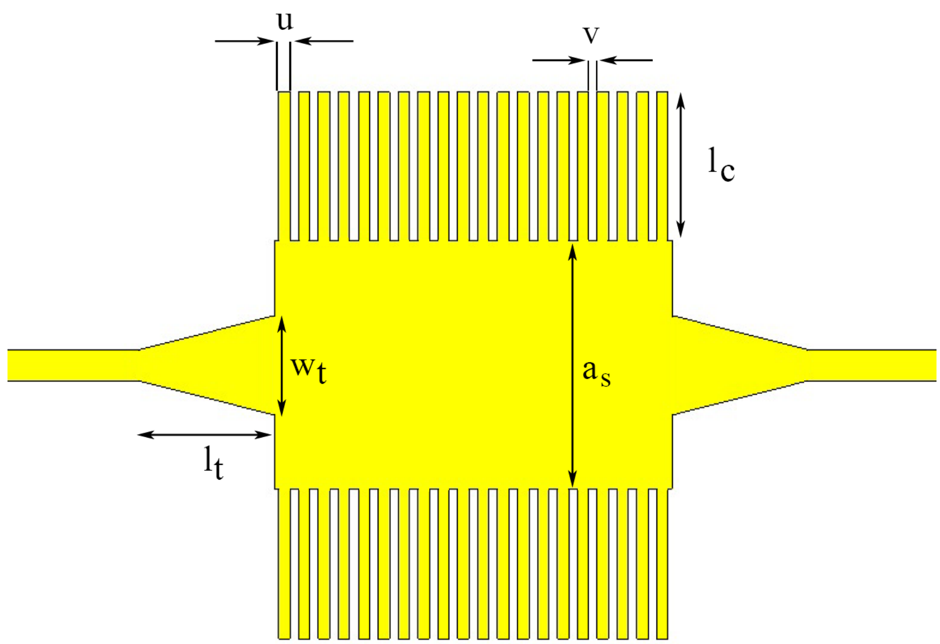

Figure 4.5: CST view of CSIW with microstrip transition

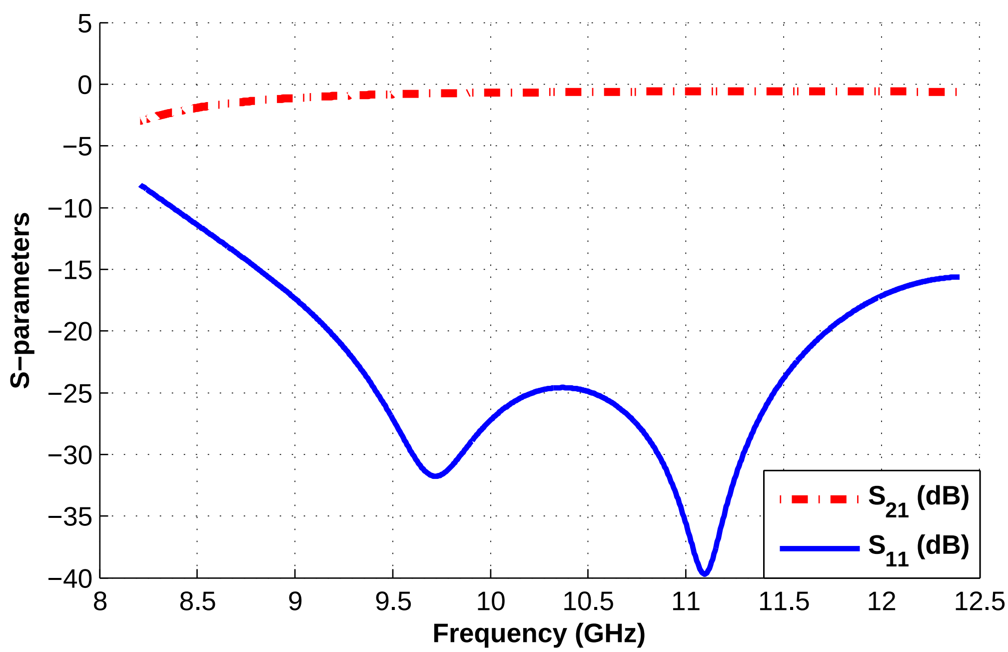

Figure 4.6: S-parameter simulation results of microstrip to CSIW transition at X-band for the design shown in Fig. 4.5 with the parameters tabulated in Table 4.3

4.4 Novel CSIW Based Power Divider

SIW based devices are more compact and have lighter weight compared to waveguide structures. However, they are still larger and more bulky than microstrip based devices. Therefore to reduce the size of the SIW based power divider, the output arms can be directly connected to microstrip lines [56]. As a result, the final architecture can be viewed more like a hybrid combination of SIW and microstrip structures (rather than a pure SIW architecture).

Considering this fact in mind, a SIW based power divider at X-band, proposed in [56], is realized with CSIW where the metallic vias are replaced with open-circuit stubs as explained before. The output arms are realized with microstrip lines providing smaller size. The design is shown in Fig. 4.7.

As the first design step, the initial values of the critical parameters for a CSIW structure at X-band are determined. This step is accomplished by synthesizing the structure as a SIW and then converting to CSIW by determining the length and width of the open-circuit stubs. Additionally, the width of the CSIW and the microstrip taper parameters are also optimized for the desired matching at the operating frequency band. Once the CSIW and the microstrip transition related parameters are determined, as the second step, the single output arm of the CSIW structure is doubled and the separation between the output arms (shown by s in Fig. 4.7) as well as the associated microstrip transition related parameters (w_t and l_t) are re-optimized for input matching at the operating frequency band. Then, the third step is to introduce a slot at the junction of the output arms whose width (w_g in Fig. 4.7) and length (l_g in Fig. 4.7) are optimized in order not to affect the matching as well as the transmission. Note that the width (w_g) must be narrow enough so that chip resistors can be soldered across the slot and the length should be sufficiently long to accommodate necessary number of chip resistors. These resistors do not affect the input return loss and more importantly (together with the introduced slot) the isolation between the output arms are significantly improved.

Following the aforementioned design steps, a prototype CSIW power divider, shown in Fig. 4.7, is designed on Rogers 4003 substrate that has a relative dielectric constant $\epsilon_r = 3.55$, loss tangent = 0.0027 and a thickness of 20 mil. Final design parameters are tabulated in Table 4.4 and additionally the width of the 50 Ω microstrip line is 44 mil. The fabricated prototype is illustrated in Fig. 4.8 where the Southwest Microwave's end-launch connectors are used for measurement. Resistor values are carefully chosen as they affect the output return loss and the isolation of the divider as discussed before. In this prototype two resistors are found to be sufficient for the desired bandwidth and isolation. The value of the resistor closer to the input arm is 80 Ω and the value of the resistor closer to the output arms is 95 Ω.

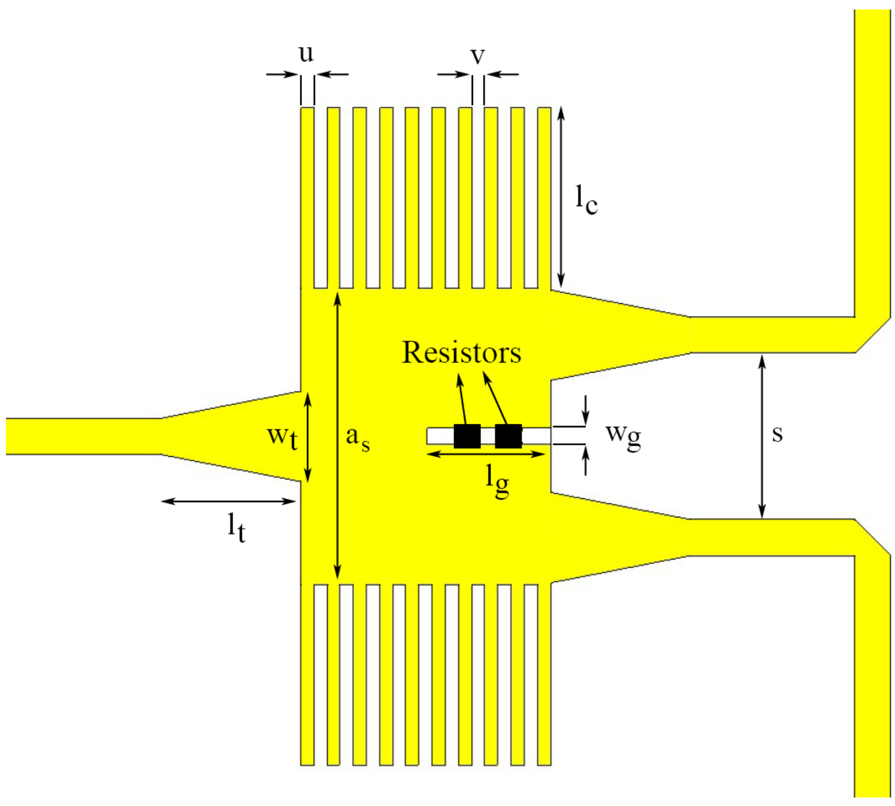

Figure 4.7: CST model of the CSIW power divider

Simulated and measured S-parameter results are given in Figs. 4.9 to 4.15. In Figs. 4.9 and 4.10, S_{11} and S_{21} (and S_{31}) are investigated, respectively and they are as expected in the simulations. S_{11} is better than -12 dB and S_{21} (and S_{31}) is about -4.2 dB in whole X-Band. In Fig. 4.11, the measured isolation is also similar to simulation results. In measurement, it is almost better than 10 dB in

Table 4.4: Dimensions of the CSIW divider at X-band

Parameter	Length (mil)	Parameter	Length (mil)
w_t	110	l_t	170
u	16	v	16
w_g	20	l_g	150
a_s	360	l_c	220
s	202		

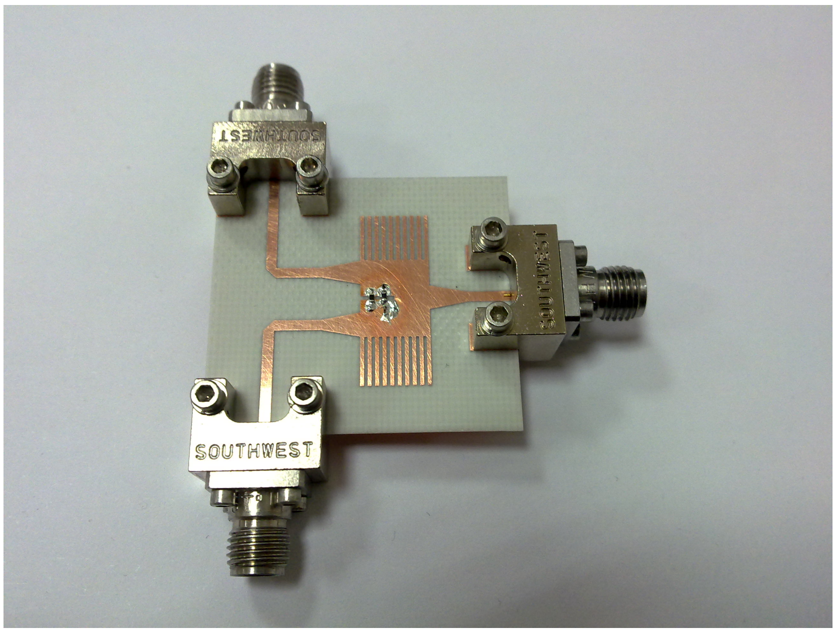

Figure 4.8: Fabricated CSIW power divider

whole band and maximum 20 dB at around 11 GHz.

When we investigate the effects of the resistors on isolation, measurement results seen in Fig. 4.12 demonstrate the positive effects of the resistors on isolation. Up to 10 dB isolation improvement is achieved in some frequencies. In Fig. 4.13, the effects of the resistors on S_{21} and S_{11} are investigated and it is clear that the resistors have almost no effect on them. Output return losses (S_{22} and S_{33}) are reduced when the resistors are used as shown in Fig. 4.14. An improvement up to 7 dB is obtained after the introduction of the proper resistors. Finally, the measured phases of S_{21} and S_{31} are investigated in Fig. 4.15. There is no phase difference between the output arms as expected.

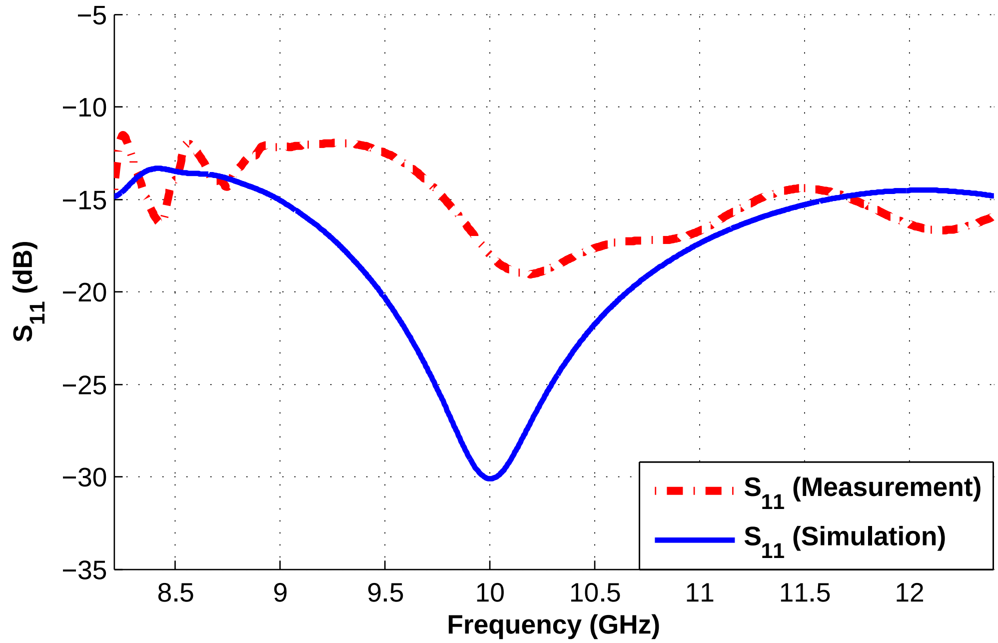

Figure 4.9: S_{11} versus frequency results of the divider shown in Fig. 4.8 with the parameters tabulated in Table 4.4

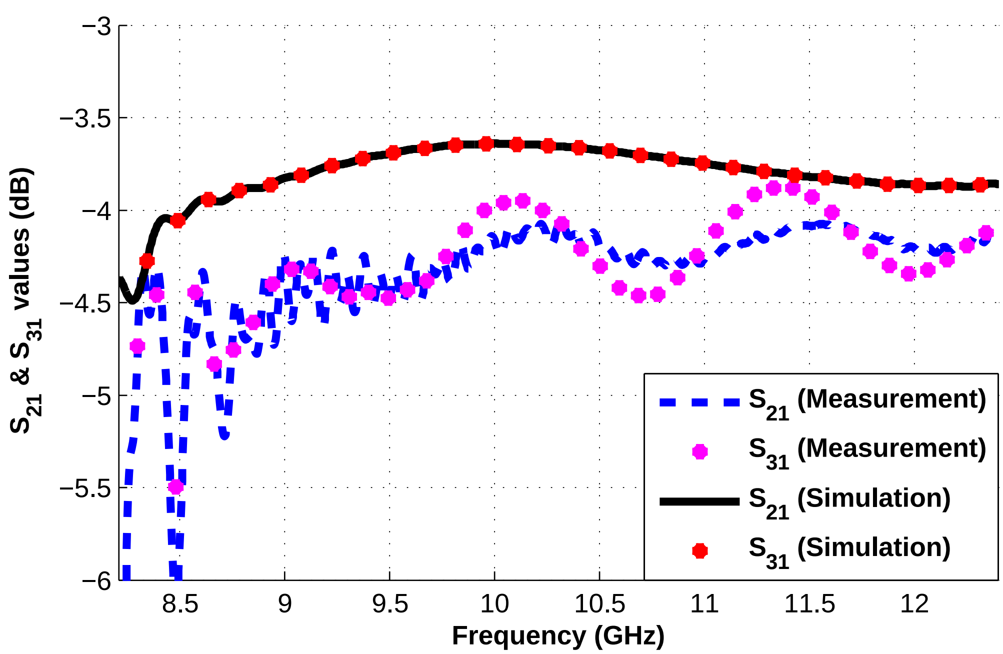

Figure 4.10: S_{21} and S_{31} versus frequency results of the divider shown in Fig. 4.8 with the parameters tabulated in Table 4.4

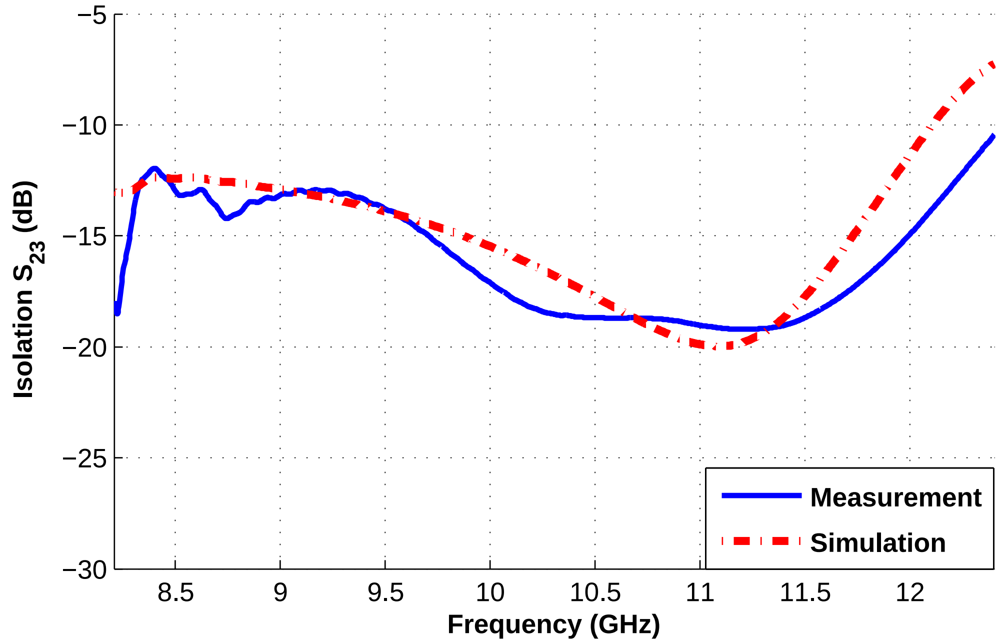

Figure 4.11: Isolation of the divider (resistors are present) shown in Fig. 4.8 with the parameters tabulated in Table 4.4

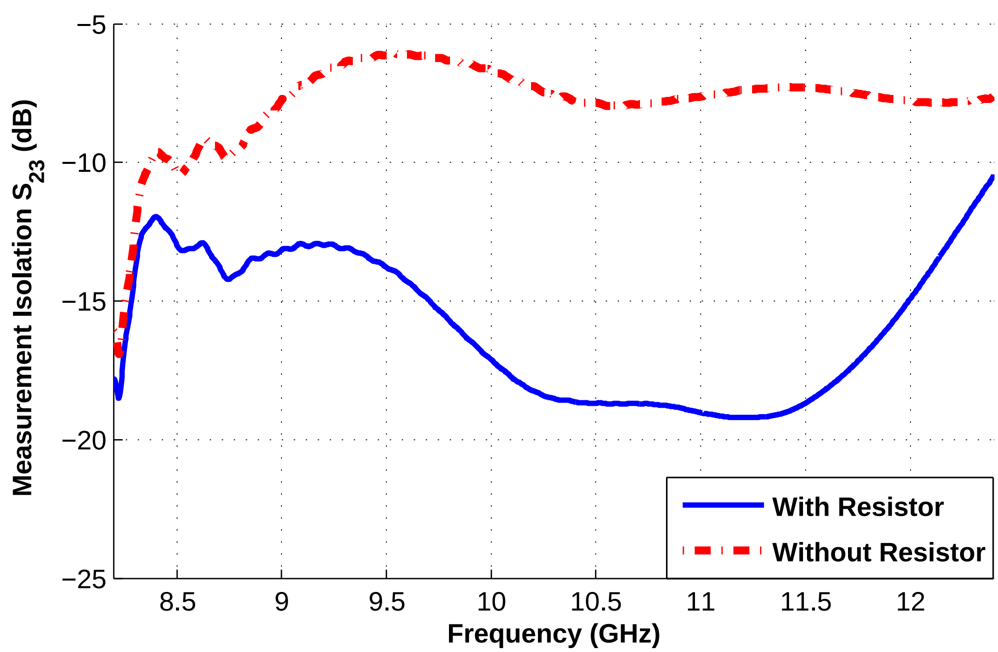

Figure 4.12: Isolation of the divider with and without the resistors (divider is shown in Fig. 4.8 with the parameters tabulated in Table 4.4)

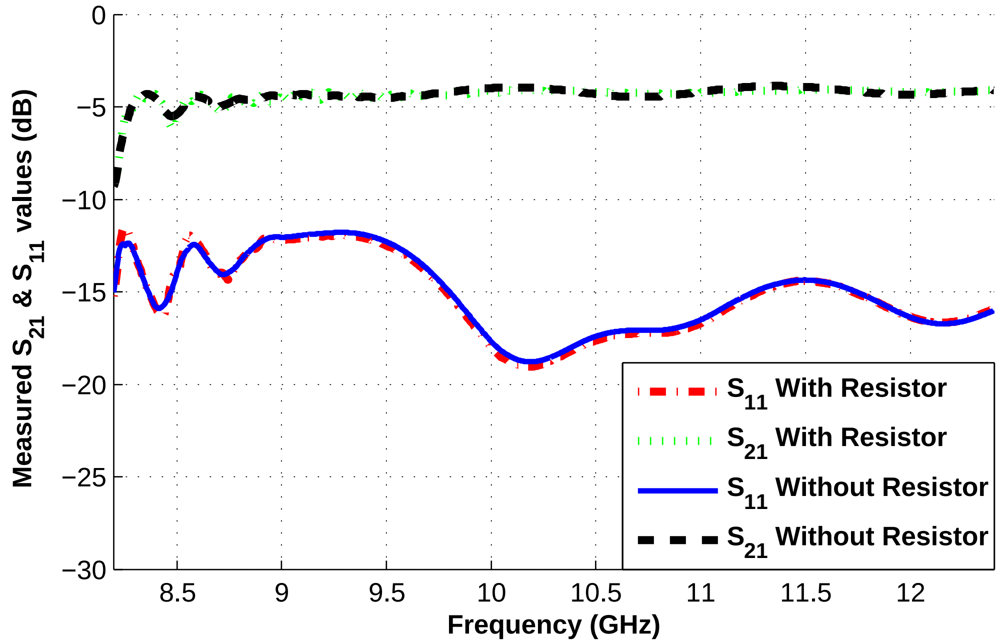

Figure 4.13: Effects of the resistors on S_{11} and S_{21} for the divider shown in Fig. 4.8 with the parameters tabulated in Table 4.4

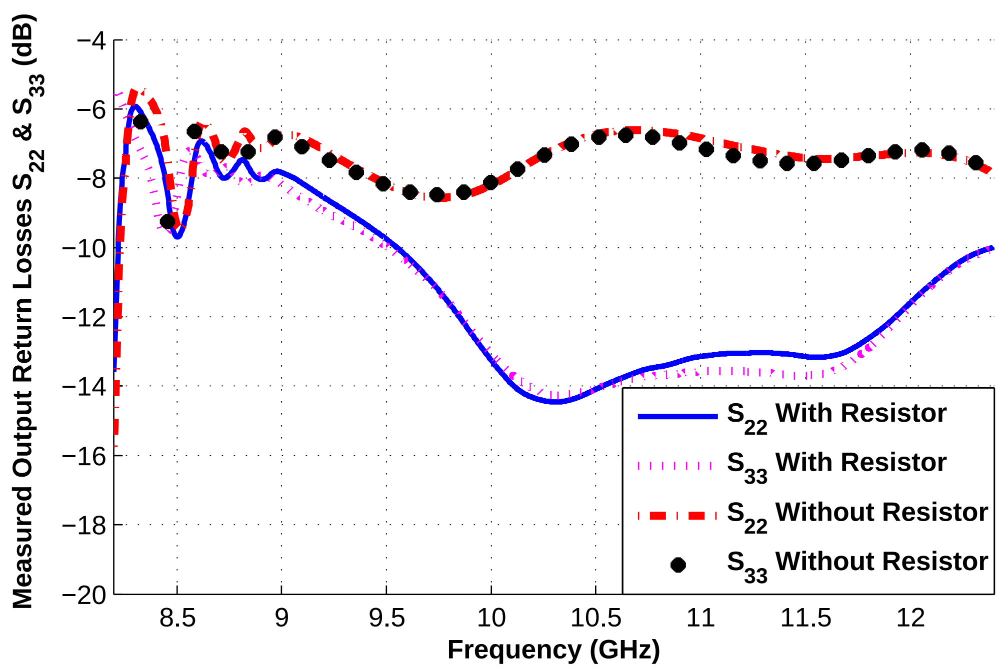

Figure 4.14: Effects of the resistor on the output return losses for the divider shown in Fig. 4.8 with the parameters tabulated in Table 4.4

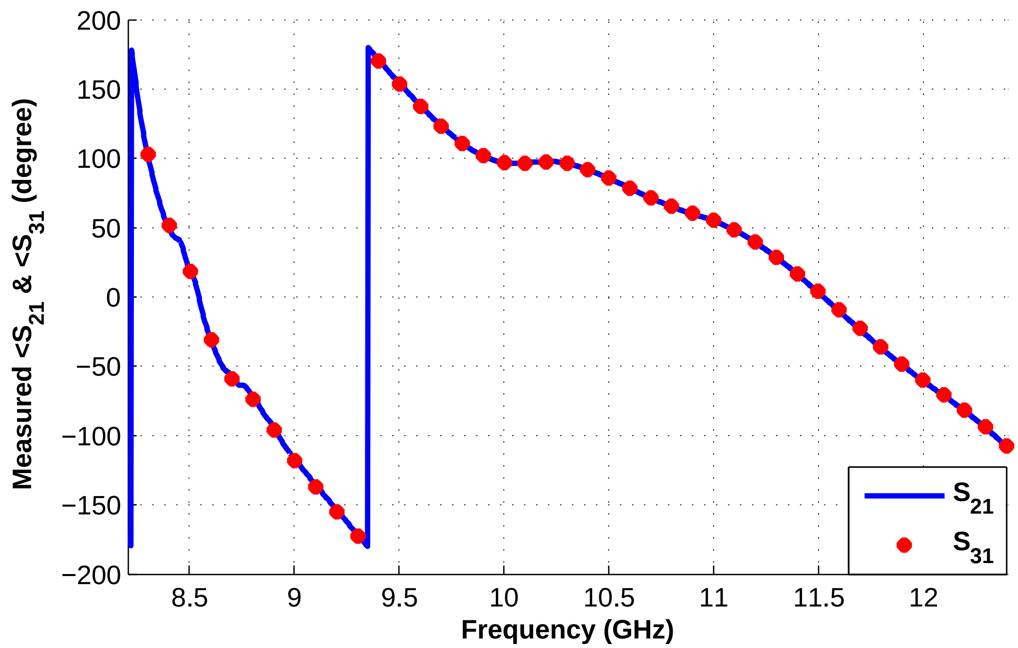

Figure 4.15: Phases of S_{21} and S_{31} for the divider shown in Fig. 4.8 with the parameters tabulated in Table 4.4

Chapter 5

Conclusion

In this thesis, a popular guiding structure of last decades named substrate integrated waveguide (SIW) and its applications with passive microwave devices have been deeply studied; novel filter and power divider structures have been proposed. Due to its low cost, easy integration with printed devices, light weight and compact size, it attracts the attention of many researchers and it is widely used in modern radar and communication applications.

In Chapter 2, design parameters of SIW and its transition to other guiding structures have been investigated by using 3-D electromagnetic simulation software CST MWS. Having designed a SIW for the desired frequency band, transition to other guiding structures are investigated. SIW to microstrip, grounded coplanar waveguide (GCPW) and waveguide transitions suggested in the literature are studied and analyzed for desired frequency bands and the simulation results agree well with the results available in the literature. They work well with good matching and low loss. Other work done in this chapter is that SIW and microstrip line with the same total length are manufactured on the same substrate in order to compare their insertion loss and return loss performances at Ka-band. Although SIW insertion loss is slightly higher than microstrip's loss, fabrication tolerances of SIW at high frequencies may make it more preferable.

In Chapter 3, SIW based microwave bandpass filter structures have been investigated. Waveguide iris bandpass filter structure is designed with SIW technology and fabricated at X- and K-bands. Measurement and simulation results agree well with each other in terms of insertion and return losses. Then, using CSRR and dumbbell type DGS, SIW based bandpass filters that are available in the literature are investigated and similar results with the ones reported in the literature are obtained. Having investigated these filter structures in the literature, a novel SIW bandpass filter topology is proposed by replacing the resonators in reverse geometry which is called interdigital configuration. This filter is designed at X band, and in order to suppress its harmonic band dumbbell type defected ground structure is designed at the bottom ground side of the filter underneath the microstrip feeding lines. Simulation and fabrication results agree well with each other and it shows that this filter can be successfully used in microwave applications due to its good harmonic suppression performance.

In Chapter 4, SIW based microwave power dividers are the main focus. Suggested topologies with Y and T-junctions available in the literature are redesigned for X band. They are investigated via simulations and their performances are found to be sufficient enough so that they can be used in microwave applications. In this chapter, a novel SIW architecture called Corrugated SIW (CSIW) is investigated. CSIW offers the wave propagation performance similar to SIW, and it has the advantage of easy fabrication since it uses open stub microstrip lines with quarter wavelength instead of metallic vias. It does not require the chemical processes that is used to plate the vias with conductor. Therefore, it speeds up the fabrication time and reduces the cost. By combining CSIW structure with the power divider topologies presented in the literature, a novel CSIW power divider with high isolation is designed and fabricated. Measurement results show that it has low loss, good input/output matching and by using chip resistors it provides high isolation performance between the output arms. This device is suitable for high frequency applications with its appropriate S-parameter responses.

This thesis shows that SIW based devices work as well as microstrip and waveguide based ones. SIW shows fairly better high frequency response than microstrip in terms of radiation loss and fabrication tolerances; and its low cost, easy fabrication process and light weight makes it more advantageous than waveguide structures. However, a higher insertion loss is observed (compared to microstrip line based structures) even at relatively high frequencies. This can be attributed to the leakage of power between the vias. By using the topologies suggested in this study, SIW based filters with well harmonic band responses and power dividers with high isolation can be designed for desired frequencies. In future work, CSIW based filter topologies and wide bandwidth power dividers with high isolation can be made.

Bibliography

[1] D. M. Pozar, *Microwave Engineering, 3rd Edition.* Wiley, 2005.

[2] R. E. Collin, *Foundations for Microwave Engineering, 1st Edition.* McGraw Hill, 1992.

[3] M. Bozzi, A. Georgiadis, and K. Wu, "Review of substrate-integrated waveguide circuits and antennas," *IET Microw. Antennas Propag.*, vol. 5, no. 8, pp. 909–920, 2011.

[4] J. E. Rayas-Sanchez, "An improved em-based design procedure for single-layer substrate integrated waveguide interconnects with microstrip transitions," *IEEE MTT-S Int. Microwave Workshop Series on Signal Integrity and High Speed Interconnects*, February 2008.

[5] K. Wu, D. Deslandes, and Y. Cassivi, "The substrate integrated circuits-a new concept for high-frequency electronics and optoelectronics," *TELSKIS 2003, Nis, Serbia and Montenegro*, October 2003.

[6] B. H. Ahmad and I. C. Hunter, "Design and fabrication of a substrate integrated waveguide bandstop filter," *European Microwave Conference, Amsterdam*, October 2008.

[7] G. H. Zhai, W. Hong, K. Wu, J. X. Chen, P. Chen, J. Wei, and H. J. Tang, "Folded half mode substrate integrated waveguide 3 db coupler," *IEEE Microwave and Wireless Components Letters*, vol. 18, no. 8, pp. 512–514, August 2008.

[8] S. A. Winkler, W. Hong, M. Bozzi, and K. Wu, "Polarization rotating frequency selective surface based on substrate integrated waveguide technology," *IEEE Transactions on Antennas and Propagation*, vol. 58, no. 4, pp. 1202–1213, April 2010.

[9] S. Cheng, H. Yousef, and H. Kratz, "79 ghz slot antennas based on substrate integrated waveguides (siw) in a flexible printed circuit board," *IEEE Transactions on Antennas and Propagation*, vol. 57, no. 1, pp. 64–71, January 2009.

[10] W. D'Orazio, K. Wu, and J. Helszajn, "A substrate integrated waveguide degree-2 circulator," *IEEE Microwave and Wireless Components Letters*, vol. 14, no. 5, pp. 207–209, May 2004.

[11] D. Deslandes, "Design equations for tapered microstrip-to-substrate integrated waveguide transitions," *IEEE International Microwave Symposium*, May 2010.

[12] M. Abdolhamidi, A. Enayati, M. Shahabadi, and R. Faraji-Dana, "Wideband single-layer dc-decoupled substrate integrated waveguide (siw) - to - microstrip transition using an interdigital configuration," *Asia Pacific Microwave Conference*, 2007.

[13] X.-P. Chen and K. Wu, "Low-loss ultra-wideband transition between conductor-backed coplanar waveguide and substrate integrated waveguide," *IEEE International Microwave Symposium*, 2009.

[14] T. Kai, J. Hirolawa, and M. Ando, "Feed through an aperture to a post-wall waveguide with step structure," *IEICE Trans. Commun.*, vol. E88-B, no. 3, pp. 1298–1302, March 2005.

[15] L. Xia, R. Xu, B. Yan, J. Li, Y. Guo, and J. Wang, "Broadband transition between air-filled waveguide and substrate integrated waveguide," *Electronics Letters*, vol. 42, no. 24, November 2006.

[16] L. Li, X. Chen, R. Khazaka, and K. Wu, "A transition from substrate integrated waveguide (siw) to rectangular waveguide," *Asia Pacific Microwave Conference*, pp. 2605–2608, 2009.

[17] J. E. Rayas-Sanchez and V. Gutierrez-Ayala, "A general em-based design procedure for single-layer substrate integrated waveguide interconnects with microstrip transitions," *IEEE MTT-S Int. Microwave Symp. Dig., Atlanta, GA*, pp. 983–986, June 2008.

[18] J. D. Martinez, S. Sirci, and V. E. Boria, "Compact cpw-fed combline filter in substrate integrated waveguide technology," *IEEE Microwave and Wireless Components Letters*, vol. 22, no. 1, pp. 7–9, January 2012.

[19] J. Chen, B. Wu, L.-w. Jiang, and C.-h. Liang, "A compact hexagonal dual-band substrate integrated waveguide filter based on extracted-pole technique," *Microwave Opt Technol Lett*, vol. 53, pp. 562–565, 2011.

[20] Y. Zhai, Q. Wang, Z. Wang, and X. X. Gao, "The design of an iris waveguide filter at 35.75 ghz," *Global Symposium on Millimeter Waves Proc.*, pp. 348–350, 2008.

[21] T.-S. Yun, H. Nam, K.-B. Kim, and J.-C. Lee, "Iris waveguide bandpass filter using substrate integrated waveguide (siw) for satellite communication," *APMC 2005 Proceedings*, 2005.

[22] X.-P. Chen, L. Han, and K. Wu, "Synthesis and design of substrate integrated waveguide filter using predistortion technique," *Asia Pacific Microwave Conference*, 2007.

[23] X.-P. Chen and K. Wu, "Accurate and efficient design approach of substrate integrated waveguide filter using numerical trl calibration technique," *IEEE Conference*, pp. 1231–1234, 2008.

[24] X.-P. Chen and K. Wu, "Substrate integrated waveguide cross-coupled filter with negative coupling structure," *IEEE Transactions on Microwave Theory and Techniques*, vol. 56, no. 1, pp. 142–149, January 2008.

[25] P. Qiu, Y. Zhang, and B. Yan, "A novel millimeter-wave substrate integrated waveguide (siw) filter buried in ltcc," *Asia Pacific Microwave Conference*, pp. 1–4, 2008.

[26] B. Potelon, J.-F. Favennec, C. Quendo, E. Rius, C. Person, and J.-C. Bohorquez, "Design of a substrate integrated waveguide (siw) filter using a novel topology of coupling," *IEEE Microwave and Wireless Components Letters*, vol. 18, no. 9, pp. 596–598, September 2008.

[27] J. Bornemann and F. Taringou, "Substrate-integrated waveguide filter design using mode-matching techniques," *41st European Microwave Conference, UK*, pp. 1–4, October 2011.

[28] Z. Kordiboroujeni, F. Taringou, and J. Bornemann, "Efficient mode-matching design of substrate- integrated waveguide filters," *Proceedings of the 42nd European Microwave Conference, Netherlands*, pp. 253–256, October 2012.

[29] S. S. Sabri, B. H. Ahmad, and A. R. B. Othman, "A review of substrate integrated waveguide (siw) bandpass filter based on different method and design," *Asia Pacific Microwave Conference on Applied Electromagnetics, Malaysia*, pp. 210–215, December 2012.

[30] X. Chen, W. Hong, T. Cui, J. Chen, and K. Wu, "Substrate integrated waveguide (siw) linear phase filter," *IEEE Microwave and Wireless Components Letters*, vol. 15, no. 11, pp. 556–558, November 2005.

[31] X.-P. Chen, K. Wu, and Z.-L. Li, "Dual-band and triple-band substrate integrated waveguide filters with chebyshev and quasi-elliptic responses," *IEEE Transactions on Microwave Theory and Techniques*, vol. 55, no. 12, pp. 2569–2578, December 2007.

[32] Z.-C. Hao, W. Hong, X.-P. Chen, J.-X. Chen, and K. Wu, "A single-layer folded substrate integrated waveguide (siw) filter," *Asia Pacific Microwave Conference*, 2008.

[33] R. Li, X. Tang, and F. Xiao, "Design of substrate integrated waveguide transversal filter with high selectivity," *IEEE Microwave and Wireless Components Letters*, vol. 20, no. 6, pp. 328–330, June 2010.

[34] L. Szydlowski, A. Lamecki, and M. Mrozowski, "Design of microwave lossy filter based on substrate integrated waveguide (siw)," *IEEE Microwave and Wireless Components Letters*, vol. 21, no. 5, pp. 249–251, May 2011.

[35] L. Szydlowski, N. Leszczynska, A. Lamecki, and M. Mrozowski, "A substrate integrated waveguide (siw) bandpass filter in a box configuration with frequency-dependent coupling," *IEEE Microwave and Wireless Components Letters*, vol. 22, no. 11, pp. 556–558, November 2012.

[36] F. Zhu, W. Hong, J.-X. Chen, and K. Wu, "Cross-coupled substrate integrated waveguide filters with improved stopband performance," *IEEE Microwave and Wireless Components Letters*, vol. 22, no. 12, pp. 633–635, December 2012.

[37] X.-C. Zhang, Z.-Y. Yu, and J. Xu, "Novel band-pass substrate integrated waveguide (siw) filter based on complementary split ring resonators (csrrs)," *Progress In Electromagnetics Research*, vol. 72, pp. 39–46, 2007.

[38] Y. D. Dong, T. Yang, and T. Itoh, "Substrate integrated waveguide loaded by complementary split-ring resonators and its applications to miniaturized waveguide filters," *IEEE Transactions on Microwave Theory and Techniques*, vol. 57, no. 9, pp. 2211–2223, September 2009.

[39] Q.-L. Zhang, W.-Y. Yin, S. He, and L.-S. Wu, "Compact substrate integrated waveguide (siw) bandpass filter with complementary split-ring resonators (csrrs)," *IEEE Microwave and Wireless Components Letters*, vol. 20, no. 8, pp. 426–428, August 2010.

[40] Y. Dong and T. Itoh, "Substrate integrated waveguide loaded by complementary split-ring resonators for miniaturized diplexer design," *IEEE Microwave and Wireless Components Letters*, vol. 21, no. 2, pp. 10–12, January 2011.

[41] K. Deng, Z. Guo, L. Chao, and W. Che, "A compact planar bandpass filter with wide out-of-band rejection implemented by substrate integrated waveguide and complementary split-ring resonator," *Microwave Opt Technol Lett.*, vol. 53, pp. 1483–1487, 2011.

[42] Q.-L. Zhang, W.-Y. Yin, S. He, and L.-S. Wu, "Evanescent-mode substrate integrated wa- veguide (siw) filters implemented with com- plementary split ring resonators," *Progress In Electromagnetics Research*, vol. 111, pp. 419–432, 2011.

[43] L. Qiang, H.-M. Lu, W. Zhao, H.-B. Qin, and B. Liu, "Half mode substrate integrated waveguide miniaturization using complementary split ring resonators," *Microwave Opt Technol Lett.*, vol. 53, no. 5, pp. 1074–1077, May 2011.

[44] L. Zhou, S. Liu, N. Gao, Y. Chen, and Y. Wei, "Miniaturized substrate integrated waveguide filter with complementary spiral resonator," *Microwave Opt Technol Lett.*, vol. 53, no. 6, pp. 1308–1311, June 2011.

[45] W.-Y. Park and S. Lim, "Miniaturized substrate integrated waveguide (siw) bandpass filter loaded with double-sided- complementary split ring resonators (ds-csrrs)," *Proc.s of the 41st European Microwave Conference, UK*, pp. 740–743, October 2011.

[46] W. Jiang, W. Shen, L. Zhou, and W.-Y. Yin, "Miniaturized and high-selectivity substrate integrated waveguide (siw) bandpass filter loaded by complementary split-ring resonators (csrrs)," *Journal of Electromagnetic Waves and Applications*, vol. 26, no. 11–12, pp. 1448–1459, August 2012.

[47] W. Jiang, W. Shen, L. Zhou, and W.-Y. Yin, "Miniaturised multi-band substrate integrated waveguide filters using complementary split-ring resonators," *IET Microwaves, Antennas Propagation*, vol. 6, no. 6, pp. 611–620, 2012.

[48] Z.-C. Hao, W. Hong, J.-X. Chen, X.-P. Chen, and K. Wu, "Compact super-wide bandpass substrate integrated waveguide (siw) filters," *IEEE Transactions on Microwave Theory and Techniques*, vol. 53, no. 9, pp. 2968–2977, September 2005.

[49] Y. L. Zhang, W. Hong, K. Wu, J. X. Chen, and H. J. Tang, "Novel substrate integrated waveguide cavity filter with defected ground structure," *IEEE*

Transactions on Microwave Theory and Techniques, vol. 53, no. 4, pp. 1280–1287, April 2005.

[50] W. Shen, W.-Y. Yin, and X.-W. Sun, "Compact substrate integrated waveguide (siw) filter with defected ground structure," *IEEE Microwave and Wireless Components Letters*, vol. 21, no. 2, pp. 83–85, February 2011.

[51] Y. Huang, Z. Shao, and L. Liu, "A substrate integrated waveguide bandpass filter using novel defected ground structure shape," *Progress In Electromagnetics Research*, vol. 135, pp. 201–213, 2013.

[52] K. W. Eccleston, "Mode analysis of the corrugated substrate integrated waveguide," *IEEE Transactions on Microwave Theory and Techniques*, vol. 60, no. 10, pp. 3004–3012, October 2012.

[53] D. G. Chen and K. W. Eccleston, "Substrate integrated waveguide with corrugated wall," *Asia Pacific Microwave Conference*, pp. 1–4, 2012.

[54] X. Xu, R. G. Bosisio, and K. Wu, "A new six-port junction based on substrate integrated waveguide technology," *IEEE Transactions on Microwave Theory and Techniques*, vol. 53, no. 7, pp. 2267–2273, July 2005.

[55] K. Song, Y. Fan, and Y. Zhang, "Eight-way substrate integrated waveguide power divider with low insertion loss," *IEEE Transactions on Microwave Theory and Techniques*, vol. 56, no. 6, pp. 1473–1477, June 2008.

[56] N. A. Smith and R. Abhari, "Compact substrate integrated waveguide wilkinson power dividers," *Antennas and Propagation Society International Symposium*, pp. 1–4, 2009.

[57] D.-S. Eom, J. Byun, and H.-Y. Lee, "Multilayer substrate integrated waveguide four-way out-of-phase power divider," *IEEE Transactions on Microwave Theory and Techniques*, vol. 57, no. 12, pp. 3469–3476, December 2009.

[58] K. Kim, J. Byun, and H.-Y. Lee, "Substrate integrated waveguide wilkinson power divider with improved isolation per- formance," *Progress In Electromagnetics Research*, vol. 19, pp. 41–48, 2010.

[59] W. Feng, W. Che, and K. Deng, "Compact planar magic-t using e-plane substrate integrated waveguide (siw) power divider and slotline transition," *IEEE Microwave and Wireless Components Letters*, vol. 20, no. 6, pp. 331–333, June 2010.

[60] K. Sarhadi and M. Shahabadi, "Wideband substrate integrated waveguide power splitter with high isolation," *IET Microw. Antennas Propag.*, vol. 4, no. 7, pp. 817–821, 2010.

[61] Y.-P. Hong, Y.-J. An, and J.-G. Yook, "Differential radial power combiner using substrate integrated waveguide," *Electronics Letters*, vol. 46, no. 24, November 2010.

[62] X. Zou, C.-M. Tong, and D.-W. Yu, "Y-junction power divider based on substrate integrated waveguide," *Electronics Letters*, vol. 47, no. 25, December 2011.

[63] L.-S. Wu, B. Xia, J. Mao, and W.-Y. Yin, "A half-mode substrate integrated waveguide ring for two-way power division of balanced circuit," *IEEE Microwave and Wireless Components Letters*, vol. 22, no. 7, pp. 333–335, July 2012.

[64] F. Zhu, W. Hong, J.-X. Chen, and K. Wu, "Design and implementation of a broadband substrate integrated waveguide magic-t," *IEEE Microwave and Wireless Components Letters*, vol. 22, no. 12, pp. 630–632, December 2012.

[65] R. Kazemi, R. A. Sadeghzadeh, and A. E. Fathy, "Design of a wide band eight-way compact siw power combiner fed by a low loss gcpw- to-siw transition," *Progress In Electromagnetics Research*, vol. 26, pp. 97–110, 2012.

[66] F. Falcone, T. Lopetegi, J. D. Baena, R. Marques, F. Martn, and M. Sorolla, "Effective negative-epsilon stopband microstrip lines based on complementary split ring resonators," *IEEE Microwave and Wireless Components Letters*, vol. 14, no. 6, pp. 280–282, June 2004.

[67] G. L. Matthaei, L. Young, and M. Jones, *Microwave Filters, Impedance-Matching Networks and Coupling Structures*. McGraw-Hill, 1964.

Appendix A

Frequency Bands

Table A.1: Frequency bands with corresponding waveguide standards

Frequency Band	Waveguide Standard	Frequency (GHz)	Dimensions (mil)
R	WR-430	1.7 - 2.6	4300 x 2150
D	WR-340	2.2 - 3.3	3400 x 1700
S	WR-284	2.6 - 3.95	2840 x 1340
E	WR-229	3.3 - 4.9	2290 x 1150
G	WR-187	3.95 - 5.85	1872 x 872
F	WR-159	4.9 - 7.05	1590 x 795
C	WR-137	5.85 - 8.2	1372 x 622
H	WR-112	7.05 - 10	1122 x 497
X	WR-90	8.2 - 12.4	900 x 400
Ku	WR-62	12.4 - 18	622 x 311
K	WR-51	15 - 22	510 x 255
K	WR-42	18 - 26.5	420 x 170
Ka	WR-28	26.5 - 40	280 x 140
Ku	WR-22	33 - 50	224 x 112

Appendix B

Datasheets

ROGERS CORPORATION
Advanced Circuit Materials

Advanced Circuit Materials Division
100 S. Roosevelt Avenue
Chandler, AZ 85226
Tel: 480-961-1382, Fax: 480-961-4533
www.rogerscorporation.com

Data Sheet
1.3000

RO3000® Series High Frequency Circuit Materials

Features and Benefits:

- Low dielectric loss for high frequency performance (RO3003). Laminate can be used in applications up to 30-40 GHz.
- Excellent mechanical properties versus temperature for reliable stripline and multilayer board constructions.
- Uniform mechanical properties for a range of dielectric constants. Ideal for multilayer board designs with a range of dielectric constants. Suitable for use with epoxy glass multilayer board hybrid designs.
- Stable dielectric constant versus temperature and frequency for RO3003. Ideal for band pass filters, microstrip patch antennas, and voltage controlled oscillators.
- Low in-plane expansion coefficient (matched to copper). Allows for more reliable surface mounted assemblies. Ideal for applications sensitive to temperature change and excellent dimensional stability.
- Volume manufacturing process for economical laminate pricing.

Typical Applications:

- Automotive Collision Avoidance Systems
- Automotive Global Positioning Satellite Antennas
- Cellular and Pager Telecommunications Systems
- Patch Antennas for Wireless Communications
- Direct Broadcast Satellites
- Datalink on Cable Systems
- Remote Meter Readers
- Power Backplanes

RO3000® High Frequency Circuit Materials are ceramic- filled PTFE composites intended for use in commercial microwave and RF applications. This family of products was designed to offer exceptional electrical and mechanical stability at competitive prices.

RO3000® series laminates are PTFE-based circuit materials with mechanical properties that are consistant regardless of the dielectric constant selected. This allows the designer to develop multilayer board designs that use different dielectric constant materials for individual layers, without encountering warpage or reliability problems.

The dielectric constant versus temperature of RO3000 series materials is very stable (Charts 1 and 2). These materials exhibit a coefficient of thermal expansion (CTE) in the X and Y axis of 17 ppm/°C. This expansion coefficient is matched to that of copper, which allows the material to exhibit excellent dimensional stability, with typical etch shrinkage (after etch and bake) of less than 0.5 mils per inch. The Z-axis CTE is 24 ppm/ C, which provides exceptional plated through-hole reliability, even in severe thermal environments.

RO3000® series laminates can be fabricated into printed circuit boards using standard PTFE circuit board processing techniques, with minor modifications as described in the application note "Fabrication Guidelines for RO3000® Series High Frequency Circuit Materials."

Available claddings are ½ , 1 or 2 oz./ft² (17, 35, 70 μm thick) electrodeposited copper foil.

RO3000® laminates are manufactured under an ISO 9002 certified system.

Chart 1: RO3003™ Laminate Dielectric Constant vs. Temperature

The data in Chart 1 demonstrates the excellent stability of dielectric constant over temperature for RO3003™— laminates, including the elimination of the step change in dielectric constant, which occurs near room temperature with PTFE glass materials.

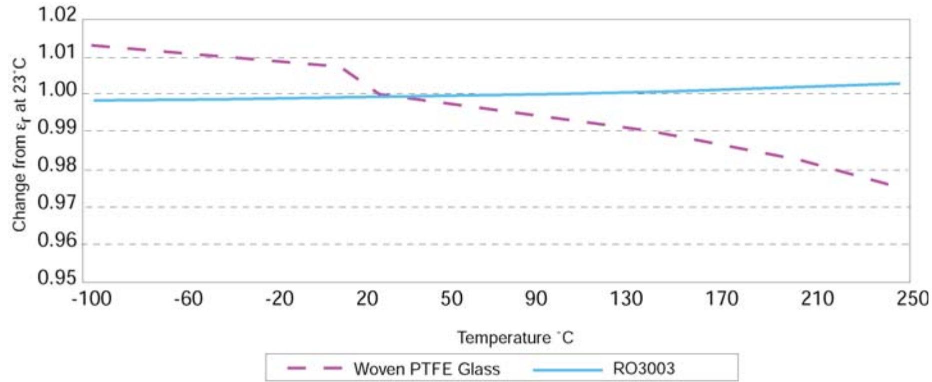

Chart 2: RO3006™ and RO3010™ Laminate Dielectric Constant vs. Temperature

The data in Chart 2 shows the change in dielectric constant vs. temperature for RO3006™ and RO3010™ laminates. These materials exhibit significant improvement in temperature stability of dielectric constant when compared to other high dielectric constant PTFE laminates.

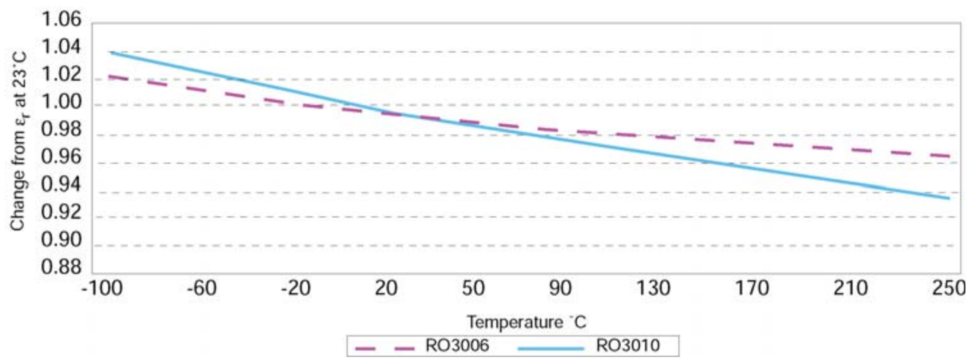

Chart 3: Dielectric Constant vs. Frequency for RO3000® Series Laminate

Chart 3 demonstrates the stability of dielectric constant for RO3000® series products over frequency. This stability simplifies the design of broad- band components as well as allowing the materials to be used in a wide range of applications over a very broad range of frequencies.

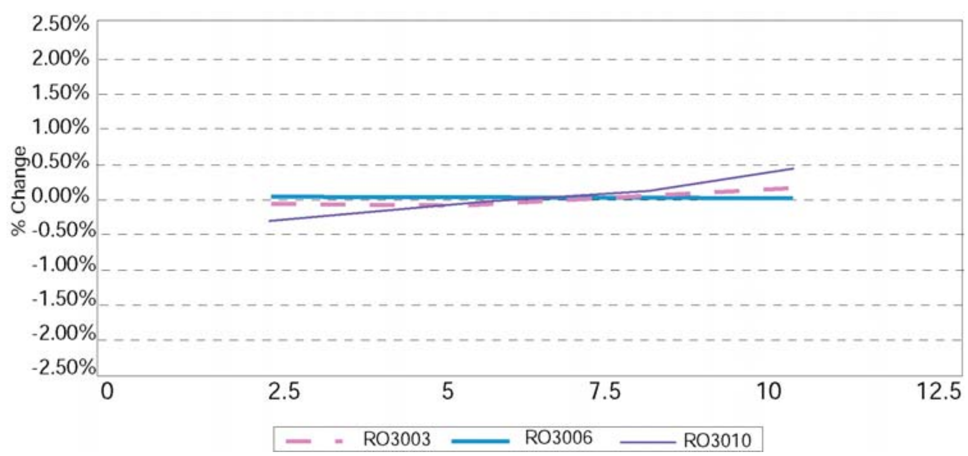

The data in Charts 1, 2 and 3 was produced using a modified IPC-TM-650, 2.5.5.5 method. For additional information request Rogers T.R. 5156 and T.M. 4924.

PROPERTY	TYPICAL VALUE (1)			DIRECTION	UNIT	CONDITION	TEST METHOD
	RO3003	RO3006	RO3010				
Dielectric Constant ε_r	3.00±0.04 (2)	6.15±0.15	10.2±0.30	Z	-	10GHz 23°C	IPC-TM-650 2.5.5.5
Dissipation Factor	0.0013	0.0020	0.0023	Z	-	10GHz 23°C	IPC-TM-650 2.5.5.5
Thermal Coefficient of ε_r	13	-160	-280	Z	ppm/°C	10GHz 0-100°C	IPC-TM-650 2.5.5.5
Dimensional Stability	0.5	0.5	0.5	X,Y	mm/m	COND A	ASTM D257
Volume Resistivity	10^7	10^3	10^3		MΩ•cm	COND A	IPC 2.5.17.1
Surface Resistivity	10^7	10^3	10^3		MΩ	COND A	IPC 2.5.17.1
Tensile Modulus	2068 (300)	2068 (300)	2068 (300)	X,Y	MPa (kpsi)	23°C	ASTM D638
Water Absorption	<0.1	<0.1	<0.1	-	%	D24/23	IPC-TM-650 2.6.2.1
Specific Heat	0.93 (0.22)	0.93 (0.22)	0.93 (0.22)		J/g/K (BTU/lb/°F)		Calculated
Thermal Conductivity	0.50	0.61	0.66	-	W/m/K	100°C	ASTM C518
Coefficient of Thermal Expansion	17 24	17 24	17 24	X,Y Z	ppm/°C	-55 to 288°C	ASTM D3386-94
Td	500	500	500		°C TGA		ASTM D 3850
Color	Tan	Tan	Off White				
Density	2.1	2.6	3.0		gm/cm^3		
Copper Peel Strength	3.1 (17.6)	2.1 (12.2)	2.4 (13.4)		N/mm (lb/in)	After solder float	IPC-TM-2.4.8
Flammability	94V-0	94V-0	94V-0				UL
Lead Free Process Capatible	Yes	Yes	Yes				

(1) References: Internal T.R.'s 1430, 2224, 2854. Tests at 23°C unless otherwise noted. Typical values should not be used for specification limits.

(2) The nominal dielectric constant of an 0.060" thick RO3003® laminate as measured by the IPC-TM-650, 2.5.5.5 will be 3.02, due to the elimination of biasing caused by air gaps in the test fixture. For further information refer to Rogers T.R. 5242.

STANDARD THICKNESS:		STANDARD PANEL SIZE:	STANDARD COPPER CLADDING:
RO3003:	**RO3006/3010:**	**RO3003:**	½ oz. (17µm), 1 oz. (35µm), 2 oz. (70µm) electrodeposited copper foil.
0.005" (0.13 mm)	0.005"(0.13 mm)	12" X 18" (305 X 457mm)	
0.010" (0.25 mm)	0.010"(0.25 mm)	24" X 18" (610 X 457mm)	
0.020" (0.50 mm)	0.025"(0.64 mm)	24" X 36" (610 X 915mm)	
0.030" (0.75 mm)	0.050"(1.28 mm)	**RO3006/3010:**	
0.060" (1.52 mm)		18" X 12" (457 X 305mm)	
		18" X 24" (457 X 610mm)	
		18" X 36" (457 X 915mm)	
		18" X 48" (457 X 1.224m)	

ROGERS CORPORATION
Advanced Circuit Materials

Advanced Circuit Materials Division
100 S. Roosevelt Avenue
Chandler, AZ 85226
Tel: 480-961-1382, Fax: 480-961-4533
www.rogerscorporation.com

Data Sheet

RO4000® Series High Frequency Circuit Materials

Features:

- Not-PTFE
- Excellent high frequency performance due to low dielectric tolerance and loss
- Stable electrical properties versus frequency
- Low thermal coefficient of dielectric constant
- Low Z-Axis expansion
- Low in-plane expansion coefficient
- Excellent dimensional stability
- Volume manufacturing process

Some Typical Applications:

- LNB's for Direct Broadcast Satellites
- Microstrip and Cellular Base Station Antennas and Power Amplifiers
- Spread Spectrum Communications Systems
- RF Identifications Tags

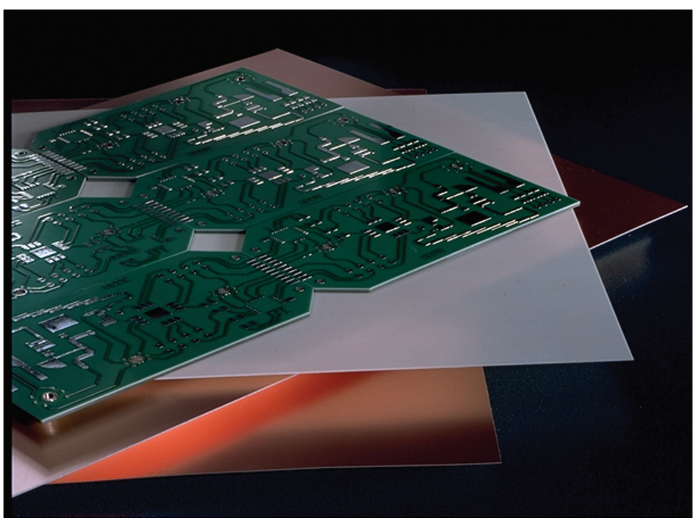

RO4000® Series High Frequency Circuit Materials are glass reinforced hydrocarbon/ceramic laminates (**Not PTFE**) designed for performance sensitive, high volume commercial applications.

RO4000 laminates are designed to offer superior high frequency performance and low cost circuit fabrication. The result is a low loss material which can be fabricated using standard epoxy/glass (FR4) processes offered at competitive prices.

The selection of laminates typically available to designers is significantly reduced once operational frequencies increase to 500 MHz and above. RO4000 material possesses the properties needed by designers of RF microwave circuits and allows for repeatable design of filters, matching networks and controlled impedance transmission lines. Low dielectric loss allows RO4000 series material to be used in many applications where higher operating frequencies limit the use of conventional circuit board laminates. The temperature coefficient of dielectric constant is among the lowest of any circuit board material (Chart 1), and the dielectric constant is stable over a broad frequency range (Chart 2). This makes it an ideal substrate for broadband applications.

RO4000 material's thermal coefficient of expansion (CTE) provides several key benefits to the circuit designer. The expansion coefficient of RO4000 material is similar to that of copper which allows the material to exhibit excellent dimensional stability, a property needed for mixed dielectric multilayer boards constructions. The low Z-axis CTE of RO4000 laminates provides reliable plated through-hole quality, even in severe thermal shock applications. RO4000 series material has a Tg of >280°C (536°F) so its expansion characteristics remain stable over the entire range of circuit processing temperatures.

RO4000 series laminates can easily be fabricated into printed circuit boards using standard FR4 circuit board processing techniques. Unlike PTFE based high performance materials, RO4000 series laminates do not require specialized via preparation processes such as sodium etch. This material is a rigid, thermoset laminate that is capable of being processed by automated handling systems and scrubbing equipment used for copper surface preparation.

RO4003™ laminates are currently offered in various configurations utilizing both 1080 and 1674 glass fabric styles, with all configurations meeting the same laminate electrical performance specification. Specifically designed as a drop-in replacement for the RO4350 material, RO4350B laminates utilize RoHS compliant flame-retardant technology for applications requiring UL 94V-0 certification. These materials conform to the requirements of IPC-4103, slash sheet /10 for RO4003C and /11 for RO4350B.

Chart 1: RO4000 Series Materials
Dielectric Constant vs. Temperature

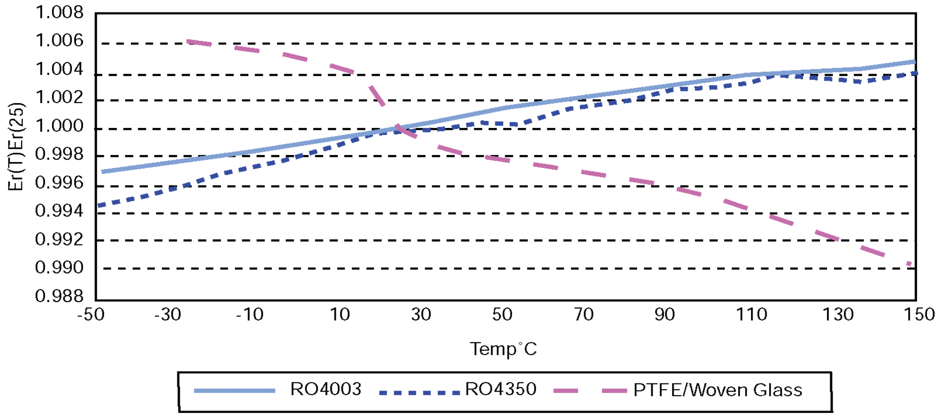

Chart 2: RO4000 Series Materials
Dielectric Constant vs. Frequency

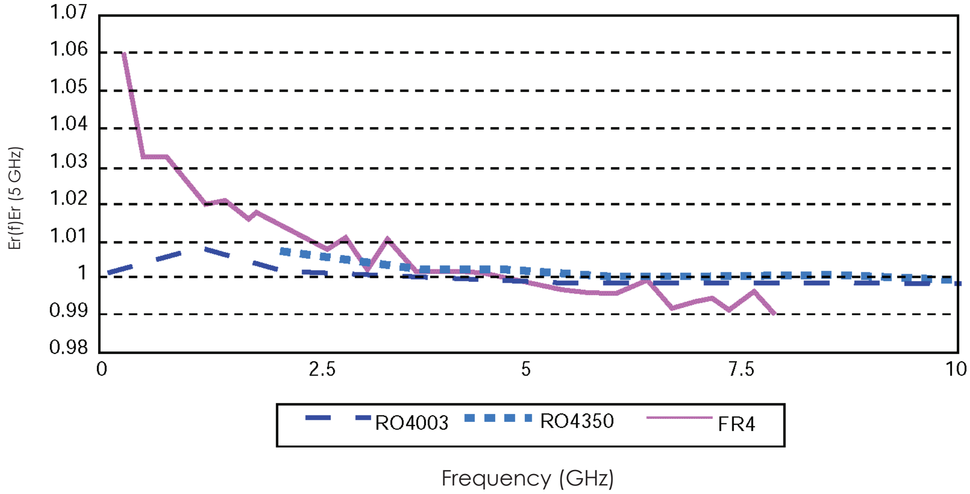

Chart 3: Microstrip Insertion Loss
(0.030" Dielectric Thickness)

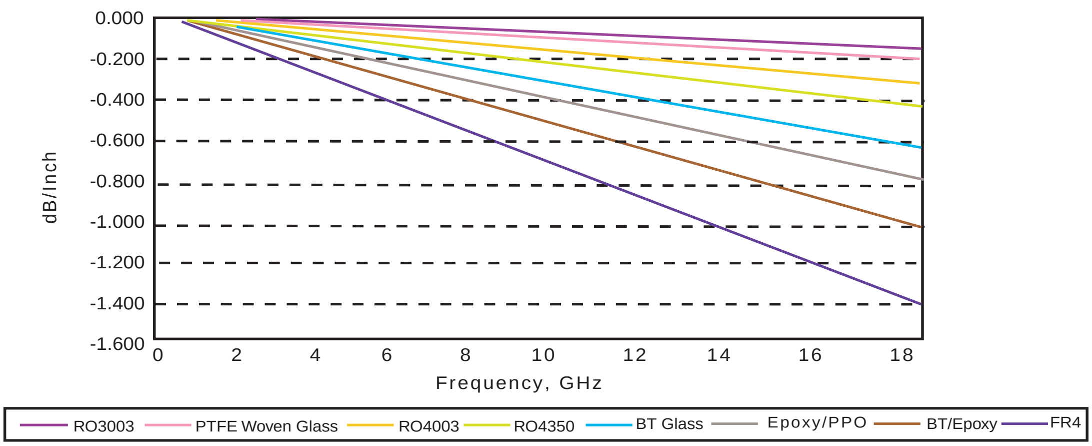

The information contained in this fabrication guide is intended to assist you in designing with Rogers' circuit materials and prepreg. It is not intended to and does not create any warranties, express or implied, including any warranty of merchantability or fitness for a particular purpose or that the results shown on this fabrication guide will be achieved by a user for a particular purpose. The user is responsible for determining the suitability of Rogers' circuit materials and prepreg for each application.

Property	Typical Value		Direction	Units	Condition	Test Method
	RO4003C™	RO4350B™				
Dielectric Constant, ε_r (Process specification)	3.38 ± 0.05	(1) 3.48 ± 0.05	Z	--	10 GHz/23°C	IPC-TM-650 2.5.5.5 (2)Clamped Stripline
(3) Dielectric Constant, ε_r (Recommended for use in circuit design)	3.55	3.66	Z	--	FSR/23°C	IPC-TM-650 2.5.5.6 Full Sheet Resonance
Dissipation Factor tan, δ	0.0027 0.0021	0.0037 0.0031	Z	--	10 GHz/23°C 2.5 GHz/23°C	IPC-TM-650 2.5.5.5
Thermal Coefficient of ε_r	+40	+50	Z	ppm/°C	-100°C to 250°C	IPC-TM-650 2.5.5.5
Volume Resistivity	1.7 X 10^{10}	1.2 X 10^{10}		MΩ•cm	COND A	IPC-TM-650 2.5.17.1
Surface Resistivity	4.2 X 10^{9}	5.7 X 10^{9}		MΩ	COND A	IPC-TM-650 2.5.17.1
Electrical Strength	31.2 (780)	31.2 (780)	Z	KV/mm (V/mil)	0.51mm (0.020")	IPC-TM-650 2.5.6.2
Tensile Modulus	26,889 (3900)	11,473 (1664)	Y	MPa (kpsi)	RT	ASTM D638
Tensile Strength	141 (20.4)	175 (25.4)	Y	MPa (kpsi)	RT	ASTM D638
Flexural Strength	276 (40)	255 (37)		MPa (kpsi)		IPC-TM-650 2.4.4
Dimensional Stability	<0.3	<0.5	X,Y	mm/m (mils/inch)	after etch +E2/150°C	IPC-TM-650 2.4.39A
Coefficient of Thermal Expansion	11 14 46	14 16 35	X Y Z	ppm/°C	-55 to 288°C	IPC-TM-650 2.1.41
Tg	>280	>280		°C DSC	A	IPC-TM-650 2.4.24
Td	425	390		°C TGA		ASTM D3850
Thermal Conductivity	0.64	0.62		W/m/°K	100°C	ASTM F433
Moisture Absorption	0.06	0.06		%	48 hrs immersion 0.060" sample Temperature 50°C	ASTM D570
Density	1.79	1.86		gm/cm^3	23°C	ASTM D792
Copper Peel Strength	1.05 (6.0)	0.88 (5.0)		N/mm (pli)	after solder float 1 oz. EDC Foil	IPC-TM-650 2.4.8
Flammability	N/A	94V-0				UL
Lead-Free Process Compatible	Yes	Yes				

(1) Dielectric constant typical value does not apply to 0.004" (0.101mm) laminates. Dielectric constant specification value for 0.004 RO4350B material is 3.36.
(2) Clamped stripline method can potentially lower the actual dielectric constant due to presence of airgap. Dielectric constant in practice may be higher than the values listed.
(3) Typical values are a representation of an average value for the population of the property. For specification values contact Rogers Corporation.

Prolonged exposure in an oxidative environment may cause changes to the dielectric properties of hydrocarbon based materials. The rate of change increases at higher temperatures and is highly dependent on the circuit design. Although Rogers' high frequency materials have been used successfully in innumerable applications and reports of oxidation resulting in performance problems are extremely rare, Rogers recommends that the customer evaluate each material and design combination to determine fitness for use over the entire life of the end product.

Standard Thickness	Standard Panel Size	Standard Copper Cladding
RO4003C: 0.008" (0.203mm), 0.012 (0.305mm), 0.016" (0.406mm), 0.020" (0.508mm) 0.032" (0.813mm), 0.060" (1.524mm) **RO4350B**: *0.004" (0.101mm), 0.0066" (0.168mm) 0.010" (0.254mm), 0.0133 (0.338mm), 0.0166 (0.422mm), 0.020" (0.508mm) 0.030" (0.762mm), 0.060" (1.524mm)	12" X 18" (305 X457 mm) 24" X 18" (610 X 457 mm) 24" X 36" (610 X 915 mm) 48" X 36" (1.224 m X 915 mm) *0. 004" material in not available in panel sizes larger than 24"x18" (610 X 457mm).	½ oz. (17µm), 1 oz. (35µm) and 2 oz. (70µm) electrodeposited copper foil.

Fabrication Guidelines for RO4000® Series High Frequency Circuit Materials

RO4000® High Frequency Circuit Materials were developed to provide high frequency performance comparable to woven glass PTFE substrates with the ease of fabrication associated with epoxy/glass laminates. RO4000 material is a glass reinforced hydrocarbon/ceramic filled thermoset material with a very high glass transition temperature (Tg >280°C). Unlike PTFE based microwave materials, no special through-hole treatments or handling procedures are required. Therefore, RO4000 material circuit processing and assembly costs are comparable to epoxy/glass laminates.

Some basic guidelines for processing double sided RO4000 panels are provided below. In general, process parameters and procedures used for epoxy/glass boards can be used to process RO4000 boards.

DRILLING:

ENTRY/EXIT MATERIAL:

Entry and exit materials should be flat and rigid to minimize copper burrs. Recommended entry materials include aluminum and rigid composite board (0.010” to 0.025” (0.254 0.635mm)). Most conventional exit materials with or without aluminum cladding are suitable.

MAXIMUM STACK HEIGHT:

The thickness of material being drilled should not be greater than 70% of the flute length. This includes the thickness of entry material and penetration into the backer material.
For example:

Flute Length:	0.300” (7.62mm)
Entry Material:	0.015” (0.381mm)
Backer Penetration:	0.030” (0.762mm)
Material Thickness:	0.020” (0.508mm)⇒(0.023”(0.584mm) with 1 oz Cu on 2 sides)

Maximum Stack Height	= 0.70 x 0.300”(7.62mm) =	0.210” (5.33mm) (available flute length)
		-0.015” (0.381mm) (entry)
		-0.030” (0.762mm) (backer penetration)
		0.165”(4.19mm) (available for PCBs)

$$\text{Maximum Boards per Stack} = \frac{0.165\text{” (4.19mm) (available for PCBs)}}{0.023\text{” (0.58mm) (thickness per board)}} = 7.2 = 7 \text{ boards/stack (round down)}$$

DRILLING CONDITIONS:

Surface speeds greater than 500 SFM and chip loads less than 0.002” (0.05mm) should be avoided, whenever possible.

Recommended Ranges:

Surface Speed:	300 - 500 SFM (90 to 150 m/mm)
Chip Load:	0.002” - 0.004”/rev. (0.05-0.10 mm/rev)
Retract Rate:	500 - 1000 IPM 500 IPM (12.7 m/min) for tool less than 0.0135" (0.343 mm),1000 IPM (25.4 m/min) for all others.
Tool Type:	Standard Carbide
Tool life:	2000-3000 hits

Hole quality should be used to determine the effective tool life rather than tool wear. The RO4003™ material will yield good hole quality when drilled with bits which are considered worn by epoxy/glass standards. Unlike epoxy/glass, RO4003 material hole roughness does not increase significantly with tool wear. Typical values range from 8-25 um regardless of hit count (evaluated up to 8000 hits). The roughness is directly related to the ceramic filler size and provides topography that is beneficial for hole-wall adhesion. Drilling conditions used for epoxy/glass boards have been found to yield good hole quality with hit counts in excess of 2000.

CALCULATING SPINDLE SPEED AND INFEED:

$$\text{Spindle Speed (RPM)} = \frac{12 \times [\text{Surface Speed (SFM)}]}{\pi \times [\text{Tool Diam. (in.)}]}$$

Feed Rate (IPM) = [Spindle Speed (RPM)] x [Chip Load (in/rev.)]

Example:

Desired Surface Speed:	400 SFM
Desired Chip Load:	0.003”(0.08 mm)/rev.
Tool Diameter:	0.0295”(0.75 mm)

$$\text{Spindle Speed} = \frac{12 \times [400]}{3.14 \times [0.0295]} = 51{,}800 \text{ RPM}$$

Infeed Rate = [51,800] x [0.003] = 155 IPM

QUICK REFERENCE TABLE:

Tool Diameter	Spindle Speed (kRPM)	Infeed Rate (IPM)
0.0100" (0.254mm)*	95.5	190
0.0135" (0.343mm)*	70.7	141
0.0160" (0.406mm)*	95.5	190
0.0197" (0.500mm)*	77.6	190
0.0256" (0.650mm)	60.0	180
0.0258" (0.655mm)	60.0	180
0.0295" (0.749mm)	51.8	155
0.0354" (0.899mm)	43.2	130
0.0394" (1.001mm)	38.8	116
0.0453" (1.151mm)	33.7	101
0.0492" (1.257mm)	31.1	93
0.0531" (1.349mm)	28.8	86
0.0625" (1.588mm)	24.5	74
0.0925" (2.350mm)	16.5	50
0.1250" (3.175mm)	15.0	45

* *Conditions stated are tapered from 200SFM and 0.002 chip load up to 400 SFM and 0.003" chip.*

DEBURRING:

RO4000 material can be deburred using conventional nylon brush scrubbers.

COPPER PLATING:

No special treatments are required prior to electroless copper plating. Board should be processed using conventional epoxy/glass procedures. Desmear of drilled holes is not typically required, as the high Tg (280°C+ [536°F]) resin system is not prone to smearing during drill. Resin can be removed using a standard CF_4/O_2 plasma cycle or a double pass through an alkaline permanganate process should smear result from aggressive drilling practices.

IMAGING/ETCHING:

Panel surfaces may be mechanically and/or chemically prepared for photoresist. Standard aqueous or semi-aqueous photoresists are recommended. Any of the commercially available copper etchants can be used.

SOLDERMASK:

Any screenable or photoimageable solder masks typically used on epoxy/glass laminates bond very well to the surface of RO4003. Mechanical scrubbing of the exposed dielectric surface prior to solder mask application should be avoided as an "as etched" surface provides for optimum bonding.

HASL and REFLOW:

RO4000 material baking requirements are comparable to epoxy/glass. In general, facilities which do not bake epoxy/glass boards will not need to bake RO4000 boards. For facilities that do bake epoxy/glass as part of their normal process, we recommend at 1-2 hour bake at 250°F-300°F (121°C-149°C).

Warning: ***RO4003*** *does not contain fire retardant(s). We understand boards trapped in an infrared (IR) unit or run at very slow conveyor speeds can reach temperatures well in excess of 700°F (371°C). RO4003 may begin to burn at these high temperatures. Facilities which still use IR reflow units or other equipment which can reach these high temperatures should take the necessary precautions to assure that there are no hazards.*

SHELF LIFE:

Rogers' High Frequency laminates can be stored indefinitely under ambient room temperatures (55-85°F, 13-30°C) and humidity levels. At room temperature, the dielectric materials are inert to high humidity. However, metal claddings such as copper can be oxidized during exposure to high humidity. Standard PWB pre-exposure cleaning procedures can readily remove traces of corrosion from properly stored materials.

ROUTING:

RO4000 material can be machined using carbide tools and conditions typically used for epoxy/glass. Copper foil should be etched away from the routing channels to prevent burring.

MAXIMUM STACK HEIGHT:

The maximum stack height should be based on 70% of the actual flute length to allow for debris removal.

Example:

Flute Length:	0.300" x 0.70 =		0.210"(5.33 mm)
Backer Penetration:		–	0.030"(0.762mm)
Max. Stack Height:			0.180"(4.572mm)

TOOL TYPE:

Carbide multifluted spiral chip breakers or diamond cut router bits.

ROUTING CONDITIONS:

Surface speeds below 500 SFM should be used whenever possible to maximize tool life. Tool life is generally greater than 50 linear feet when routing the maximum allowable stack height.

Chip Load:	0.0010-0.0015"(0.0254-0.0381mm)/rev
Surface Speed:	300 - SFM

QUICK REFERENCE TABLE:

Tool Diameter	Spindle Speed	Lateral Feed Rate
1/32	40 k RPM	50 IPM
1/16	25 k RPM	31 IPM
3/32	20 k RPM	25 IPM
1/8	15 k RPM	19 IPM

CONTACT INFORMATION:

USA:	Rogers Advanced Circuit Materials, ISO 9002 Certified	Tel: 480-961-1382	Fax: 480-917-5256
Belgium:	Rogers N.V. - Gent	Tel: +32-9-2353611	Fax: +32-9-2353658
Japan:	Rogers Japan Inc.	Tel: 81-3-5200-2700	Fax: 81-3-5200-0571
Taiwan:	Rogers Taiwan Inc.	Tel: 886-2-86609056	Fax: 886-2-86609057
Korea:	Rogers Korea Inc.	Tel: 82-31-716-6112	Fax: 82-31-716-6208
Singapore:	Rogers Technologies Singapore Inc.	Tel: 65-747-3521	Fax: 65-747-7425
China:	Rogers (Shanghai)	Tel: 86-21-63916088	Fax: 86-21-63915060
China:	Rogers (Shenzhen)	Tel: 86-755-8236 6060	Fax: 86-755-8236 6123

The information in this data sheet is intended to assist you in designing with Rogers' circuit material laminates. It is not intended to and does not create any warranties express or implied, including any warranty of merchantability or fitness for a particular purpose or that the results shown on this data sheet will be achieved by a user for a particular purpose. The user should determine the suitability of Rogers' circuit material laminates for each application.

Prolonged exposure in an oxidative environment may cause changes to the dielectric properties of hydrocarbon based materials. The rate of change increases at higher temperatures and is highly dependent on the circuit design. Although Rogers' high frequency materials have been used successfully in innumerable applications and reports of oxidation resulting in performance problems are extremely rare, Rogers recommends that the customer evaluate each material and design combination to determine fitness for use over the entire life of the end product.

These commodities, technology and software are exported from the United States in accordance with the Export Administration regulations. Diversion contrary to U.S. law prohibited.

Revised 11/02/2007-1107-0.5CC
Publication #92-004

Advanced Circuit Materials Division
100 S. Roosevelt Avenue
Chandler, AZ 85226
Tel: 480-961-1382, Fax: 480-961-4533
www.rogerscorporation.com

Advanced Circuit Materials

Data Sheet
1.5000

RT/duroid®5870 /5880 High Frequency Laminates

Features:

- Lowest electrical loss for reinforced PTFE material.
- Low moisture absorption.
- Isotropic
- Uniform electrical properties over frequency.
- Excellent chemical resistance.

Some Typical Applications:

- Commercial Airline Telephones
- Microstrip and Stripline Circuits
- Millimeter Wave Applications
- Military Radar Systems
- Missile Guidance Systems
- Point to Point Digital Radio Antennas

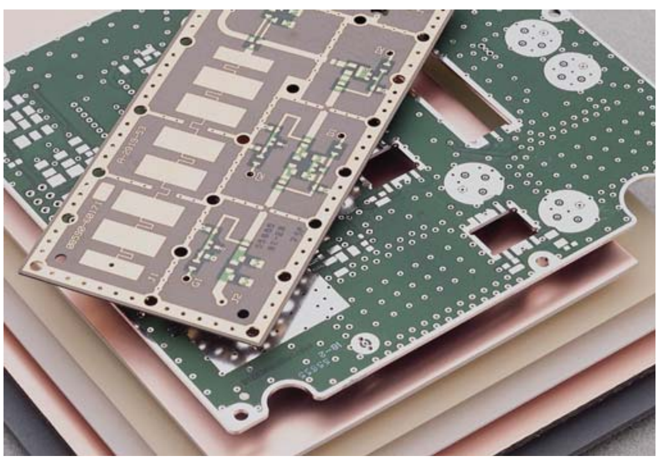

RT/duroid® 5870 and 5880 glass microfiber reinforced PTFE composites are designed for exacting stripline and microstrip circuit applications.

Glass reinforcing microfibers are randomly oriented to maximize benefits of fiber reinforcement in the directions most valuable to circuit producers and in the final circuit application.

The dielectric constant of RT/duroid 5870 and 5880 laminates is uniform from panel to panel and is constant over a wide frequency range. Its low dissipation factor extends the usefulness of RT/duroid 5870 and 5880 to Ku-band and above.

RT/duroid 5870 and 5880 laminates are easily cut, sheared and machined to shape. They are resistant to all solvents and reagents, hot or cold, normally used in etching printed circuits or in plating edges and holes.

Normally supplied as a laminate with electrodeposited copper of ¼ to 2 ounces/ft.^{2} (8 to 70μm) on both sides, RT/duroid 5870 and 5880 composites can also be clad with rolled copper foil for more critical electrical applications. Cladding with aluminum, copper or brass plate may also be specified.

When ordering RT/duroid 5870 and 5880 laminates, it is important to specify dielectric thickness, tolerance, rolled or electrodeposited copper foil, and weight of copper foil required.

PROPERTY		TYPICAL VALUE RT/duroid® 5870		TYPICAL VALUE RT/duroid 5880		DIRECTION	UNITS	CONDITION	TEST METHOD
Dielectric Constant, ε_r		2.33 2.33 ± 0.02 spec.		2.20 2.20 ± 0.02 spec.		Z Z		C24/23/50 C24/23/50	1 MHz IPC-TM-650, 2.5.5.3 10 GHz IPC-TM-2.5.5.5
Dissipation Factor, tan δ		0.0005 0.0012		0.0004 0.0009		Z Z		C24/23/50 C24/23/50	1 MHz IPC-TM-650, 2.5.5.3 10 GHz IPC-TM-2.5.5.5
Thermal Coefficient of ε_r		-115		-125			ppm/°C	-50 - 150°C	IPC-TM-650, 2.5.5.5
Volume Resistivity		2 X 10^7		2 X 10^7		Z	Mohm cm	C96/35/90	ASTM D257
Surface Resistivity		2 X 10^8		3 X 10^7		Z	Mohm	C/96/35/90	ASTM D257
Tensile Modulus		Test at 23°C	Test at 100°C	Test at 23°C	Test at 100°C		MPa (kpsi)	A	ASTM D638
		1300 (189)	490 (71)	1070 (156)	450 (65)	X			
		1280 (185	430 (63)	860 (125)	380 (55)	Y			
	ultimate stress	50 (7.3)	34 (4.8)	29 (4.2)	20 (2.9)	X			
		42 (6.1)	34 (4.8)	27 (3.9)	18 (2.6)	Y			
	ultimate strain	9.8	8.7	6.0	7.2	X	%		
		9.8	8.6	4.9	5.8	Y			
Compressive Modulus		1210 (176)	680 (99)	710 (103)	500 (73)	X	MPa (kpsi)	A	ASTM D695
		1360 (198)	860 (125)	710 (103)	500 (73)	Y			
		803 (120)	520 (76)	940 (136)	670 (97)	Z			
	ultimate stress	30 (4.4)	23 (3.4)	27 (3.9)	22 (3.2)	X			
		37 (5.3)	25 (3.7)	29 (5.3)	21 (3.1)	Y			
		54 (7.8)	37 (5.3)	52 (7.5)	43 (6.3)	Z			
	ultimate strain	4.0	4.3	8.5	8.4	X	%		
		3.3	3.3	7.7	7.8	Y			
		8.7	8.5	12.5	17.6	Z			
Deformation Under Load, Test at 150°C				1.0		Z	%	24hr/14 MPa (2 Kpsi)	ASTM D621
Heat Distortion Temperature		>260 (>500)		>260 (>500)		X.Y	°C (°F)	1.82 MPa (264 psi)	ASTM D648
Specific Heat		0.96 (0.23)		0.96 (0.23)			J/g/K (cal/g/C)		Calculated
Moisture Absorption	Thickness 0.31" (0.8mm)	0.9 (0.02)		0.9 (0.02)			mg (%)	D24/23	ASTM D570
	0.62" (1.6mm)	13 (0.015)		13 (0.015					
Thermal Conductivity		0.22		0.20		Z	W/m/K		ASTM C518
Td		500		500			°C TGA		ASTM D3850
Density		2.2		2.2					ASTM D792
Copper Peel		20.8 (3.7)		22.8 (4.0)			pli (N/mm)	after solder float	IPC-TM-650 2.4.8
Flammability		94V-0		94V-0					UL
Lead-Free Process Compatible		Yes		Yes					

PROPERTY	RT/duroid® 5870 X	RT/duroid® 5870 Y	RT/duroid® 5870 Z	RT/duroid 5880 X	RT/duroid 5880 Y	RT/duroid 5880 Z	DIRECTION	UNITS	CONDITION	TEST METHOD
Thermal Expansion	-5.0	-5.5	-11.6	-6.1	-8.7	-18.7		mm/m	-100°C	ASTM D3386 (10K/min) (Values given are total change from a base temperature of 35°C)
	-0.6	-0.9	-4.0	-0.9	-1.8	-6.9			15	
	-0.3	-0.4	-2.6	-0.5	-0.9	-4.5			25	
	0.7	0.9	7.5	1.1	1.5	8.7			75	
	1.8	2.2	22.0	2.3	3.2	28.3			150	
	3.4	4.0	58.9	3.8	5.5	69.5			250	

[1] SI unit given first with other frequently used units in parentheses.
[2] References: Internal TR's 1430, 2224, 2854. Test were at 23°C unless otherwise noted.
Typical values should not be used for specification limits.

STANDARD THICKNESS:	STANDARD PANEL SIZE:	STANDARD COPPER CLADDING:
0.005" (0.127mm), 0.031" (0.787mm) 0.010" (0.254mm), 0.062" (1.575mm) 0.015" (0.381mm), 0.125" (3.175mm) 0.020" (0.508mm),	18" X 12" (457 X 305mm) 18" X 24" (457 X 610mm) 18" X 36" (457 X 915mm) 18" X 48" (457 X 1.224m)	¼ oz. (8 μm) electrodeposited copper foil. ½ oz. (17μm), 1 oz. (35μm), 2 oz. (70μm) electrodeposited and rolled copper foil.

The information in this data sheet is intended to assist you in designing with Rogers' circuit material laminates. It is not intended to and does not create any warranties express or implied, including any warranty of merchantability or fitness for a particular purpose or that the results shown on this data sheet will be achieved by a user for a particular purpose. The user should determine the suitability of Rogers' circuit material laminates for each application.

These commodities, technology and software are exported from the United States in accordance with the Export Administration regulations. Diversion contrary to U.S. law prohibited. RT/duroid and DUROID are licensed trademarks of Rogers Corporation.

Revised 11/06 0696-1106-0.5CC **Publication #92-101**

ROGERS CORPORATION
Advanced Circuit Materials

Advanced Circuit Materials Division
100 S. Roosevelt Avenue
Chandler, AZ 85226
Tel: 480-961-1382, Fax: 480-961-4533
www.rogerscorporation.com

Data Sheet
TMM

TMM® Thermoset Microwave Materials

Features:

- Wide range of dielectric constants. Ideal for single material systems on a wide variety of applications.
- Excellent mechanical properties. Resists creep and cold flow.
- Exceptionally low thermal coefficient of dielectric constant.
- Coefficient of thermal expansion matched to copper. High reliability of plated through holes.
- Resistant to process chemicals. No damage to material during fabrication and assembly processes.
- Thermoset resin for reliable wirebonding. No specialized production techniques required. TMM 10 and 10i laminates can replace alumina substrates.

Some Typical Applications:

- RF and Microwave Circuitry
- Global Positioning Systems Antennas
- Power Amplifiers and Combiners
- Patch Antennas
- Filters and Coupler
- Dielectric Polarizers and Lenses
- Satellite Communication Systems
- Chip Testers

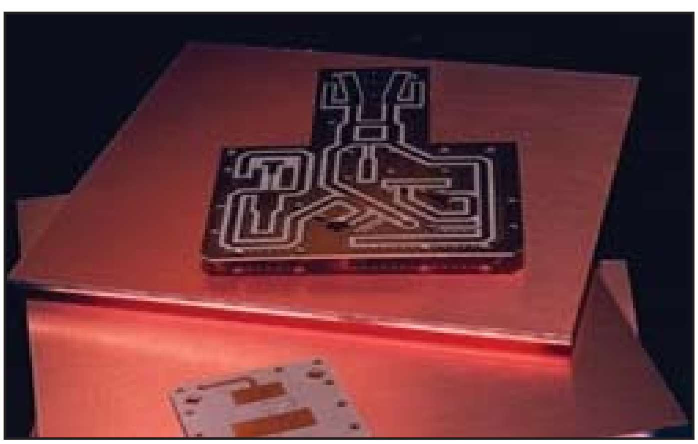

TMM® thermoset microwave materials are ceramic thermoset polymer composites designed for high plated-thru-hole reliability stripline and microstrip applications. TMM laminates are available in a wide range of dielectric constants and claddings.

The electrical and mechanical properties of TMM laminates combine many of the benefits of both ceramic and traditional PTFE microwave circuit laminates, without requiring the specialized production techniques common to these materials. TMM laminates do not require a sodium napthanate treatment prior to electroless plating.

TMM laminates have an exceptionally low thermal coefficient of dielectric constant, typically less than 30 ppm/°C. The material's isotropic coefficients of thermal expansion, very closely matched to copper, allow for production of high reliability plated through holes, and low etch shrinkage values. Furthermore, the thermal conductivity of TMM laminates is approximately twice that of traditional PTFE/ceramic laminates, facilitating heat removal.

TMM laminates are based on thermoset resins, and do not soften when heated. As a result, wire bonding of component leads to circuit traces can be performed without concerns of pad lifting or substrate deformation.

TMM laminates combine many of the desirable features of ceramic substrates with the ease of soft substrate processing techniques. TMM laminates are available clad with 1/2 oz/ft^2 to 2 oz/ ft^2 electrodeposited copper foil, or bonded directly to brass or aluminum plates. Substrate thicknesses of 0.015" to 0.500" and greater are available. The base substrate is resistant to etchants and solvents used in printed circuit production. Consequently, all common PWB processes can be used to produce TMM thermoset microwave materials.

PROPERTIES	TYPICAL VALUES					DIRECTION	UNITS	CONDITIONS	TEST METHOD
	TMM3	TMM4	TMM6	TMM10	TMM10I				
(1) Dielectric Constant, ε_r	3.27 ± 0.032	4.50 ± 0.045	6.00 ± 0.080	9.20 ± 0.230	9.80 ± 0.245	Z		10 GHz	IPC-TM-650 method 2.5.5.5
(1) Dissipation Factor, tan δ	0.0020	0.0020	0.0023	0.0022	0.0020	Z		10 GHz	IPC-TM-650 method 2.5.5.5
Thermal Coefficient of ε_r	+37	+15	-11	-38	-43*		ppm/K	-55 to +125°C	IPC-TM-650 method 2.5.5.5
Insulation Resistance	>2000	>2000	>2000	>2000	>2000		Gohm	C/96/60/95	ASTM D257
Volume Resistivity	$3X10^9$	$6X10^8$	$1X10^8$	$2X10^8$	$2X10^8$		Mohm cm		ASTM D257
Surface Resistivity	$>9X10^9$	$1X10^9$	$1X10^9$	$4X10^7$	$4X10^7$		Mohm		ASTM D257
Flexural Strength	16.53	15.91	15.02	13.62	-	X,Y	kpsi	A	ASTM D790
Flexural Modulus	1.72	1.76	1.75	1.79	1.80*	X,Y	Mpsi	A	ASTM D790
Impact, Notch Izod	0.33	0.36	0.42	0.43	-	X,Y	ft-lb/in		ASTM D256A
Water Absorption (2X2)							%	D/48/50	ASTM D570
1.27mm (0.050" thk)	0.06	0.07	0.06	0.09	0.16				
3.18mm (0.125" thk)	0.12	0.18	0.20	0.20	0.13				
Specific Gravity	1.78	2.07	2.37	2.77	2.77			A	ASTM D792
Specific Heat	0.87	0.83	0.78	0.74	0.72*		J/g/K	A	Calculated
Thermal Conductivity	0.70	0.70	0.72	0.76	0.76	Z	W/m/K	80°C	ASTM C518
Thermal Expansion	15	16	18	21	19	X,Y	ppm/K	0 to 140°C	ASTM D3386
	23	21	26	20	20	Z			
Td	425	425	425	425	425		°C TGA		ASTM D3850
Copper Peel Strength	5.7 (1.0)	5.7 (1.0)	5.7 (1.0)	5.0 (0.9)	5.0 (0.9)	X,Y	lb/inch (N/mm)	after solder float 1 oz. EDC	IPC-TM-650 Method 2.4.8
Lead-Free Process Capable	YES	YES	YES	YES	YES				

Notes: ASTM D3386 corresponds to IPC-TM-650, method 2.4.4.1
* estimated

Typical values are a representation of an average value for the population of the property. For specification values contact Rogers Corporation.

(1) Prolonged exposure in an oxidative environment may cause changes to the dielectric properties of hydrocarbon based materials. The rate of change increases at higher temperatures and is highly dependent on the circuit design. Although Rogers' high frequency materials have been used successfully in innumerable applications and reports of oxidation resulting in performance problems are extremely rare, Rogers recommends that the customer evaluate each material and design combination to determine fitness for use over the entire life of the end product.

AVAILABLE THICKNESS:		STANDARD PANEL SIZE:	STANDARD COPPER CLADDING:
0.015" (0.381mm) 0.020" (0.508mm) 0.025" (0.635mm) 0.030" (0.762mm) 0.050" (1.270mm) 0.060" (1.524mm) 0.075" (1.905mm) 0.100" (2.540mm)	0.125" (3.175mm) 0.150" (3.810mm) 0.200" (5.080mm) 0.250" (6.350mm) 0.275" (6.985mm) 0.300" (7.620mm) 0.500" (12.70mm)	18" X 12" (457 X 305mm) 18" X 24" (457 X 610mm)	½ (17µm), 1 oz (35µm), 2 oz. (70µm) electrodeposited copper foil. Heavy metal cladding available. Contact Rogers customer service.

Revised 05/2008 0797-0508-0.5CC Publication #92-108